

The Chiral Belle Conceptual Design Report: Upgrading SuperKEKB with a Polarized Electron Beam

Belle II Collaboration

Publishing date

Executive Summary

Upgrading the SuperKEKB electron-positron collider with polarized electron beams opens a new program of precision physics at a center-of-mass energy of 10.58 GeV, the mass of the $\Upsilon(4S)$ meson. This white paper describes the physics potential of this ‘Chiral Belle’ program. It includes projections for precision measurements of $\sin^2 \theta_W$ that can be obtained from independent left-right asymmetry measurements of e^+e^- transitions to pairs of electrons, muons, taus, charm and b-quarks. The $\sin^2 \theta_W$ precision obtainable at SuperKEKB will match that of the LEP/SLC world average but at the centre-of-mass energy of 10.58 GeV. Measurements of the couplings for muons, charm, and b-quarks will be substantially improved and the existing 3σ discrepancy between the SLC A_{LR} and LEP A_{FB}^b measurements will be addressed. Precision measurements of neutral current universality will be more than an order of magnitude more precise than currently available. As the energy scale is well away from the Z^0 -pole, the precision measurements will have sensitivity to the presence of a parity-violating dark sector gauge boson, Z_{dark} . The program also enables the measurement of the anomalous magnetic moment $g - 2$ form factor of the τ to be made at an unprecedented level of precision. A precision of 10^{-5} level is accessible with 40 ab^{-1} and with more data it would start to approach the 10^{-6} level. This technique would provide the most precise information from the third generation about potential new physics explanations of the muon $g - 2$ 4σ anomaly. Additional τ and QCD physics programs enabled or enhanced with having polarized electron beams are also discussed in this White Paper.

In order to implement e^- beam polarization in the SuperKEKB high energy ring (HER), three hardware upgrades are required: 1) introduction of a low-emittance polarized source that supplies SuperKEKB with transversely polarized electrons that provide separate data sets with opposite polarization states; 2) a system of spin rotator magnets that rotate the spin of the electrons in the beam to be longitudinal before the interaction point (IP) where the Belle II detector is located, and then back to transversely polarized after the IP; and 3) a Compton polarimeter that provides online measurements of the beam polarization at a location between the first spin rotator and the IP. A precision measurement of the polarization is also made at the IP by analysing the spin-dependent decay kinematics of τ leptons produced in a $e^+e^- \rightarrow \tau^+\tau^-$ data set. This White Paper will review the current status of the R&D associated with the three hardware projects and describes the τ polarimetry analysis of 0.4 ab^{-1} of e^+e^- data collected at the $\Upsilon(4S)$ with the *BABAR* experiment that shows the high precision that can be achieved. This paper includes a summary of the path forward in R&D and next steps required to implement this upgrade and access its exciting discovery potential.

Contents

1	Introduction	1
2	Precision Electroweak Program	2
2.1	Muon Pair A_{LR}	5
2.2	Tau Pair A_{LR}	6
2.3	Charm and Beauty A_{LR}	7
2.3.1	Introduction	7
2.3.2	Training and evaluation of the model	7
2.3.3	Evaluation	7
2.3.4	Classification of $c\bar{c}$	9
2.3.5	Classification of $b\bar{b}$	9
2.3.6	Lepton requirement study	9
2.3.7	Beauty A_{LR}	10
2.3.8	Charm A_{LR}	12
2.4	Bhabha A_{LR}	13
3	Tau $g - 2$	14
4	Tau EDM	17
5	Tau LFV	18
6	QCD: Dynamical mass generation studies with polarized beams	19
7	Polarized Source	21
7.1	Beam Generation	21
7.1.1	Cathode Production and Testing	22
7.2	Linac Transport	22
8	Beam-Beam Effects on Polarization	23
9	Spin Rotator	24
9.1	BINP Spin Rotator Concepts	24
9.1.1	The concept of a scheme for obtaining longitudinal polarization	24
9.1.2	Spin rotators	27
9.1.3	Beam depolarization time	30
9.1.4	Conclusions	34
9.2	Dipole-Solenoid-Quadrupoles Combined Function Magnets Concept	35
9.2.1	Rotator Modelling with BMAD	36
9.2.2	Open-geometry Optimization	37
9.2.3	Closed-geometry Optimization	38
9.2.4	Match the Tune	39
9.2.5	Match the Chromaticity	40
9.2.6	HER With Spin Rotators: Rotator Ring	42
9.2.7	Tracking Studies and Next Steps	44
9.3	Direct Wind Magnet for Spin Rotators	50

10 Compton Polarimetry	54
10.1 Introduction	54
10.2 Integration	55
10.2.1 Laser-electron beam interaction point	55
10.2.2 Photon detector	55
10.2.3 Electron detector	57
10.3 Sensitivity studies	57
10.3.1 Event generation	58
10.3.2 Fitting procedure	60
10.4 Summary and outlook	62
11 Touschek Polarimetry	63
11.1 Introduction	63
11.2 Touschek lifetime and polarization	64
11.3 s-dependance of Touschek lifetime	65
11.4 Touschek lifetime measurement at SuperKEKB	66
11.5 Conclusion	72
12 Tau Polarimetry	72
12.1 Event Selection	73
12.2 Fitting	75
12.3 Extracted vs Input Beam Polarization Study	76
12.4 Systematic Uncertainties	76
12.5 Preliminary results from <i>BABAR</i> Beam Polarization Fit	78
13 Summary and Next Steps	78

1 Introduction

The SuperKEKB e^+e^- collider, operating at a center-of-mass energy of 10.58 GeV with its high luminosity, can access new windows for discovery with the Belle II experiment if it is upgraded to have a longitudinally polarized electron beam. Upgrading SuperKEKB to provide large samples of left-handed and right-handed initial-state electrons with approximately 70% polarization at the Belle II interaction point creates a unique and versatile facility for probing new physics with precision measurements that no other experiments, current or planned, can achieve. This upgrade is being considered and the associated R&D program is underway. This paper describes the physics potential of this “Chiral Belle” program and how the upgrade can be implemented.

The measurements in this ‘Chiral Belle’ program include precision measurements of $\sin^2 \theta_W$ obtained from independent left-right asymmetry measurements of e^+e^- transitions to pairs of electrons, muons, taus, charm and b-quarks. The $\sin^2 \theta_W$ precision obtainable at SuperKEKB will match that of the LEP/SLC world average but at the center-of-mass energy of 10.58 GeV, thereby probing the neutral current couplings with unprecedented precision at a new energy scale, which is sensitive to the running of the couplings. World average measurements of the individual neutral current vector coupling constants to b- and c-quarks and muons in particular will be substantially improved, and the residual 3σ discrepancy between the SLC A_{LR} and LEP A_{FB}^b measurements will be addressed. Precision measurements of neutral current universality will be more than an order of magnitude more precise than currently available, with measurements sensitive to parity-violating dark sector gauge bosons. If there is a dark-sector parity-violating equivalent of the Standard Model (SM) Z^0 , a Z_{dark} , with a mass below that of the SM Z^0 , then precision parity-violation measurements at 10 GeV provide a unique sensitivity to its presence, particularly if a Z_{dark} has different couplings to different SM fermions. The Chiral Belle physics program also enables the measurement of the tau-lepton g-2 at an unprecedented and unrivaled level of precision. It is the only method for measuring tau g-2 that can approach a level of precision of interest in a Minimal Flavor Violation third-generation analog of the muon g-2 4σ anomaly. Other physics uniquely enabled with polarized electron beams includes precision measurements of the tau EDM and tau Michel parameters. In addition, searches for lepton flavor violation in tau decays and dynamical mass generation hadronization studies are enhanced will be enhanced with polarized beams.

The upgrade to SuperKEKB involves three hardware projects:

- 1) A low-emittance polarized electron source in which the electron beams would be produced via a polarized laser illuminating a “strained lattice” GaAs photocathode as was done for SLD [1]. The source would produce a sample of left-handed and a sample of right-handed longitudinally polarized electron bunches whose spin would be rotated to be transversely polarized (with spins vertically up or vertically down) before encountering any dipole magnets, thereby ensuring spin stability in the SuperKEKB 7 GeV electron storage ring - the High Energy Ring (HER);
- 2) A pair of spin-rotators, one positioned before and the other after the interaction region, to rotate the spin to longitudinal prior to collisions and back to transverse following collisions. The challenge is to design the rotators to be transparent to the rest of the HER lattice, which requires minimizing couplings between vertical and horizontal planes and addressing higher order and chromatic effects in the design to ensure the luminosity is not degraded;
- 3) A Compton polarimeter that measures the beam polarization before the beam enters the interaction region. The beam polarization is also measured directly at the IP via the analysis of decays of τ leptons produced in $e^+e^- \rightarrow \tau^+\tau^-$ events.

The rest of this paper provides more details of the physics discovery potential and how electron polarization can be implemented in an upgrade to SuperKEKB while maintaining the high luminosity.

2 Precision Electroweak Program

A data sample of 20 ab^{-1} with a polarized electron beam enables Belle II to measure the weak neutral current vector coupling constants of the b -quark, c -quark and muon at significantly higher precision than any previous experiment. With 40 ab^{-1} of polarized beam data, the precision of the vector couplings to the tau and electron can be measured at a level comparable to current world averages, which are dominated by LEP and SLD measurements at the Z^0 -pole.

Within the framework of the Standard Model (SM) these measurements of g_V^f , the neutral current vector coupling for fermion f , can be used to determine the weak mixing angle, θ_W , through the relation: $g_V^f = T_3^f - 2Q_f \sin^2 \theta_W$, where T_3^f is the 3rd component of weak isospin of fermion f , Q_f is its electric charge in units of electron charge and the notational conventions of Reference [1] are used.

As described in Reference [2], with polarized electron beams an e^+e^- collider at 10.58 GeV enables the determination of g_V^f by measuring the left-right asymmetry, A_{LR}^f , for each identified final-state fermion-pair in the process $e^+e^- \rightarrow f\bar{f}$. With SM Born cross sections for 100% left-handed ($\sigma_{\mathbf{L}}$) and 100% right-handed ($\sigma_{\mathbf{R}}$) initial state electrons in s-channel processes, such as $e^+e^- \rightarrow \mu^+\mu^-$,

$$A_{LR}^f(\text{SM}) = \frac{\sigma_{\mathbf{L}}^f - \sigma_{\mathbf{R}}^f}{\sigma_{\mathbf{L}}^f + \sigma_{\mathbf{R}}^f} = \frac{sG_F}{\sqrt{2}\pi\alpha Q_f} g_A^e g_V^f \quad (1)$$

where $g_A^e = T_3^e = -\frac{1}{2}$ is the neutral current axial coupling of the electron, G_F is the Fermi coupling constant, and s is the square of the center-of-mass energy. The Bhabha channel, $e^+e^- \rightarrow e^+e^-$, with a significant t-channel contribution, has a different dependence on the SM couplings than presented in Equation 1, as discussed in section 2.4. These left-right asymmetries arise from $\gamma - Z$ interference and, although the SM asymmetries are small (approximately -6×10^{-4} for the μ and τ leptons, $+1.5 \times 10^{-4}$ for electrons, -5×10^{-3} for charm and -2% for the b -quarks), unprecedented precisions can be achieved because of the combination of both the high luminosity of SuperKEKB and a 70% beam polarization measured with precision of better than $\pm 0.5\%$. Note that, because of the small asymmetries, the denominator is dominated by the parity-conserving components of the cross-section. Nonetheless, the measurements include these parity-violating components in both numerator and denominator.

Independent measurements of A_{LR}^f for the different final state fermions ($f = e, \mu, \tau$, c-quark, b-quark) are performed by selecting pure samples of each event type and counting the numbers of such events when the beam longitudinal polarization is left-handed (\mathbf{L}) and separately when it is right-handed (\mathbf{R}), so that:

$$A_{LR}^f(\text{measured}) = \frac{N_{\mathbf{L}}^f - N_{\mathbf{R}}^f}{N_{\mathbf{L}}^f + N_{\mathbf{R}}^f} \langle Pol \rangle \quad (2)$$

$\langle Pol \rangle$ is the average electron beam polarization for the sample under consideration:

$$\langle Pol \rangle = \frac{1}{2} \left[\left(\frac{N_{eR} - N_{eL}}{N_{eR} + N_{eL}} \right)_{\mathbf{R}} - \left(\frac{N_{eR} - N_{eL}}{N_{eR} + N_{eL}} \right)_{\mathbf{L}} \right] \quad (3)$$

where N_{eR} is the actual number of right-handed electrons and N_{eL} the actual number of left-handed electrons in the event samples where the electron beam bunch is nominally left polarized or right polarized, as indicated by the ‘ \mathbf{L} ’ and ‘ \mathbf{R} ’ subscripts.

High precision measurements of A_{LR}^f , and consequently of $\sin^2 \theta_W^f$, are possible at such an upgraded SuperKEKB because with 20 ab^{-1} of data Belle II can identify between 10^9 and 10^{10} final-state pairs of b-quarks, c-quarks, taus, muons and electrons with high purity and reasonable signal efficiency, and because all detector-related systematic errors can be made to cancel by flipping

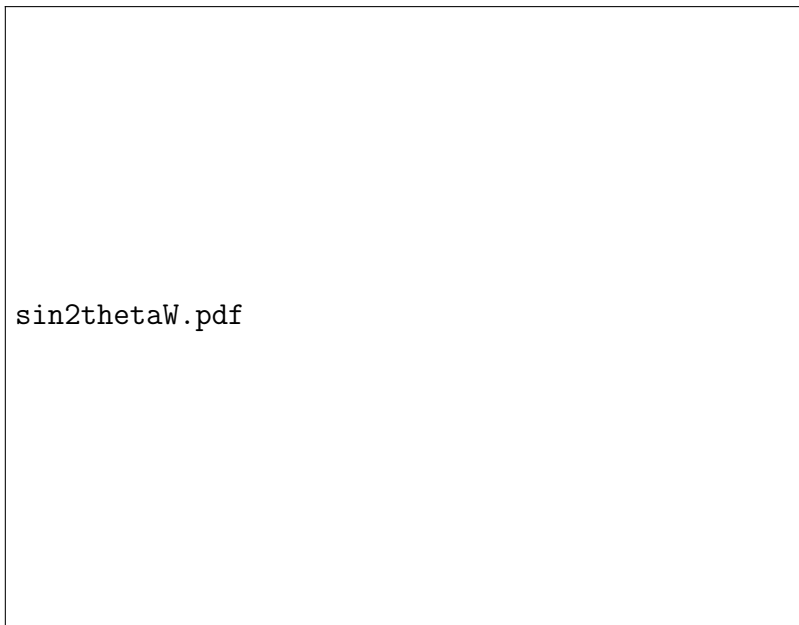


Figure 1: Determination of $\sin^2 \theta_W$ at present and future experimental facilities as a function of energy scale, adapted from [3–5].

the laser polarization at the source from \mathbf{R} to \mathbf{L} in a random, but known, pattern. $\langle Pol \rangle$ would be measured in two ways. The first method uses a Compton polarimeter, which can be expected to have an absolute uncertainty at the Belle II interaction point of less than 1% and provides a ‘bunch-by-bunch’ measurement of $\left(\frac{N_{eR}-N_{eL}}{N_{eR}+N_{eL}}\right)_{\mathbf{R}}$ and $\left(\frac{N_{eR}-N_{eL}}{N_{eR}+N_{eL}}\right)_{\mathbf{L}}$. The uncertainty will be dominated by the need to predict the polarization loss from the Compton polarimeter to the interaction point. The second method measures the polar angle dependence of the polarization of τ -leptons produced in $e^+e^- \rightarrow \tau^+\tau^-$ events using the kinematic distributions of the decay products of the τ separately for the \mathbf{R} and \mathbf{L} data samples. The forward-backward asymmetry of the tau-pair polarization is linearly dependent on $\langle Pol \rangle$ and therefore can be used to determine $\langle Pol \rangle$ to better than 0.5% with a 10 ab^{-1} \mathbf{R} sample and 10 ab^{-1} \mathbf{L} sample at the Belle II interaction point in a manner entirely independent of the Compton polarimeter, as discussed in section 12. The τ polarimetry method avoids the uncertainties associated with tracking the polarization losses to the interaction point, and also automatically accounts for any residual positron polarization that might be present. In addition, it automatically provides a luminosity-weighted beam polarization measurement.

Table 1 provides the sensitivities to electroweak parameters expected with polarized electron beams in an upgraded SuperKEKB from $e^+e^- \rightarrow b\bar{b}$, $e^+e^- \rightarrow c\bar{c}$, $e^+e^- \rightarrow \tau^+\tau^-$, $e^+e^- \rightarrow \mu^+\mu^-$, and $e^+e^- \rightarrow e^+e^-$ events selected by Belle II. From this information the precision on the b-quark, c-quark and muon neutral current vector couplings will improve by a factor of four, seven and five, respectively, over the current world average values[1] with 20 ab^{-1} of polarized data.

This is of particular importance for g_V^b , where the measurement of -0.3220 ± 0.0077 is 2.8σ higher than the SM value of -0.3437 [1]. That discrepancy arises from the 3σ difference between the SLC A_{LR} measurements and LEP A_{FB}^b measurements of $\sin^2 \theta_W^{eff}$. A measurement of g_V^b at an upgraded SuperKEKB that is four times more precise and which avoids the hadronization uncertainties that are a significant component of the uncertainties of the measurement of the forward-backward asymmetry at LEP, or any other forward-backward asymmetry measurement using on-shell Z^0 bosons, will be able to definitively resolve whether or not this is a statistical fluctuation or a first hint of a genuine breakdown of the SM.

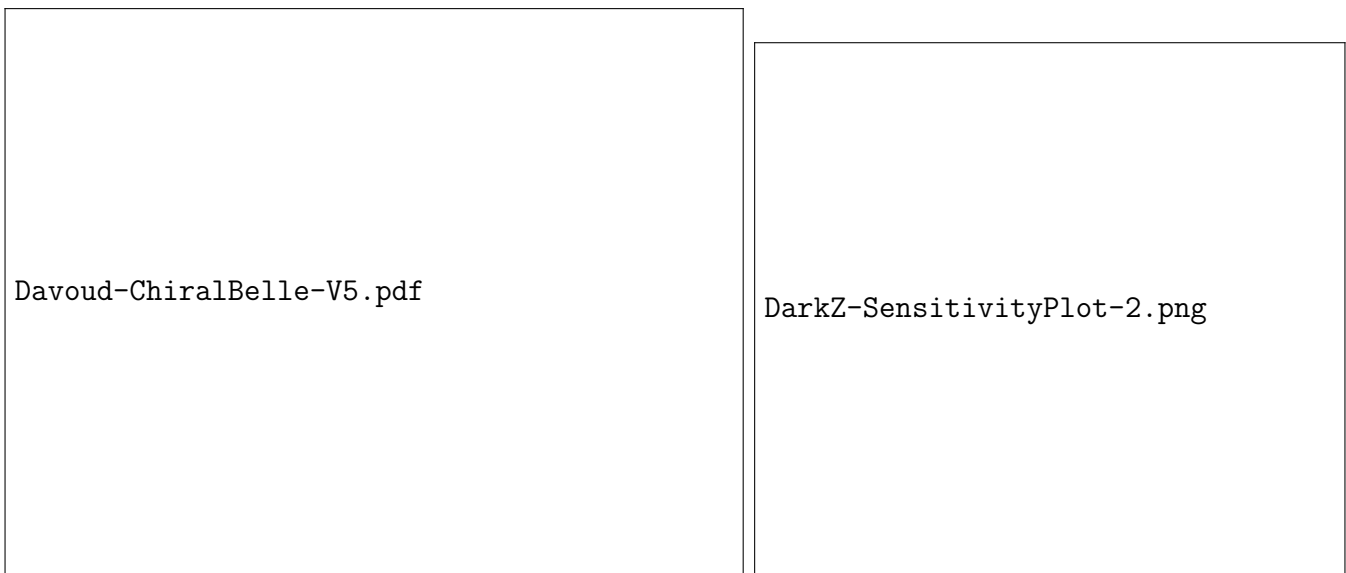


Figure 2: Left: Dark blue band shows Q^2 -dependent shift in $\sin^2 \theta_W$ caused by a 15 GeV mass dark Z , adapted from [6]. Right: Comparison of the difference between $\sin^2 \theta_W$ at $Q^2 = 10.58^2 \text{GeV}^2$ for the SM and in a model with two values of the product of the model-dependent parameters, $\epsilon\delta$, as a function of $m_{\text{dark}Z}$. The projected precision of the measurement of $\sin^2 \theta_W$ with 40 ab^{-1} at Chiral Belle is indicated by the red line. The magnitude of the SM theory error on $\sin^2 \theta_W$ is shown by the yellow band.

Table 1 also indicates the uncertainties on $\sin^2 \theta_W^{\text{eff}}$ that can be achieved with 40 ab^{-1} of polarized beam data - the combined uncertainty at Chiral Belle would be comparable to the Z^0 world average measured uncertainty of ± 0.00016 from LEP and SLD[1] but made away from the Z^0 -pole at an order of magnitude lower energy scale. Assuming lepton universality, the uncertainty on $\sin^2 \theta_W^{\text{eff}}$ from the three Chiral Belle lepton measurements, including the common systematic uncertainty on the beam polarization measurement, is projected to be ± 0.00018 . Figure 1 shows the determinations of $\sin^2 \theta_W$ as a function of energy scale at present and future experimental facilities including SuperKEKB upgraded with a polarized electron beam delivering 40 ab^{-1} of data to Belle II.

This electroweak program with polarized electron beams in SuperKEKB would also provide the most precise tests of neutral current vector coupling universality for all available final-state fermions. The ratio of A_{LR}^{f1}/A_{LR}^{f2} , which provides a measure of the ratio g_V^{f1}/g_V^{f2} , does not depend on the beam polarization, which cancels in the ratio. Because of this cancellation, the universality ratio is measured with an uncertainty dominated by statistics. For example, g_V^b/g_V^c would be measured with a relative uncertainty below 0.3%, an order of magnitude lower than the current uncertainty on this ratio. In addition, right-handed b -quark couplings to the Z can be experimentally probed with high precision at Belle II with polarized beams. Also, measurements with the projected precision will enable Belle II to probe parity violation induced by the exchange of heavy particles such as a hypothetical TeV-scale Z' boson(s). If such bosons only couple to leptons they will not be produced at the LHC. Moreover, the SuperKEKB machine will have a unique possibility to probe parity violation in the lepton sector mediated by light and very weakly coupled particles often referred to as “Dark Forces”. Such forces have been entertained as a possible connecting link between normal and dark matter [7, 8]. SuperKEKB with polarization would be uniquely sensitivity to “Dark Sector” parity violating light neutral gauge bosons, especially when Z_{dark} is off-shell and with a mass between roughly 10 and 35 GeV [6] or even up to the Z^0 pole, or couples more to the 3rd generation (see Figure 2).

Final State Fermion	A_{LR}^{SM}	Relative A_{LR} Error (%)	g_V^f W.A.[1]	$\sigma(g_V^f)$ (20 ab ⁻¹)	$\sigma(g_V^f)$ (40 ab ⁻¹)	$\sigma(s^2\theta_W)$ (40 ab ⁻¹)
b-quark (eff.=0.3)	-0.020	0.4	-0.3220 ±0.0077	0.002 improves x4	0.002	0.003
c-quark (eff.=0.15)	-0.005	0.5	+0.1873 ±0.0070	0.001 improves x7	0.001	0.0008
tau (eff.=0.25)	-0.0006	2.4	-0.0366 ±0.0010	0.001	0.0008	0.0004
muon (eff.=0.5)	-0.0006	1.5	-0.03667 ±0.0023	0.0007 improves x3	0.0005	0.0003
electron (17nb acceptance, eff=.36)	+0.00015	2.0	-0.3816 ±0.00047	0.0009	0.0006	0.0003

Table 1: For each fermion pair cleanly identifiable in Belle II for the given efficiency in column 1: column 2 gives the SM value of A_{LR} ; column 3, the expected relative error on A_{LR} based on based on 40 ab⁻¹ and a beam polarization at Belle II of 0.700 ± 0.003 with an error of ± 0.003 ; column 4, the current world average value of its neutral current vector coupling; column 5, the projected error on g_V^f with 20 ab⁻¹ of data; column 6, the projected error on g_V^f with 40 ab⁻¹ of data; and column 7, the projected SuperKEKB/Belle II error on $\sin^2\theta_W^{eff}$ with 40 ab⁻¹ of polarized e^- beam data.

The enhancement of parity violation in the muon sector has been an automatic consequence of some models [9] that aim at explaining the unexpected result for the recent Lamb shift measurement in muonic hydrogen [10]. The left-right asymmetry of the $e^-e^+ \rightarrow \mu^-\mu^+$ in such models is expected to be enhanced at low-to-intermediate energies, and SuperKEKB with polarized beams may provide a conclusive test of such models, as well as impose new constraints on a parity-violating dark sector.

2.1 Muon Pair A_{LR}

A study with polarized $e^+e^+ \rightarrow \mu^+\mu^-$ KKMC Monte Carlo events processed with the Belle II GEANT4 detector response software and Belle II event reconstruction software, validated with Belle II μ -pair data, demonstrates that a high purity selection with an efficiency of 50% for a measurement of A_{LR}^μ is quite feasible [11]. The selection of muon pairs starts from a set of two track events. The two tracks are required to be back-to-back, to have $\theta_{cms} > 30^\circ$, and to have an invariant mass $M_{\mu\mu}$ in the range $8.7 < M_{\mu\mu} < 11$ GeV/ c^2 . The angular region corresponds to that covered by the muon identification system. To suppress Bhabha events, which make up the vast majority of the two-track sample, both tracks are required to be identified as muons. The fraction of Bhabha events in the final selected sample is 0.014%. The efficiency of this selection can be derived from data, and exceeds 96% within that geometrical acceptance. The trigger efficiency, also derived from Belle II collision data, is essentially 100%. The overall selection efficiency is 50.4%, which for the 1147 pb⁻¹ production cross section, corresponds to an effective cross-section for selected events of 578 pb⁻¹. For a 10 ab⁻¹ sample of each polarization state (20 ab⁻¹ in total) having 70% polarization, and assuming $A_{LR}^\mu(\text{measured}) = A_{LR}^\mu(\text{SM}) \times \langle Pol \rangle = -0.00064$ [12] $\times 0.70 = -0.00045$, the statistical uncertainty on A_{LR} is 2.1%. With a 40 ab⁻¹ sample, the relative statistical uncertainty is 1.5%.

With this selection the decays of $\Upsilon(1S)$, $\Upsilon(2S)$, and $\Upsilon(3S)$ to $\mu^+\mu^-$ make up approximately 0.1% of selected events. These are produced via initial state radiation to the lower mass Υ states and such ‘radiative return’ processes have been extensively studied (see e.g. [13]). If one assumes the asymmetry for these events is that of $b\bar{b}$ events, $A_{LR}^b(\text{SM}) = -0.020$, then they would have an

asymmetry 32 times larger than A_{LR}^μ . As the Chiral Belle program calls for a precision measurement of A_{LR}^b (see section 2.3), and the contributions of the Υ resonances to the sample can be measured independently of the A_{LR} measurement, this systematic effect can be controlled and is not expected to contribute significantly to the overall uncertainty. The uncertainty on the measured polarization produces an uncertainty on A_{LR} of 0.4%, as discussed in section 12. Other uncertainties, including residual contamination from Bhabha, tau pair, and $q\bar{q}$ events, are expected to contribute a small amount to the systematic uncertainty (less than 0.2%). With a 40 ab^{-1} sample having 20 ab^{-1} with 70% left-handed beam electrons and 20 ab^{-1} with 70% right-handed, the total uncertainty would be 1.5%.

2.2 Tau Pair A_{LR}

A high-purity ($> 98\%$ purity) sample of $e^+e^- \rightarrow \tau^+\tau^-$ events with reasonable efficiency can be obtained with a selection in which cross-feeds between τ decay modes are ignored in the optimization process, since the A_{LR}^τ measurement is insensitive to such cross-feeds. Note that this is not the approach taken in many published τ analyses, as well as the selection in the Tau Polarimetry section of this white paper, where backgrounds from cross-feeds are required to be minimized.

Such a selection approach that ignores cross-feeds has been developed by considering the following τ decay modes: $\tau^\pm \rightarrow e^\pm\nu\nu$, $\tau \rightarrow \mu^\pm\nu\nu$, $\tau^\pm \rightarrow h^\pm\nu$, $\tau^\pm \rightarrow h^\pm\pi^0\nu$, $\tau^\pm \rightarrow h2\pi^0\nu$, and $\tau^\pm \rightarrow 3h^\pm\nu$. Here, h is a charge pion or kaon.

Considering the following mutually exclusive selections that require one of the τ 's to decay leptonically:

- Events with $\tau^\pm \rightarrow e^\pm\nu\nu$ and $\tau^\mp \rightarrow \mu^\mp\nu\nu$. BaBar MC studies indicated this has a 58% selection efficiency, excluding branching fractions, and 99% purity. Including the branching fractions factor, this selects 3.6% of $e^+e^- \rightarrow \tau^+\tau^-$ events.
- $\tau^\pm \rightarrow e^\pm\nu\nu$ and τ^\mp decays to any of the above listed semileptonic decay modes (i.e. the above listed modes except $\tau^\mp \rightarrow e^\mp\nu\nu$ or $\tau^\mp \rightarrow \mu^\mp\nu\nu$). Based on a similar inclusive $\tau^+\tau^-$ event selection described in reference [14], this is expected to have an efficiency (excluding the branching fractions factor), of 63% with a 99% purity. It would select 13% of τ -pair events.
- $\tau^\pm \rightarrow \mu^\pm\nu\nu$ and τ^\mp decays to any of the above listed semileptonic modes. With an efficiency of 50% (99% purity), it selects 10% of τ -pairs.

Combining these three selections alone provide a high purity selection of at least 25% of τ -pair events. Early studies that include a $\tau \rightarrow \rho\nu$ tag, in addition to the leptonic tagged event selection described above, indicate that this can add substantially to the fraction of τ -pair events that can be selected with high purity and that, consequently, the 25% should be considered a lower limit to the fraction of the overall fraction of τ -pair events that can be selected with high purity. The relative statistical uncertainty on $A_{LP}^\tau(\text{measured})$ with 40 ab^{-1} of data (20 ab^{-1} left-handed and 20 ab^{-1} right-handed) would be 2.3%.

As with the muon pair sample discussed in section 2.1, there will be a non-negligible effect on the $A_{LR}^\tau(\text{measured})$ from radiative returns to the $\Upsilon(1S, 2S, 3S) \rightarrow \tau^+\tau^-$ that have an asymmetry equal to A_{LR}^b , which will be measured with a 0.5% relative uncertainty. The rate of production of these states can be determined from studies of the muon pair sample independent of the A_{LR}^μ measurement and the known SM branching fractions of the $\mathcal{B}(\Upsilon(1S, 2S, 3S) \rightarrow \tau^+\tau^-)/\mathcal{B}(\Upsilon(1S, 2S, 3S) \rightarrow \mu^+\mu^-)$ under the assumption of lepton universality, or from direct measurements as in reference [14]. As with the muon pair study, this effect is expected to have a small contribution to the total uncertainty on $A_{LR}^\tau(\text{measured})$, projected to be 2.4% with 40 ab^{-1} of data, with the beam polarization uncertainty the dominant systematic uncertainty.

2.3 Charm and Beauty A_{LR}

2.3.1 Introduction

In order to cleanly separate $e^+e^- \rightarrow c\bar{c}$ events from $e^+e^- \rightarrow b\bar{b}$ events with high efficiency for the separate A_{LR} measurements, we develop $b\bar{b}$ and $c\bar{c}$ selectors that use event-shape variables. Although this approach is sufficient for selecting $b\bar{b}$ events, additional requirements must be imposed in the $c\bar{c}$ selector in order to suppress additional backgrounds arising from non- $b\bar{b}$ sources: light quarks (uds) and τ -pairs.

A machine learning tool is trained to classify between $c\bar{c}$ and $b\bar{b}$ events using the ten most important event-shape variables (as identified by the model). The model chosen for this training is a gradient boosted decision tree (GBDT) with depth of 5, trained over 100 iterations. The model was also trained on a larger number of variables (23), but negligible benefits were found to adding extra variables.

Further selections are tested on the $c\bar{c}$, $b\bar{b}$ events and their backgrounds $u\bar{u}$, $d\bar{d}$, $s\bar{s}$ and $\tau^+\tau^-$ ($uds\tau$) requiring events to have an identified lepton (e^\pm or μ^\pm) as a way to reduce background rates from uds backgrounds in the $c\bar{c}$ sample.

2.3.2 Training and evaluation of the model

Monte Carlo (MC) simulation samples of $b\bar{b}$, $c\bar{c}$ and $uds\tau$ events are collected. Table 2 shows the number of events per sample. The number of events per sample is normalized to the cross section of each process [15].

dataset	charged	mixed	$b\bar{b}$	$c\bar{c}$	$u\bar{u}$	$u\bar{u}$	$s\bar{s}$	$\tau^+\tau^-$
MC number	268591	253669	522260	661033	798314	199454	190501	457103
Reconstructed	268580	253659	522239	646343	788986	197119	180206	457102

Table 2: Number of events generated and reconstructed in each simulation sample. The $b\bar{b}$ events are separately simulated as charged (B^+B^-) and mixed ($B^0\bar{B}^0$) and are shown separately next to the total number of $b\bar{b}$.

The events are reconstructed without any decay requirements, and event-shape variables are calculated based on every candidate particle available in the event. Table 3 shows the ten event-shape variables used for training with their relative importance.

The following figures show the correlation matrix of the different event-shape variables for the different simulation samples. The $c\bar{c}$ simulation is shown in figure 3, the $b\bar{b}$ (B^\pm) simulation is shown in figure 4 and the $b\bar{b}$ (B^0) simulation is shown in figure 5.

Once trained, the GBDT is used to predict if an event is from a $c\bar{c}$ event or a $b\bar{b}$ event. Figure 6 shows the output distribution of the GBDT model when classifying a validation sample.

2.3.3 Evaluation

The performance of the GBDT model is evaluated on two distinct tasks: the identification of $c\bar{c}$ and $b\bar{b}$ events. The performance is obtained using two Receiver Operating Characteristic (ROC) curves and their associated Area Under the Curve (AUC). The ROC curve is expressed using efficiencies and fake rates as defined in equation 4

Variable	Feature Importance
foxWolframR2	0.590
thrust	0.184
foxWolframR1	0.081
harmonicMomentThrust0	0.060
thrustAxisCosTheta	0.039
harmonicMomentCollision2	0.020
foxWolframR3	0.010
aplanarity	0.006
harmonicMomentThrust2	0.006
sphericity	0.004

Table 3: Importance of the variables as calculated by the GBDT, ordered by decreasing importance. The importance metric has arbitrary units and is used to quantify the decision weight of the variable during GBDT decisions.

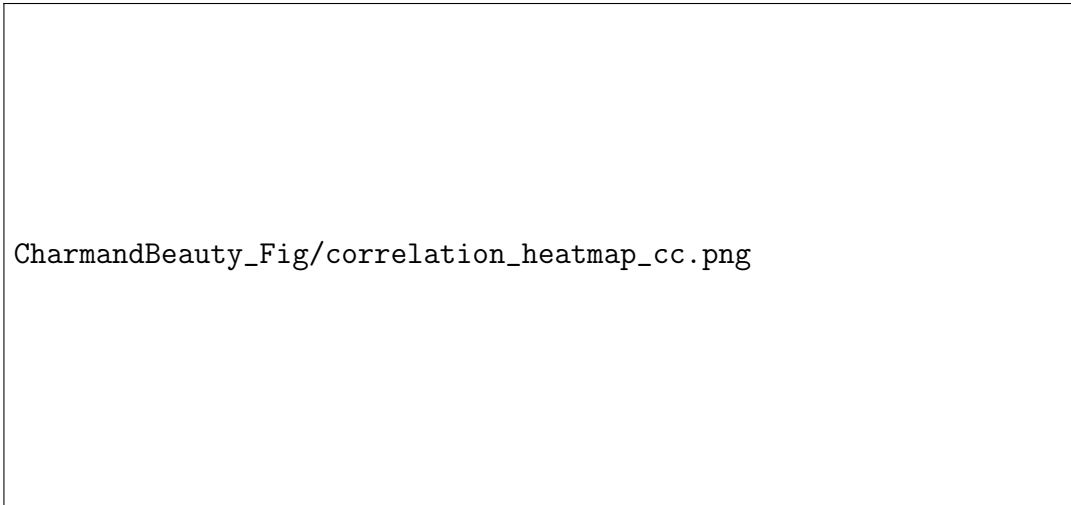
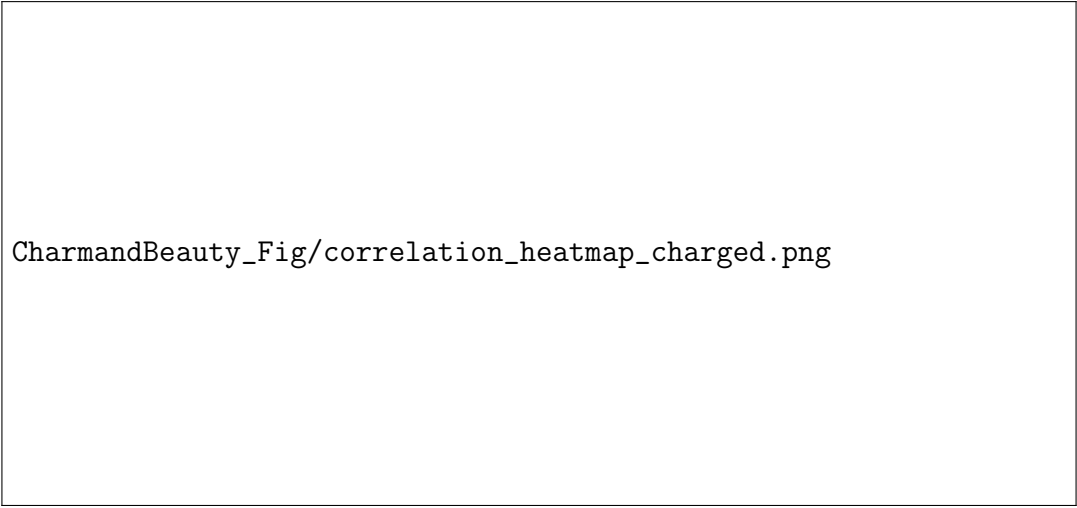


Figure 3: Correlation matrix for the event-shape variables of the $c\bar{c}$ simulation.

$$b\bar{b} \text{ Efficiency} = \frac{\# \text{ of real } b\bar{b} \text{ predicted as } b\bar{b}}{\# \text{ total number of MC generated } b\bar{b}} \quad (4)$$

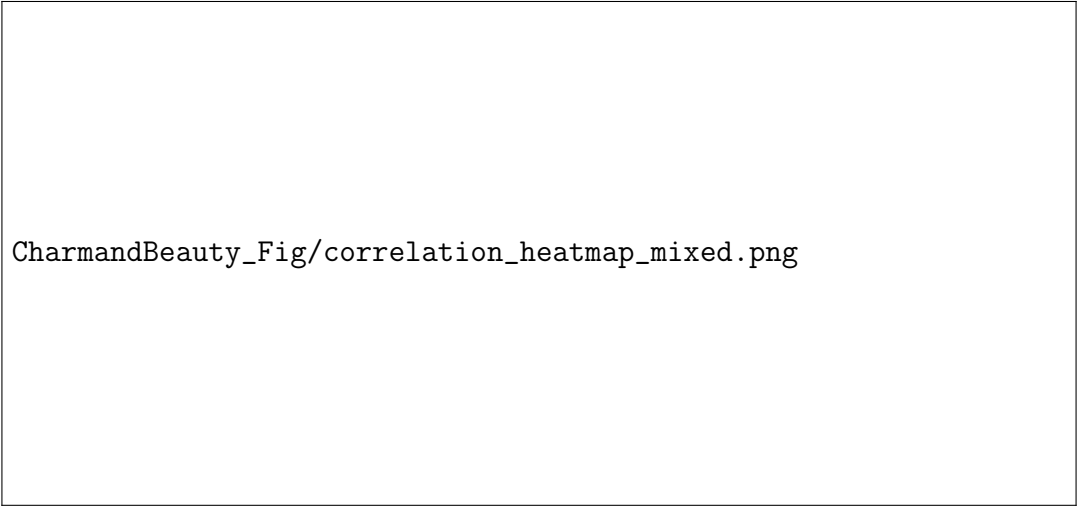
$$c\bar{c} \text{ Fake rate} = \frac{\# \text{ of real } c\bar{c} \text{ misidentified as } b\bar{b}}{\# \text{ total number of MC generated } c\bar{c}} \quad (5)$$

Figure 7 shows the ROC curves calculated on a validation sample of $c\bar{c}$ and $b\bar{b}$. The figures show that the model can discriminate between $c\bar{c}$ and $b\bar{b}$ events with high purity.



CharmandBeauty_Fig/correlation_heatmap_charged.png

Figure 4: Correlation matrix for the event-shape variables of the $b\bar{b}$ (B^\pm) simulation.



CharmandBeauty_Fig/correlation_heatmap_mixed.png

Figure 5: Correlation matrix for the event-shape variables of the $b\bar{b}$ (B^0) simulation.

2.3.4 Classification of $c\bar{c}$

Table 4a shows the fake rate of $c\bar{c}$ at different efficiencies for figure 7a. Only the fake rates of $b\bar{b}$ is shown as $uds\tau$ backgrounds are classified as $c\bar{c}$ events by the GBDT model. Table 4b shows the rates of table 4a converted to number of events per nb^{-1} .

2.3.5 Classification of $b\bar{b}$

Table 5 shows the fake rate of $b\bar{b}$ at different efficiencies for figure 7b. The fake rates of $uds\tau$ backgrounds are included. Table 6 shows the rates of Table 5 converted to number of events per nb^{-1} .

2.3.6 Lepton requirement study

Also explored was whether or not applying a requirement that a muon or electron be present in the event would provide an additional means of reducing the uds backgrounds in the $c\bar{c}$ and $b\bar{b}$ selections. Such cuts can be used separately from the selection of $c\bar{c}$ from $b\bar{b}$ events with the GBDT. Table 7a

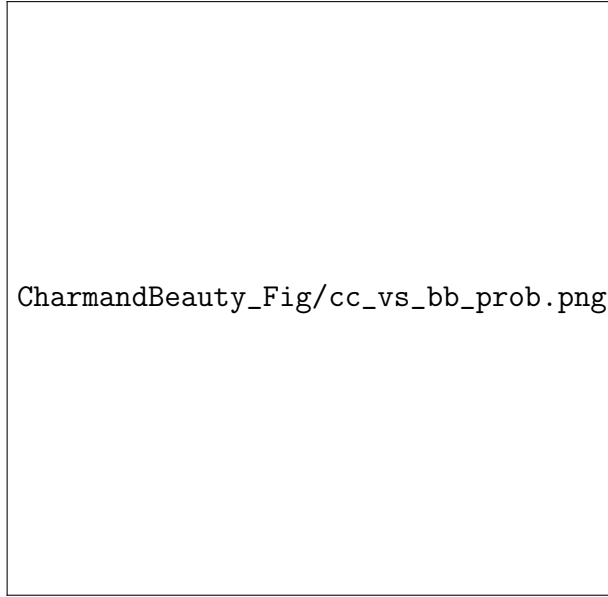


Figure 6: GBDT prediction of events, where the probability is the certainty of the model that the event is a $b\bar{b}$ event. Identified by color are the truth value of a given prediction ($c\bar{c}$ or $b\bar{b}$).

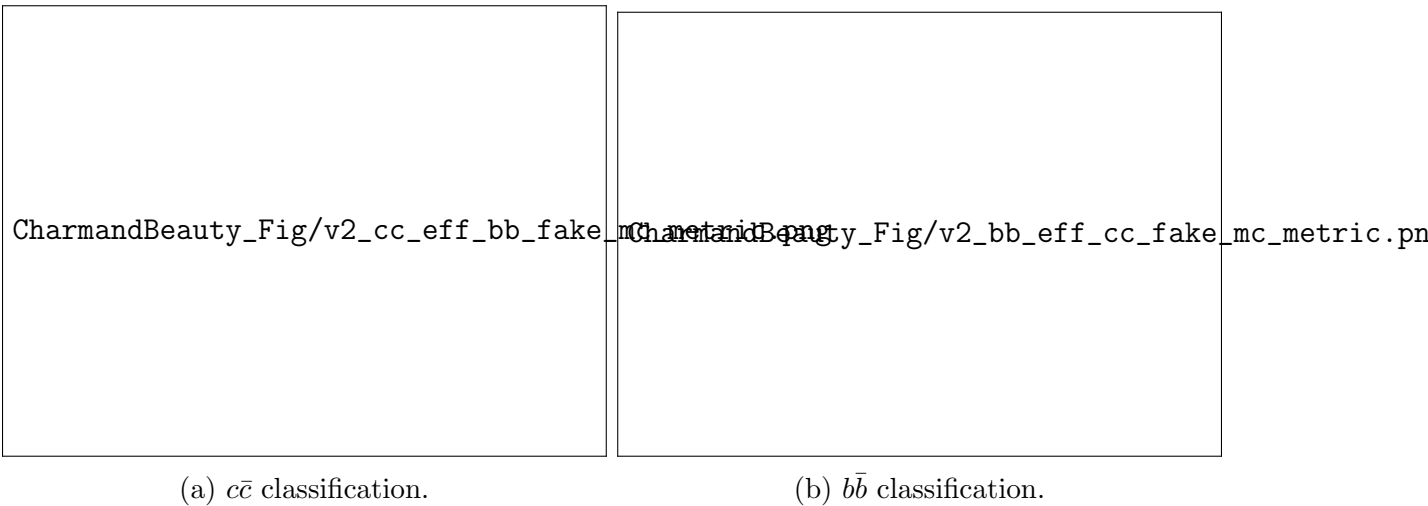


Figure 7: ROC curves of the $c\bar{c}$, $b\bar{b}$ classifier. The definition of fake rates and efficiencies can be found in equation 4.

shows the fraction of events kept after requiring the event to have a lepton (μ^\pm or e^\pm). Table 7b shows the fraction of table 7a converted to number of events per nb^{-1} . Although it is evident that uds backgrounds can be partially suppressed using a lepton requirement, higher purity against the uds backgrounds will require additional measures to develop a sufficiently pure $c\bar{c}$ sample, such as requiring the presence of a charm meson.

2.3.7 Beauty A_{LR}

For the $b\bar{b}$ sample, a GBDT requirement alone that provides a 30% efficiency that has an 88% purity, with half of the backgrounds coming from $c\bar{c}$. Studies with data below the $\Upsilon(4S)$ resonance will enable these backgrounds to be measured precisely, and therefore they would introduce a $\mathcal{O}(0.1\%)$ systematic uncertainty on A_{LR} for $b\bar{b}$. The statistical error would be significantly below that and

Fraction		Events per nb ⁻¹	
$c\bar{c}$ efficiency	$b\bar{b}$ fake rate	$c\bar{c}$	$b\bar{b}$
0.102	0.000	0.133	0.000
0.201	0.002	0.261	0.002
0.301	0.005	0.391	0.006
0.402	0.010	0.523	0.011
0.500	0.020	0.650	0.022
0.599	0.037	0.779	0.041
0.700	0.069	0.910	0.077
0.800	0.138	1.040	0.153
0.900	0.311	1.170	0.345
0.979	0.998	1.273	1.108

(a) Efficiency and fake rates.

(b) Number of events selected as $c\bar{c}$.Table 4: Classification of $c\bar{c}$ events against $b\bar{b}$ events. These tables show the results from figure 7a.

Fraction						
Efficiency	Background Fraction	Fake Rate				
		$c\bar{c}$	$u\bar{u}$	$d\bar{d}$	$s\bar{s}$	$\tau^+\tau^-$
0.098	0.088	0.003	0.002	0.002	0.002	0.002
0.196	0.091	0.008	0.004	0.004	0.004	0.002
0.301	0.110	0.015	0.008	0.008	0.008	0.003
0.401	0.128	0.024	0.013	0.013	0.014	0.003
0.501	0.153	0.038	0.020	0.020	0.022	0.003
0.599	0.181	0.056	0.029	0.030	0.032	0.004
0.699	0.221	0.083	0.044	0.046	0.050	0.004
0.800	0.281	0.130	0.070	0.073	0.079	0.006
0.900	0.380	0.226	0.124	0.131	0.144	0.014
0.998	0.802	0.979	0.966	0.966	0.941	0.996

Table 5: Efficiency and fake rates for the classification of $b\bar{b}$. This table shows the results from figure 7b.

the dominant uncertainty would arise from the systematic error of the measurement of the beam polarization. As shown in the Tau Polarimetry section, the systematic component of the uncertainty that can be achieved is 0.3%. Assuming this is 100% correlated across running periods, it can be used as a reliable estimate of the overall systematic uncertainty that can be achieved. Concerning the statistical component of the polarization, with a 20 ab⁻¹ sample, which consists of 10 ab⁻¹ of

Events selected as $b\bar{b}$ per nb^{-1}					
$b\bar{b}$	$c\bar{c}$	$u\bar{u}$	$d\bar{d}$	$s\bar{s}$	$\tau^+\tau^-$
0.109	0.004	0.003	0.001	0.001	0.002
0.218	0.010	0.006	0.002	0.002	0.002
0.334	0.020	0.013	0.003	0.003	0.003
0.445	0.031	0.021	0.005	0.005	0.003
0.556	0.049	0.032	0.008	0.008	0.003
0.665	0.073	0.047	0.012	0.012	0.004
0.776	0.108	0.071	0.018	0.019	0.004
0.888	0.169	0.113	0.029	0.030	0.006
0.999	0.294	0.200	0.052	0.055	0.013
1.108	1.273	1.555	0.386	0.358	0.915

Table 6: Events selected as $b\bar{b}$ per nb^{-1} for the classification of $b\bar{b}$.

Fraction							Events per nb^{-1}						
Type	MC Truth			ID Cuts			Type	MC Truth			ID Cuts		
	μ	e	Total	μ	e	Total		μ	e	Total	μ	e	Total
$b\bar{b}$	0.26	0.27	0.40	0.33	0.22	0.41	$b\bar{b}$	0.29	0.30	0.45	0.36	0.24	0.46
$c\bar{c}$	0.13	0.16	0.28	0.25	0.12	0.34	$c\bar{c}$	0.17	0.21	0.36	0.32	0.15	0.44
$u\bar{u}$	0.02	0.06	0.08	0.16	0.05	0.20	$u\bar{u}$	0.04	0.10	0.13	0.25	0.07	0.31
$d\bar{d}$	0.02	0.06	0.08	0.16	0.05	0.20	$d\bar{d}$	0.01	0.02	0.03	0.06	0.02	0.08
$s\bar{s}$	0.02	0.05	0.07	0.14	0.04	0.17	$s\bar{s}$	0.01	0.02	0.03	0.05	0.01	0.07
$\tau^+\tau^-$	0.25	0.27	0.47	0.27	0.21	0.45	$\tau^+\tau^-$	0.23	0.24	0.44	0.25	0.20	0.41

(a) Fraction of events containing at least one lepton. (b) Number of events containing at least one lepton.

Table 7: Simulation sets containing at least one lepton. The sets are selected using cuts: truth is the number MC generated number of events with leptons. ID cuts uses a cut on the default particle identification tool (>0.95) and on E/p (>0.85 electron).

left-handed beam electrons and 10 ab^{-1} of right-handed beam electrons, the statistical error would project to be less than 0.1%. For a 70% beam polarization, these translate into a 0.4% relative uncertainty on the beam polarization, which will dominate the precision with which the A_{LR} for $b\bar{b}$ can be measured.

2.3.8 Charm A_{LR}

A $c\bar{c}$ sample can be obtained that has an efficiency of 50% and $b\bar{b}$ background that is only 3% of the combined number of $c\bar{c}$ and $b\bar{b}$ events selected. However, additional requirements are required to suppress large $uds\tau$ backgrounds. For example, requiring the presence of a charm meson in the

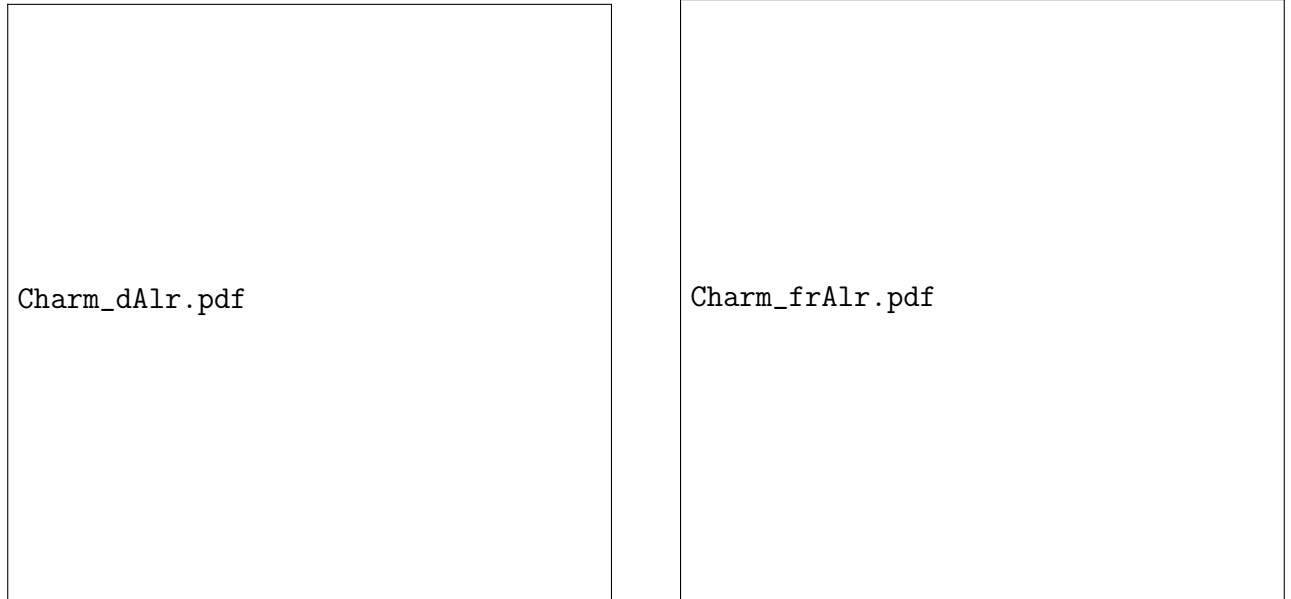


Figure 8: Left: absolute uncertainty on A_{LR} obtained by reconstructing Cabibbo-favored $D^{*+} \rightarrow D^0\pi^+$, $D^0 \rightarrow K^-\pi^+$, $K^-\pi^+\pi^0$, $K^-\pi^+\pi^+\pi^-$ decays, and $D^{*+} \rightarrow D^+\pi^0$, $D^+ \rightarrow K^-\pi^+\pi^+$ decays. Right: the corresponding fractional uncertainty on A_{LR} in percent, assuming $A_{LR} = 0.00546$.

event would provide a high purity $c\bar{c}$ sample. If one assumes a 30% efficiency to find any charm meson, this would provide a 15% overall efficiency for selecting a $c\bar{c}$ sample, and with 40 ab^{-1} of data leads to a 0.3% relative statistical error on A_{LR} for $c\bar{c}$. This would be less than the 0.4% relative uncertainty coming from the systematic uncertainty from the beam polarization, described above. Under these assumptions, the total relative uncertainty would be 0.6% with 20 ab^{-1} of data and 0.5% with 40 ab^{-1} . The development of an efficient charm meson finder forms part of the next steps in the R&D program.

One can obtain a conservative estimate for the precision on A_{LR} that can be obtained by scaling the signal yields of charm decays reconstructed at Belle and Belle II [16, 17]. We consider the Cabibbo-favored decays $D^0 \rightarrow K^-\pi^+$, $K^-\pi^+\pi^0$, $K^-\pi^+\pi^+\pi^-$, and $D^+ \rightarrow K^-\pi^+\pi^+$. To reduce backgrounds from non- $c\bar{c}$ sources, we require that the D^0 and D^+ mesons originate from $D^{*+} \rightarrow D^0\pi^+$ and $D^{*+} \rightarrow D^+\pi^0$ decays. For these decay modes, the purity of the Belle and Belle II samples ranged from 91-99%. The resulting uncertainty on A_{LR} is plotted in Fig. 8. The figure shows that a fractional uncertainty of below 1% could be obtained with $> 20 \text{ ab}^{-1}$ of data for each beam polarization.

2.4 Bhabha A_{LR}

The A_{LR} behaviour in the Bhabha events ($e^+e^- \rightarrow e^+e^-$) differs from the other final state fermions due to the presence of t-channel scattering. A detailed NLO calculation of A_{LR} for Bhabhas has been carried out by Aleksejevs *et. al.*[18]. A luminosity paper has been published by the Belle II collaboration[19], and includes the detector efficiency for collecting Bhabhas. Belle II reports a high purity selection with an efficiency of 36% for an angular acceptance corresponding to a cross section of 17.4 nb. From these results the expected value of A_{LR}^e is $+1.5 \times 10^{-4}$, and with a 40 ab^{-1} data sample and 70% beam polarization, a relative statistical uncertainty of 2% is projected. This 2% relative uncertainty is expected to be statistically dominated. This would translate into a uncertainty of 0.0003 for a measurement of $\sin^2\theta_W$ using only the Bhabhas, and similarly an

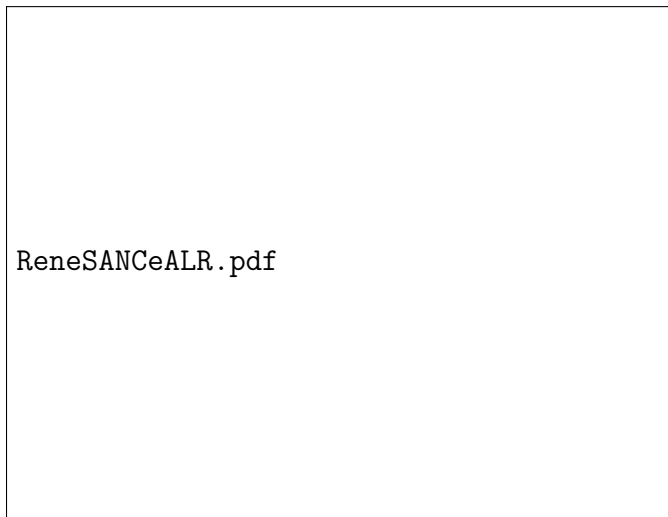


Figure 9: Distribution of A_{LR} in Bhabhas with an angular acceptance of $-\cos a$ to $\cos a$

uncertainty of 0.0006 on a measurement of g_V^e . Initial studies comparing the NLO value of A_{LR} to the ReneSANCe MC generator[20] have been carried out. The preliminary results from the generator show good agreement on the behaviour of A_{LR} over the angular acceptance as shown in Figure 9. Further studies are being carried out to determine if the small difference between the two approaches is related to differences in variable definitions or reflects the level of uncertainty in the NLO calculations.

3 Tau $g - 2$

So far, a test of physics beyond the SM (BSM) via a measurement of the anomalous magnetic moment of the τ , a_τ , has proven elusive, with current limits not precise enough to even resolve the Schwinger term in the QED expansion [21, 22]. Meanwhile, given the current tension in a_μ [23, 24], such a test would provide valuable complementary information in case the muonic tension did signal contributions from new particles or interactions. However, for a meaningful BSM test, a_τ needs to be probed at the level of 10^{-6} , a conclusion that derives from scaling the possible BSM contribution to a_μ with the square of the lepton masses as expected in Minimal Flavor Violation, from the size of the electroweak contribution [25], and from the study of concrete BSM scenarios [26].

Reaching such a level of precision is challenging, but could potentially be achieved at a SuperKEKB upgrade with polarized electrons in a precision study of $e^+e^- \rightarrow \tau^+\tau^-$ at or around the Υ resonances. Such measurements at $s \simeq (10 \text{ GeV})^2$ allow one to extract the Pauli form factor F_2 at the same energy, in such a way that the comparison to the SM prediction reveals a potential BSM contribution. If the associated BSM scale lies beyond the electroweak scale, a mismatch in $\text{Re}(F_2)$ can be directly interpreted as a_τ^{BSM} , while bounds for light BSM degrees of freedom become model dependent.

In order to measure $\text{Re}(F_2^{\text{eff}})$, the effective form factor that can be extracted directly in terms of observable asymmetries, with this procedure requiring the selection of τ -pair events in which both τ^+ and τ^- decay semileptonically: $e^+e^- \rightarrow \tau^+\tau^- \rightarrow h^+\bar{\nu}_\tau h^-\nu_\tau$, which enables the reconstruction of the production plane and direction of flight, as described in Ref. [27]. Polarization is needed because, without it, one can only extract F_2 from the angular dependence of the cross section, which would require controlling the normalization at the 10^{-6} level, or by using the ‘‘Normal Asymmetry’’ as defined in Refs. [28, 29], which is only sensitive to $\text{Im}(F_2)$ [28, 29]. Such approaches will be limited

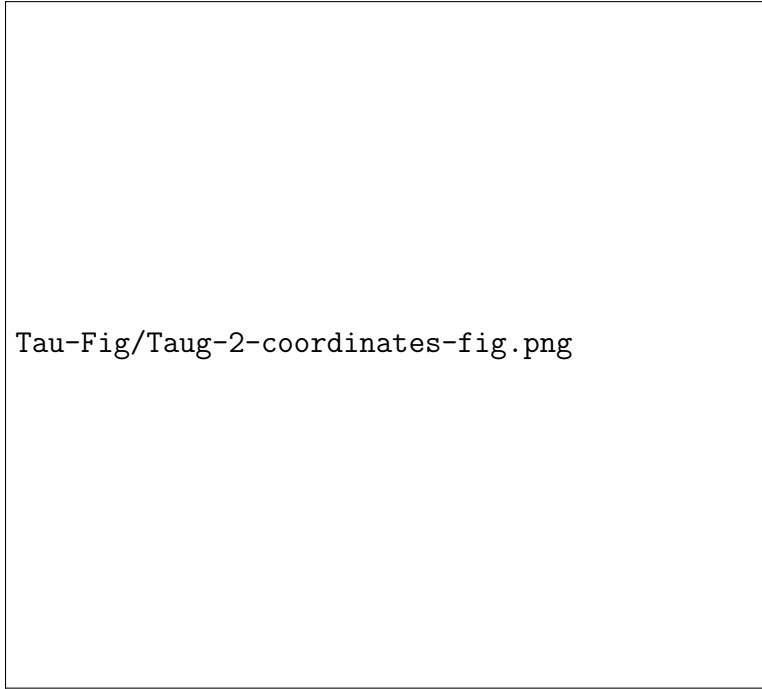


Figure 10: Coordinate system for $e^+e^- \rightarrow \tau^+\tau^-$; $\tau^+ \rightarrow h^+\bar{\nu}_\tau$ and $\tau^- \rightarrow h^-\nu_\tau$ events used in $\tau g-2$ and EDM measurements [31]. Here the z -axis is aligned with τ^- momentum, θ_{τ^-} is the production angle of the τ with respect to the beam electron direction in the center-of-mass, and the azimuthal and polar angles of the produced hadrons, h^\pm , in τ^\pm rest frame, are ϕ_\pm and θ_\pm^* , respectively. The tau production plane and direction of flight are fully reconstructed using the technique described in Ref. [27].

by systematic uncertainties associated with modeling the detector asymmetries that do not cleanly cancel.

In contrast, with a polarized beam, asymmetries between data taken with a left-polarized and right-polarized beam benefit from cancellations of systematic uncertainties associated with the detector asymmetries, since it is the beam that is changing polarization state under identical detector responses. Two left-right beam polarization asymmetries are used, a transverse (A_T) and a longitudinal (A_L) asymmetry, as suggested in Ref. [28], and described below. A particular linear combination of A_T and A_L cancels large contributions from F_1 and is proportional to the effective $\text{Re}(F_2)$:

$$\text{Re}(F_2^{\text{eff}}) = \mp \frac{8(3 - \beta^2)}{3\pi\gamma\beta^2\alpha_\pm} \left(A_T^\pm - \frac{\pi}{2\gamma} A_L^\pm \right), \quad (6)$$

where the \pm refers to the charge on the τ being considered, $\alpha_\pm \equiv (m_\tau^2 - 2m_{h^\pm}^2)/(m_\tau^2 + 2m_{h^\pm}^2)$ is the polarization analyzer [30], and $\gamma = 1/\sqrt{1 - \beta^2} = E_\tau/m_\tau$.

Using the coordinate systems defined in Fig. 10, the transverse asymmetry for the τ^+ (and separately for the τ^-) is measured by counting events with $\pi/2 < \phi_\pm < 3\pi/2$ when the beam is right-polarized (R_e) and also when the beam is left-polarized (L_e) and, taking their difference, then doing the same for events with $-\pi/2 < \phi_\pm < \pi/2$. Subtracting the former from the latter gives A_T^\pm :

$$A_T^\pm = \frac{1}{2\sigma} \left[\int_{-\pi/2}^{\pi/2} \left(\left(\frac{d\sigma^{R_e}}{d\phi_\pm} \right) - \left(\frac{d\sigma^{L_e}}{d\phi_\pm} \right) \right) d\phi_\pm - \int_{\pi/2}^{3\pi/2} \left(\left(\frac{d\sigma^{R_e}}{d\phi_\pm} \right) - \left(\frac{d\sigma^{L_e}}{d\phi_\pm} \right) \right) d\phi_\pm \right]. \quad (7)$$

The longitudinal asymmetry measurement involves the R_e - L_e asymmetries as well, along with the asymmetries associated with two angular observables ($z = \cos\theta_{\tau^-}$ and $z_\pm^* = \cos\theta_\pm^*$), after

integrating over all other angles. Defining

$$A_{RL} = \frac{d^2\sigma^{R_e}}{dz_{\pm}^* dz} - \frac{d^2\sigma^{L_e}}{dz_{\pm}^* dz}, \quad (8)$$

the longitudinal asymmetry is:

$$A_L^{\pm} = \frac{1}{2\sigma} \left[\int_0^1 dz_{\pm}^* \left(\int_0^1 dz (A_{RL}) - \int_{-1}^0 dz (A_{RL}) \right) - \int_{-1}^0 dz_{\pm}^* \left(\int_0^1 dz (A_{RL}) - \int_{-1}^0 dz (A_{RL}) \right) \right]. \quad (9)$$

In order to measure A_L^{\pm} , for each beam polarization state (R_e or L_e), the experiment counts the events in four bins separately for the identified τ^+ and τ^- :

- $N_{\pm}^{FF}(R_e \text{ or } L_e)$: number of τ^{\pm} decays with $0 < \cos \theta_{\tau^-} < 1$ and h^{\pm} in $0 < \cos \theta_{\pm}^* < 1$;
- $N_{\pm}^{FB}(R_e \text{ or } L_e)$: number of τ^{\pm} decays with $0 < \cos \theta_{\tau^-} < 1$ and h^{\pm} in $-1 < \cos \theta_{\pm}^* < 0$;
- $N_{\pm}^{BF}(R_e \text{ or } L_e)$: number of τ^{\pm} decays with $-1 < \cos \theta_{\tau^-} < 0$ and h^{\pm} in $0 < \cos \theta_{\pm}^* < 1$;
- $N_{\pm}^{BB}(R_e \text{ or } L_e)$: number of τ^{\pm} decays with $-1 < \cos \theta_{\tau^-} < 0$ and h^{\pm} in $-1 < \cos \theta_{\pm}^* < 0$.

Defining the R_e and L_e asymmetries as:

$$\begin{aligned} A_{FF}^{\pm} &= \frac{N_{\pm}^{FF}(R_e) - N_{\pm}^{FF}(L_e)}{N_{\pm}^{FF}(R_e) + N_{\pm}^{FF}(L_e)}, & A_{BF}^{\pm} &= \frac{N_{\pm}^{BF}(R_e) - N_{\pm}^{BF}(L_e)}{N_{\pm}^{BF}(R_e) + N_{\pm}^{BF}(L_e)}, \\ A_{FB}^{\pm} &= \frac{N_{\pm}^{FB}(R_e) - N_{\pm}^{FB}(L_e)}{N_{\pm}^{FB}(R_e) + N_{\pm}^{FB}(L_e)}, & A_{BB}^{\pm} &= \frac{N_{\pm}^{BB}(R_e) - N_{\pm}^{BB}(L_e)}{N_{\pm}^{BB}(R_e) + N_{\pm}^{BB}(L_e)}, \end{aligned} \quad (10)$$

the longitudinal asymmetry for the τ^{\pm} is then:

$$A_L^{\pm} = \frac{1}{2} [(A_{FF}^{\pm} - A_{BF}^{\pm}) - (A_{FB}^{\pm} - A_{BB}^{\pm})]. \quad (11)$$

Note that the unpolarized cross section, after integration over ϕ_{\pm} , no longer depends on θ_{\pm}^* and is further symmetric in z , in such a way that in Eq. (10) each term can indeed be normalized to the sum of events in each bin separately. The same holds true for A_T^{\pm} , as the unpolarized cross section does not distinguish between the two regions in ϕ_{\pm} either.

In the SM at 10 GeV, $\text{Re}(F_2^{\text{eff}}) = -268.77(50) \times 10^{-6}$ [26]. Consequently, the factor $\frac{8(3-\beta^2)}{3\pi\gamma\beta^2\alpha_{\pm}}$ in Eq. 6 only needs to be controlled at the 0.5% level in order to achieve a ppm measurement. However, the cancellation of the large contribution from F_1 , which motivates the subtraction $(A_T^{\pm} - \frac{\pi}{2\gamma} A_L^{\pm})$, requires the $\pi/(2\gamma)$ factor to be very well controlled. Since $\gamma = E_{\tau}/m_{\tau} = E_{\text{cm}}/(2m_{\tau})$, its uncertainty is determined by the uncertainties on the τ mass and mass of the $\Upsilon(1S)$, which is used to calibrate the center-of-mass energy in the machine. Current uncertainties on m_{τ} and $M_{\Upsilon(1S)}$ [32] limit this precision to 1×10^{-5} . This contribution to the overall uncertainty on the precision of $\text{Re}(F_2^{\text{eff}})$ will scale in proportion with the uncertainties of the measurements on m_{τ} and $M_{\Upsilon(1S)}$, and therefore motivates improved measurements of those quantities.

With 40 ab^{-1} of $e^+e^- \rightarrow \tau^+\tau^-$ data, requiring both the τ^+ and τ^- to decay semileptonically and assuming a 60% selection efficiency, the statistical error on $\text{Re}(F_2^{\text{eff}})$ would be 1×10^{-5} . As both A_T and A_L involve differences in the polarization state of the beam, the dominant detector systematic uncertainties cancel and one is left dealing with the detector related systematic uncertainties in the

residual differences. These can be accurately controlled in analyses that do not use the beam polarization information. Consequently, the measurements of A_T and A_L at a polarization-upgraded SuperKEKB constitutes a promising way to precisely measure a_τ . The path towards eventually constraining a_τ^{BSM} at the 10^{-6} level will require more statistics as well as higher precision measurements of m_τ and $M_{\Upsilon(1S)}$.

Key requirements for such a program are studied in Ref. [26]: first, a precision of 10^{-6} necessitates the consideration of two-loop effects, as provided therein for the resonance-enhanced case of a measurement on the $\Upsilon(nS)$, $n = 1, 2, 3$. However, the typical spread in beam energies results in the continuum $\tau^+\tau^-$ pairs to dominate over resonant ones, and such a measurement would require significant dedicated runs on the lower Υ resonances to gather enough statistics. On the other hand, the broader physics program calls for most data to be collected at the center-of-mass energy of $\Upsilon(4S)$ mass, where $e^+e^- \rightarrow \tau^+\tau^-$ events are produced non-resonantly, since the $\Upsilon(4S)$ has a negligible leptonic branching fraction. Given that this non-resonant data would allow for a significant increase in statistics, and translate to improved limits on a_τ^{BSM} , this strongly motivates the full two-loop calculation in the coming years.

4 Tau EDM

The electric dipole moment (EDM, d_τ) of the τ lepton characterizes the time-reversal or charge-parity (CP) violation properties at the $\gamma\tau\tau$ vertex. The SM predicts an extremely small value, $d_\tau \approx 10^{-37}$ ecm [33, 34], many orders of magnitude below any experimental sensitivity. Independent measurements of the electric dipole moments of e , μ and τ are necessary to determine the flavor dependence of CP violating phases in the possible mixing between three generation of the charged lepton sector. In general, the strength of CP violation may be different for different flavors and Belle II is uniquely suited to test a large class of new physics models which predict enhanced contributions in EDM of the τ lepton at observable levels of 10^{-19} ecm [35, 36].

Experimental studies of the τ EDM are very clean tools of discovery of new physics, because they rely on measurement of asymmetries with relatively small systematic uncertainties in the measurement. Current best results are from a recent Belle study [37], where the squared spin-density matrix of the τ production vertex is extended to include contributions proportional to the real and imaginary parts of the τ EDM. The expectation values of the optimal observable were measured yielding $\text{Re}(d_\tau) = (-6.2 \pm 6.3) \times 10^{-18}$ ecm and $\text{Im}(d_\tau) = (-4.0 \pm 3.2) \times 10^{-18}$ ecm. The results are obtained using 833 fb^{-1} of data, with the dominant systematic uncertainty associated to mismatch of data and the simulated distributions of momentum and angular variables. The sensitivity studies on EDM at Belle II has shown that the agreement between data and Monte Carlo can be improved significantly. Conservative assumption on benchmark scenarios of systematic uncertainties at Belle II show that we expect to probe τ EDM at the 10^{-19} level with the 50 ab^{-1} data set.

The τ EDM not only influences the angular distributions, but also the polarization of the τ produced in electron-positron annihilation. The beam polarization substantially improves the experimental sensitivity for τ EDM by allowing measurements of the polarization of a single τ , rather than measurements of correlations between two τ leptons produced in the same event [31, 38]. The proposed beam polarization upgrade at SuperKEKB will further experimental sensitivity, since the uncertainties in modeling the forward-background asymmetry in the detector response are independent of beam polarization and will largely cancel. Such an increase in experimental sensitivity will allow to unambiguously discriminate between the new physics contributions to the τ EDM at the level of 10^{-20} ecm, which is two orders of magnitude below any other existing bounds [31, 39, 40].

5 Tau LFV

Many models predict lepton flavor violation (LFV) in τ decays at 10^{-10} – 10^{-8} levels, which will be probed by the huge data sample of 10^{11} single τ^- decays at Belle II. Upper limits will improve current bounds by an order of magnitude in the next decade, probing LFV in τ decays down to few parts in $10^{-10} - 10^{-9}$ [15]. Substantial gains are possible by re-optimizing the analysis for the Belle II detector, exploiting beam polarization effects. The high energy electrons beam at SuperKEKB are expected to be $\sim 70\%$ longitudinally polarized, influencing the angular distribution of the τ decay products in a way that depends on the interaction that causes LFV. With beam polarization, the helicity angles of the τ pair decay products can be used to significantly suppress the background when one τ decays to $\mu\gamma$ and the other one to $\pi\nu$, which is the decay channel most sensitive to the polarization of the τ lepton. Similar background suppression can also be obtained with the other decay modes, which vary in their sensitivity to the τ polarization. In general, the polar angles in the center-of-mass frame times the charge of the τ decay provide maximal background suppression. The “irreducible background” from $\tau \rightarrow \mu\nu\bar{\nu}\gamma$ decays are studied in Figure 11 [41]. While the distributions of the backgrounds differ significantly with and without beam polarization, the signal distribution modelled by phase-space does not change. By varying the selected set of events based on such a distribution, the background can be reduced significantly, corresponding to a small loss in signal efficiency. An optimization study has shown that this would result in approximately a 10% improvement in the sensitivity. Similar analyses can be expected to yield comparable gain sensitivities for the $\tau \rightarrow e\gamma$ LFV decay mode, based on the published *BABAR* analysis [42]. However, it should be noted that the phase space model of the signal is chosen due to the lack of current knowledge on the underlying theory behind LFV decays. By far, the most important aspect of having the polarization is the possibility to determine the helicity structure of the LFV coupling from the final state momenta distributions, for example in $\tau \rightarrow \mu\mu\mu$ decays [43, 44].

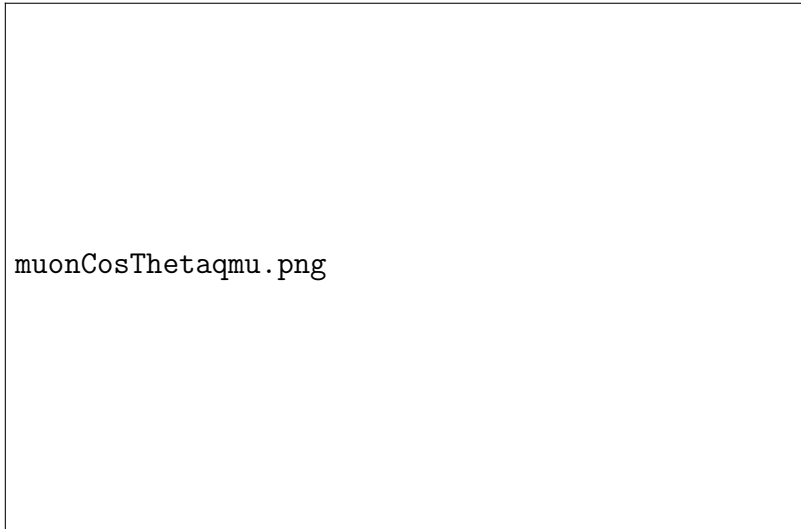


Figure 11: Distribution of the cosine of the angle between the signal-side muon momentum and e^- beam momentum in the center-of-mass frame, multiplied by the muon charge for signal and background events with and without electron beam polarization in the $\tau \rightarrow \mu\nu\bar{\nu}\gamma$ search analysis.



Figure 12: Inclusive DIS (left) and Λ production from SIA (right) diagrams with an inclusive jet correlator Ξ replacing unobserved perturbative quarks in the final state. Φ and Δ^h are the correlation functions that encode information on hadron structure and hadronization, respectively. The jet correlator $J = \frac{1}{2} \int dk^+ \Xi(k)$ is defined in Eq. (12) and further discussed in the main text. In this document, the detected hadron h is a self-polarizing Λ baryon.

6 QCD: Dynamical mass generation studies with polarized beams

Due to color confinement, the quarks created in a hard collision cannot appear as on shell particles in the final state, but rather decay into a jet of hadrons whose mass is dynamically generated, but the details of the quark-to-hadron transition are still unknown. As proposed in [45, 46] dynamical mass generation can be studied even without observing the produced hadrons, but instead studying the Dirac decomposition of the (color averaged) *gauge-invariant* quark correlator

$$\begin{aligned}
 J_{ij}(k^-, \vec{k}_T) &\equiv \frac{\text{Tr}_c}{2N_c} \int dk^+ \text{Disc} \int \frac{d^4\xi}{(2\pi)^4} e^{ik \cdot \xi} \langle \Omega | \psi_i(\xi) \bar{\psi}_j(0) W(0, \xi; n_+) | \Omega \rangle \\
 &= \frac{\theta(k^-)}{4(2\pi)^3 k^-} \left\{ k^- \gamma^+ + \not{k}_T + M_j \mathbb{I} + \frac{K_j^2 + \vec{k}_T^2}{2k^-} \gamma^- \right\}.
 \end{aligned} \tag{12}$$

where $|\Omega\rangle$ is the nonperturbative QCD vacuum, ψ_i is the quark field, W a Wilson line. This correlator describes the nonperturbative propagation and hadronization of a quark [45, 46], and generalizes the perturbative quark propagator contributing to particle production in lepton-nucleus deep inelastic scattering (DIS) at large Bjorken x values [47, 48] as well as in the semi-inclusive annihilation (SIA) of electrons and positrons, see Figure 12.

In particular, In SIA production of a self-polarizing Λ hadron the chiral-odd jet mass M_j couples to the H_1^Λ transversity fragmentation function and contributes to the longitudinal beam spin asymmetry of the process,

$$A_L = \frac{d\sigma^{R_e} - d\sigma^{L_e}}{d\sigma^{R_e} + d\sigma^{L_e}}, \tag{13}$$

where R_e and L_e refer to the handedness of the electron. The Λ 's longitudinal and transverse spin contributions to the asymmetry can be separated studying the $y = P_\Lambda \cdot l / P_\Lambda \cdot q$ dependence of the asymmetry, where l , q , and P_Λ are the four-momenta of the incoming electron, the exchanged photon, and the Λ baryon respectively [49, 50]. Assuming the saturation of the positivity bounds and Wandzura-Wilczek approximation for the polarized leading twist fragmentation functions $G_1^\Lambda(z)$,

$H_1^\Lambda(z)$, and the higher twist $G_T^\Lambda(z)$ fragmentation function [51] one obtains:

$$A_L(y, Q) = \pm \underbrace{\left(\lambda_e \frac{C(y)}{2A(y)} \right)}_{A_L^1(y)} \lambda_\Lambda \pm \underbrace{\left(2\lambda_e \frac{M_j(Q)}{Q} \frac{D(y)}{A(y)} \right)}_{A_L^{\cos\phi}(y, Q)} |S_{T\Lambda}| \cos(\phi) , \quad (14)$$

where λ_e and λ_Λ are the electron's and Λ hadron's helicities, respectively, $S_{T\Lambda}$ is the transverse spin vector of the detected Λ hadron (see the ‘‘Opportunities for precision QCD physics in hadronization at Belle II’’ Snowmass 2022 contribution for details [52]). The \pm signs in Eq. (14) refer to the case where the polarized leading twist fragmentation functions $G_1^\Lambda(z)$, $H_1^\Lambda(z)$ saturate the respective positivity bounds with a plus or a minus sign [51]. The configuration with the plus (minus) sign corresponds to the solid blue (dashed red) curves in Fig. 13.

The jet mass M_j can then be extracted from the Fourier coefficient $A_L^{\cos\phi}$. With the expected 70% beam polarization at the polarized SuperKEKB upgrade, this is found to be of $\mathcal{O}(1\%)$, reaching a maximum at $y = 0.5$. At the same value of y the constant modulation A_L^1 displays a node. This specific value allows one to separate the two modulations A_L^1 and $A_L^{\cos\phi}$, related to the longitudinal and transverse polarization of the detected Λ hadron respectively. The blue band in Fig. 13 displays the sensitivity of this observable to a 20% variation in the jet mass at the non-perturbative scale, $M_{j0} = 0.4 - 0.6$ GeV.

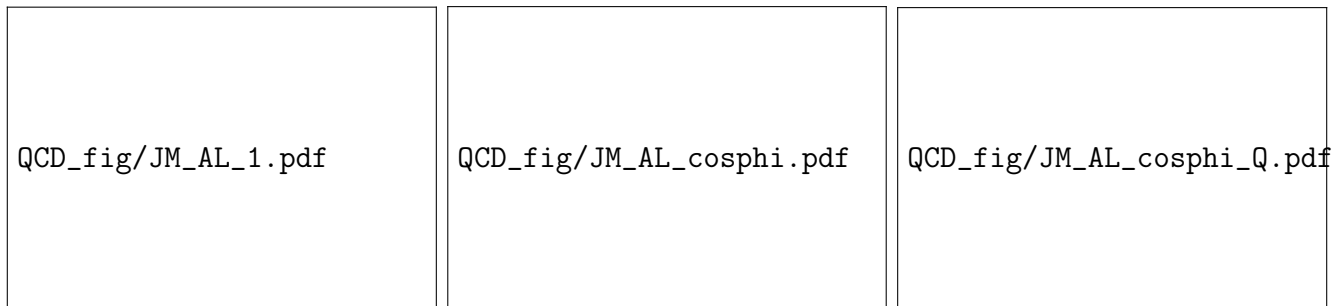


Figure 13: The Fourier components $A_L^1(y)$ and $A_L^{\cos\phi}(y, Q)$ of the longitudinal electron spin asymmetry as a function of y at the SuperKEKB nominal energy $Q = 10.58$ GeV. The band in the $\cos\phi$ modulation indicates the sensitivity of the measurement to $\pm 20\%$ variation in the jet mass at the initial scale. The rightmost panel shows the $A_L^{\cos\phi}$ modulation as a function of Q at fixed $y = 0.5$, along with its 20% sensitivity to M_j , which also slightly increases at lower energies due to QCD evolution.

In summary, the $A_L^{\cos\phi}$ modulation of the beam spin asymmetry A_L in Eqs. (13), (14) for production of a Λ hadron in polarized e^+e^- annihilation provides access to the dynamical component of the jet mass, allowing one to experimentally measure the contribution of the non-perturbative QCD dynamics at play in the hadronization mechanism. If the positivity bounds for the polarized fragmentation functions turn out not to be saturated, the signal may drop below the $\mathcal{O}(1\%)$ estimated in Fig. 13. However, being a twist three effect suppressed as $\sim 1/Q$, the signal and its sensitivity to M_j can increase significantly at lower center of mass energies, as displayed in the right-most panel of Fig. 13. Similar measurements with di-hadron production instead of a self-polarizing Λ baryon are also under consideration.

7 Polarized Source

Development of the polarized source aims at creating and delivering a high-quality beam to the Main Ring via the injector linac. A highly polarized beam is desired, with emission parameters at injection in line with the SuperKEKB’s HER values (see Table 8).

SuperKEKB HER Beam Parameters	
Energy [GeV]	7
Bunch charge [nC]	4
Normalized Emittance [mm · mrad]	40/20 (Hor./Vert.)

Table 8: SuperKEKB Beam Parameters.

7.1 Beam Generation

We consider electron beam generation using a GaAs cathode activated with a circularly-polarized laser. GaAs has been shown since the 1970’s to produce highly polarized electron beams[53]. Strain super-lattice GaAs crystals have been demonstrated to show $\geq 90\%$ polarization with a quantum efficiency of 1.6% [54]. However, the 1.43 eV gap between the valence and conduction bands in GaAs presents an obstacle to efficient acceleration of electrons; application of a thin Negative Electron Affinity (NEA) surface may be used to permit electrons from the conduction band minimum to escape into the vacuum and thence to be accelerated through the beamline.

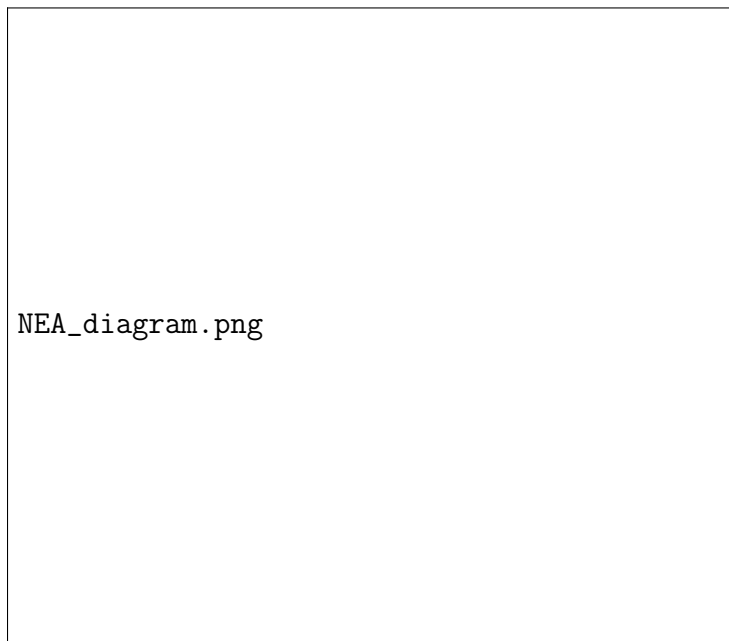


Figure 14: Representation of a GaAs cathode with a thin-film NEA layer.

NEA films are susceptible to several modes of degradation, including residual gas adsorption, ion back bombardment, and thermal desorption, and consequently have relatively short lifetimes. As a practical matter, however, this necessitates using a DC electron gun as opposed to the relatively harsh environment of an RF gun. Because the charge density of DC guns is relatively low, a buncher must also be considered to achieve the desired bunch charge.

We are currently investigating increasing the lifetime of NEA cathodes by investigating novel materials in the thin film surface as well as improving the application procedure to produce more robust cathodes. Results from the test bench at Hiroshima University have shown that lifetimes for CsKTe-activated cathodes, for example, have a lifetime approximately one order of magnitude greater than that of previous-generation CsO-activated cathodes, as shown in Table 9.

Cathode	Lifetime [10^{-3} Pa · s]
CsO/GaAs	0.29 ± 0.03
CsO/GaAs	0.40 ± 0.02
CsKTe/GaAs	6.50 ± 0.01

Table 9: Measured lifetimes of thin-film cathodes. Data taken from [55].

7.1.1 Cathode Production and Testing

Cathode production is carried out at the Hiroshima University test bench. GaAs wafers are prepared by washing with an oxygenated ammonium bath (Semicoclean 23 solution) for five minutes, followed by rinsing with distilled water and ethanol and flushing any remaining impurities from the surface with He gas. The wafer is then mounted to a stage and inserted into the vacuum chamber.

The vacuum chamber is baked at 200 °C with a vacuum pump connected to flush outgassed hydrogen. At the level of 10^{-6} Pa, an angle valve is closed and an ion pump is activated to increase the vacuum to approximately 10^{-9} Pa and the cathode is heated again to remove any remaining surface contaminants.

Following baking, NEA surface materials are heated and dispersed evenly into the vacuum chamber and their deposition is monitored at the Ångstrom level. A 50 Å layer of Sb is deposited onto the face of the GaAs wafer directly, after which layers of other materials to be tested are deposited in 5 Å segments.

7.2 Linac Transport

After beam generation, the polarized electrons must be aligned to the vertical configuration and delivered through the injector linac into the HER while maintaining spin polarization. Spin-tracking simulations must thus be carried out to ensure that the polarization is maintained throughout, particularly in the 180° J-arc of the linac and in the beam transport line, which has a vertical displacement of approximately 10 m as well as four horizontal arcs before injection into the HER. An overhead view of the beam transport line is shown in Figure 15.

For purposes of aligning the spin orientation to the vertical, we consider the existing lattice when investigating installation of a spin rotator. Downstream of the beam source sit two focusing-defocusing quadrupole magnet cells and an X-Y steering magnet; before these beam elements, there is approximately 0.9 m of open space which may be possible to use for beam alignment.

Prior to entering the RF cavities traversing the J-arc of the linac, the beam spin vector should be aligned to the vertical to avoid depolarization due to the bend in the linac. To achieve this, we consider the addition of a Wien Filter in the early stages of the linac, immediately after source generation and prior to entering the first RF cell. Although there exists four pairs of vertical bends before the pipe goes into the tunnel, the vertical polarization is re-established by the time the beam enters the HER, due to anti-symmetric structure of the bends, as shown in Figure 16.

Beam dynamics simulations are to be carried out for the entirety of the linac, including spin-tracking; however, while the beam lattice model exists in SAD, spin tracking has not been reliably

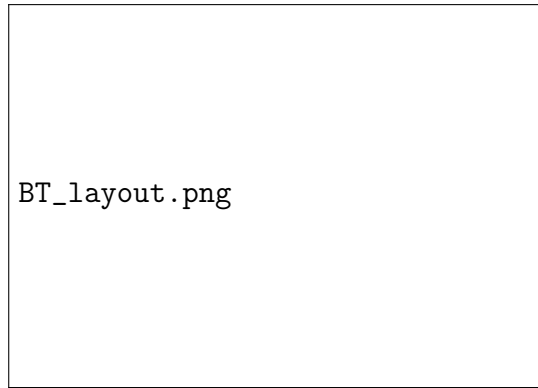


Figure 15: Overhead view of the beam transport lines, showing both electron and positron lines. Only the electron arc is to be polarized.

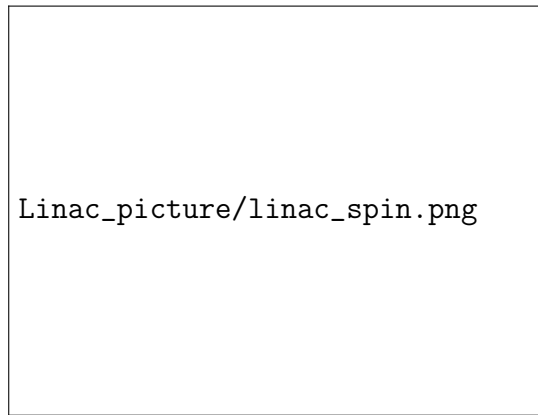


Figure 16: Spin motion of the electron in the Linac section with the beam vertically polarized at the early stage. $s=0\text{m}$ corresponds to the approximate source position and $s = 1100\text{m}$ corresponds to the position of injection into the HER.

demonstrated. An alternate solution to ensure consistency with tracking performed in the HER is to create the same model in BMAD, with simulations performed in the same manner. The goals of this simulation are to ensure that spin polarization can be maintained acceptably up to injection, and also to determine what, if any, changes must be made to the existing setup in order to ensure that such preservation is possible.

8 Beam-Beam Effects on Polarization

The effect of beam-beam interactions on the polarization will have to be studied in simulations. To first-order, the beam-beam effect is a focusing force that affects spin-transparency. At HERA it was observed that the optimum polarization at strong beam-beam required slightly different optimization of the machine but was recoverable to a large extent [56, 57]. Beam-beam in SuperKEKB will be stronger, but only by a modest factor, not by an order of magnitude as the luminosity is increased by extremely small β^* , not by an extremely large beam-beam parameter. We note that the beam-beam effects experienced by the electrons in HERA was not particularly small, due to the strong proton bunches, and was one of the factors limiting the luminosity [58]. At SuperKEKB, with short beam lifetime and constant injection of freshly polarized electrons, a high equilibrium polarization is a realistic expectation.

9 Spin Rotator

Three approaches for implementing spin rotators into the HER are presented. Two approaches are described in the “BINP Spin Rotator Concepts” subsection, in which a modest conversion of the geometry of electron beam bends in the experimental section of the HER storage ring to provide drift gaps with a length of about 10 m for installing spin rotators, are proposed. One BINP approach uses a conventional spin rotator with separate solenoid and quadrupole magnets and the second makes use of combined function solenoid-quadrupole magnets. The third approach is described in the subsection entitled “Dipole-Solenoid-Quadrupoles Combined Function Magnets Concept”, in which four existing dipoles on either side of the IP are replaced with dipole-solenoid-quadrupoles combined function spin rotator magnets that can be constructed using the direct wind technology used at BNL with the intention of minimizing changes to the HER lattice. So far, these approaches indicate that implementing spin rotators in the HER is feasible and the next step in this R&D program is to perform long-term particle tracking studies to determine whether or not the dynamic aperture with spin rotators has worsened in comparison with the version of the ring optics without spin rotators.

9.1 BINP Spin Rotator Concepts

This section discusses how to implement a Spin Rotator within the SuperKEKB lattice. Due to the extremely small coupling coefficient of transverse oscillations in SuperKEKB [59, 60] it would be very challenging to use any spin rotator schemes using transverse dipole fields. Only the scheme with the use of a longitudinal magnetic field has no effect on the value of the vertical emittance, which is formed by quantum fluctuations of synchrotron radiation in the main dipole magnets of the ring and by parasitic coupling of transverse oscillations.

9.1.1 The concept of a scheme for obtaining longitudinal polarization

Below, we discuss the simplest version of such a scheme of rotations of the direction of the electron spin vector, when the vertical direction of the spin in the main arcs is completely restored when the beam passes through a long experimental straight section of the HER ring, see Figure 17.

The left and right spin rotators have the opposite sign of the longitudinal magnetic field, and the whole rotation scheme is generally antisymmetric in the signs of magnetic fields at an equilibrium orbit. This antisymmetry ensures almost complete absence of the dependence of the spin orientation in the loops on the particle energy, which is very important for obtaining a long beam depolarization time. The presence of a nonzero dispersion function in spin rotators and magnets between them does not allow to completely suppress the chromatic energy dependence of the spin orbit in the loops. We will discuss this issue in greater details later.

To rotate the electron spin by 90 degrees, the field integral in the solenoids is proportional to the particle momentum:

$$Bl = \frac{\pi}{2(1 + a_e)} BR$$

Here $BR = p c/e$ is the magnetic rigidity and $a_e = 1.16 \times 10^{-3}$ is the anomalous magnetic moment of an electron. The subsequent rotation of the spin by 90° in the horizontal plane occurs in the section from the rotator to the point of intersection of the beams with the total angle of rotation of the velocity vector equal to:

$$\theta = \frac{\pi}{2\nu_0}$$

BINP_Fig/BINP-SR-Fig1.png

Figure 17: Scheme of spin rotations with restoration of their vertical direction in the main arcs of the ring. Each spin rotator consists of two solenoids and several skew-quadrupole lenses that compensate for the coupling of betatron oscillations introduced by these solenoids.

where $\nu_o = \gamma a_e$ is the dimensionless spin frequency (or tune) proportional to the gamma factor of the particle.

To detune from resonances with betatron oscillation frequencies, which can quickly depolarize the beam due to beam-beam collision effects, we chose the optimal value of the electron energy equal to $E = 7.15$ GeV, which corresponds to the spin tune $\nu_0 = 16.226$ which is sufficiently distant both from close to half-integer values of transverse oscillation frequencies, and from integer resonances with their synchrotron satellites. This value of the spin tune dictates to us the required total angle of all turns in the horizontal plane from the rotator to the interaction point equal to $\theta = 0.0968$.

In the current geometry of the complicated wavy HER orbit, there is no suitable place for a spin rotator. Moreover, given that the length of the rotator is about 10 meters, several dipoles had to be moved from their places, simultaneously changing their angles of rotation. Such transformations of the long insertion connecting the left and right arches were calculated and optimized taking into account the preservation of the storage ring perimeter. The geometries of the separation of the trajectories of the LER and HER rings are slightly different on the left and right sides from the interaction point, see respectively Fig. 18 and 19.

In a condensed form, the scheme of intersection of the collider rings is shown in Fig. 20.

Note that due to a significant change in some of the rotation angles, the lengths of the corresponding dipoles also changed. In the new scheme, the number of long dipoles is increased by two units, while the number of short dipoles is decreased also by two units. We note that the right half of the long experimental region in the new geometry is lengthened by 14 mm, which is fully compensated by the corresponding shortening of its left half. Spin rotators are inserted into specially widened gaps about 10 m long, between the structural blocks of compensation for the local chromaticity of the triplets of the strong final quadrupole lenses. Each such SX or SY-block[59] consists of a pair of identical dipole magnets and symmetrically spaced quadrupole lenses, which provide minus-unity of the diagonal elements of the transport matrix of the section between the

BINP_Fig/BINP-SR-Fig2.png

Figure 18: To the left from the IP half of experimental straight section. The modified magnetic elements of the HER ring are painted in dark brown, and the solenoids of the spin rotator are painted in dark yellow. The distance between the rings is great

BINP_Fig/BINP-SR-Fig3.png

Figure 19: To the right from the IP half of straight section. At the entrance to the tunnel, the magnets of the rings are very close, but such technical problems can be solved.

BINP_Fig/BINP-SR-Fig4.png

Figure 20: Optimized SuperKEKB ring intersection scheme for longitudinal polarization. Spin rotators are located in convenient places, away from the tunnel walls and the magnetic elements of the positron ring. The angles of rotation of all dipole magnets are given at the bottom of the diagram, and in Tables 10 and 11. The lengths and angles of only modified dipoles are given.

centers of the same sextupole lenses $T_{11} = T_{22} = T_{33} = T_{44} = -1$. Also in this matrix the elements $T_{12} = T_{34} = 0$ equal to zero. Such optics ideally provide complete suppression of geometric aberrations for particles with equilibrium energy. This scheme of compensation for the local chromaticity

		Original parameters of dipoles		New parameters	
Name	Quantity	Length, m	Angle, rad	Length, m	Angle, rad
B2E.4	1	5.90220	0.0557427	5.90220	0.0745895
BLA4LE	2	5.90220	0.0663658	5.90220	0.0520765
BLA2LE	1	5.90220	0.0206421	3.96143	-0.0181419
BLX2LE	2	3.96143	0.0259281	5.90220	0.0570931
BLB1LE	1	3.96143	-0.0229996	3.96143	-0.0368136

Table 10: Lengths and rotation angles of the dipoles to the left of the intersection of the beams.

		Original parameters of dipoles		New parameters	
Name	Quantity	Length, m	Angle, rad	Length, m	Angle, rad
BLA6RE	2	5.90220	0.0501497	5.90220	0.0501498
BLA4RE	1	5.90220	0.0480687	3.96143	0.0280687
BLA2RE	1	3.96143	0.0348280	5.90220	0.0591537
BLX1RE	2	3.96143	-0.0221788	3.96143	-0.0310501
BLB2RE	1	3.96143	0.0234696	5.90220	0.0548871
BLY2RE	2	3.96143	0.0270000	3.96143	0.0180000

Table 11: Lengths and rotation angles of the dipoles to the right of the intersection of the beams.

of strong lenses of the final focus by pairs of non-interleaved sextupoles is currently generally accepted and we have kept this approach intact, changing only the dipole angles in both chromatic blocks.

9.1.2 Spin rotators

There are several options for compensating for the coupling of betatron oscillations introduced by the longitudinal magnetic field of the solenoids. The general idea is that in a system of reference, which rotates with a half Larmor frequency around the longitudinal axis, motion in two transverse degrees of freedom becomes uncoupled if the angles of rotation of all skew-quadrupole lenses around their axis are chosen to be equal to the integral of such twist[61]:

$$\phi(s) = \int_{s_0}^s \kappa(s) ds$$

Here, the reference longitudinal coordinate s_0 is chosen in such a way that exactly half of the integral of the longitudinal field over the entire rotator is accumulated from the beginning of the rotator to this point. As a result, the angles of rotation of lenses at azimuths $s > s_0$ have a sign determined by the sign of the torsion $\kappa(s)$, while lenses at azimuths $s < s_0$ are rotated around their axis in the opposite direction.

In the thus introduced rotating Cartesian coordinate system (x,y,s), the equations of motion for transverse deflections x,y take on an extremely simple form:

$$\begin{aligned} x'' + (\kappa(s)^2 + g(s))x &= 0 \\ y'' + (\kappa(s)^2 + g(s))y &= 0 \end{aligned}$$

where $g(s) = G(s)/BR$ is the transverse field gradient normalized to the magnetic rigidity. It is shown in reference [61] that the full 4x4 transport matrix of a spin rotator has zero anti-diagonal 2x2 blocks if the matrices for x,y oscillations counted in the rotating coordinate system are equal

to each other with the opposite sign: $T_x = -T_y = T$. Under this condition, the full matrix M of the rotator has the same form both in the rotating basis and in the fixed one:

$$M = \begin{pmatrix} T & 0 \\ 0 & -T \end{pmatrix}$$

Note that there is great freedom in choosing the form of 2x2 matrices $T_x = -T_y = T$. In our choice, we settled on a mirror-symmetric arrangement of lenses and two sections of solenoids, shown in Fig. 21. Rotator optics based on such a scheme was successfully implemented in the 1990s on the AmPS storage ring at NIKHEF, Amsterdam[62].

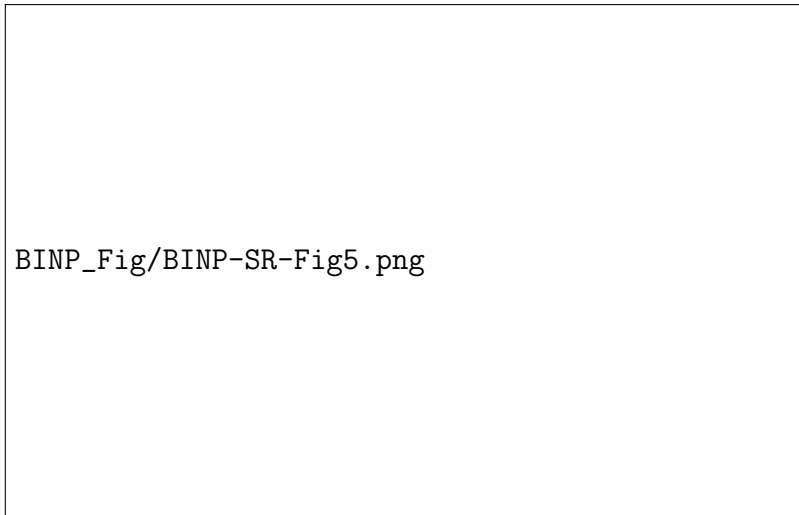


Figure 21: Optical functions of the spin rotator for the left half of the long interaction region.

The middle lens is not rotated around its axis, while the lenses of the two outermost doublets are rotated at an angle $\phi = \pm\pi/8(1 + a_e) = \pm 22.474^\circ$

The X -box 2x2 matrix is:

$$T = \begin{pmatrix} 0.4134 & 7.13 \\ -0.14025 & 0.4134 \end{pmatrix}$$

The total length of the rotator is 9.89112 meters. Table 12 shows the main parameters of the solenoids and lenses of this spin rotator.

Element	Length, m	Field or Gradient: T, T/m
Quadrupole #1, #5	0.46227	-29.4792 ($\phi_1 = -\phi_5 = -22.474^\circ$)
Drift 1	0.436	
Quadrupole #2, #4	0.46227	28.5569 ($\phi_2 = -\phi_4 = -22.474^\circ$)
Drift 2	0.25	
Solenoid	2.8	6.54197
Drift 3	0.25	
Quadrupole #3	0.57004	-25.3736 ($\phi_3 = 0$)

Table 12: Basic parameters of lenses and solenoids for $BR = 23.3495 \text{ T}\cdot\text{m}$ ($E = 7.15 \text{ GeV}$).

Alternatively, we consider the option of combining the solenoidal and quadrupole fields. This approach, but with a more radical proposal, to combine three types of fields (solenoidal, quadrupole, and dipole) is also considered and described in the following section. But, as mentioned above, the

presence of a dipole field can lead to the excitation of too large a vertical emittance and we consider here the solenoidal-quadrupole combined version. Table 13 shows the parameters of quadrupole lenses of such a solenoidal-quadrupole combined version, in which the solenoidal field is continuous and occupies the entire length of the rotator of 9.2 m.

The windings of the quadrupole lenses are superimposed on a cylindrical mandrel over the solenoid winding. Moreover, there are two sets of windings: straight-oriented windings and weaker second windings rotated at an angle of 45° to them, creating a skew-quadrupole field. The total number of lenses in the rotator is increased to 7 in order to have the freedom to reproduce the same optics in the versions with the longitudinal field on and off.

Element	Length, m	Field or Gradient: T, T/m
Drift #1, #17	0.34556	$B_s = G = 0$
Pure Solenoid #2, #16	0.15	$B_s = 4.067373$
Quadrupole plus Solenoid: #3, #15	0.7	-20.067768 ($\phi_3 = -\phi_{15} = -19.822^\circ$)
Solenoid #4, #14	0.4	$B_s = 4.067373$
Quadrupole plus Solenoid: #5, #13	0.7	23.232294 ($\phi_5 = -\phi_{13} = -14.5297^\circ$)
Solenoid #6, #12	0.8	$B_s = 4.067373$
Quadrupole plus Solenoid: #7, #11	0.7	-5.385630 ($\phi_7 = -\phi_{11} = -7.3598^\circ$)
Solenoid #8, #10	0.8	
Quadrupole plus Solenoid: #9	0.7	-22.806964 ($\phi_9 = 0^\circ$)

Table 13: Basic parameters of lenses and solenoids of a spin rotator with a superposition of solenoidal and quadrupole fields for $BR = 23.3495 \text{ T}\cdot\text{m}$ ($E = 7.15 \text{ GeV}$). The sequence of numbering of structure elements: 1, 2, ..., 17.

The option with combined fields has several attractive points. Its main advantage over the variant with separated functions is the acceptably small value of the longitudinal field: $B_s = 4.067373 \text{ T}$ versus the alternative $B_s = 6.54197 \text{ T}$. Also, the use of a common cylindrical frame supporting both the solenoidal and quadrupole windings may be more technologically advanced as compared to their separate fixation in space. In addition, the need to create two types of lens windings - straight-oriented and skew-rotated - makes the cosine-theta technology the preferred choice.

When calculating the transport matrix of a section of the structure with superposition of the quadrupole and solenoidal fields constant along s , we used numerical methods for calculating the exponent of the matrix of a linear system of equations of motion:

$$\frac{dX}{ds} = A \cdot X \quad A = \begin{pmatrix} 0 & 1 & \kappa & 0 \\ -\kappa^2 - g & 0 & 0 & \kappa \\ -\kappa & 0 & 0 & 1 \\ 0 & -\kappa & -\kappa^2 + g & 0 \end{pmatrix}$$

The transformation transport matrix of vector $X = (x, p_x, y, p_y)^T$ is:

$$T(s, g, \kappa) = R(-s\kappa)\exp(sA)R(s\kappa)$$

where $R(s\kappa)$ is the rotation matrix, and the arguments of the matrix A are as defined above. Note that p_x and p_y are canonical momenta, defined as:

$$\begin{aligned} p_x &= x' - \kappa y \\ p_y &= y' + \kappa x \end{aligned}$$

Canonical momenta do not experience any jumps at the boundaries of the solenoidal field, in contrast to kinetic impulses x', y' which subjected a discontinuity at solenoid edges.

The angles of rotation of the lenses were selected in such a way as to make all elements of antidiagonal 2x2 coupling boxes of the complete transport matrix of the rotator vanish. To fulfill this condition, taking into account the mirror symmetry of the placement of all seven lenses and with the antisymmetric rotation of six of them around the axis, we used a procedure for numerical optimization of three rotation angles and gradients of four lens families (the central lens is not rotated!). The X-block matrix was selected the same as in the rotator version with separated longitudinal and transverse fields:

$$T = \begin{pmatrix} 0.4134 & 7.24 \\ -0.14025 & 0.4134 \end{pmatrix}$$

The matrix of the Y-block is equal to it with the opposite sign.

At the edges of the rotator, short drift gaps with a length of 0.34556 m are left free from fields, connecting the cold superconducting magnetic system with room temperature of the adjacent areas. The total length of the entire rotator is 9.89112 m, same as in the first version.

9.1.3 Beam depolarization time

When a photon of synchrotron radiation is emitted, there is an abrupt change in the equilibrium direction of the spin and the magnitude of the projection of the spin on the new equilibrium direction. The spin relaxation time of the beam due to this process and the equilibrium degree of polarization are determined by the well-known Derbenev-Kondratenko formulas [63]:

$$\begin{aligned} \tau_{rad}^{-1} &= \frac{5\sqrt{3}}{8} \lambda_e r_e c \gamma^5 \left\langle |r|^{-3} \left(1 - \frac{2}{9} (\vec{n}\vec{v})^2 + \frac{11}{18} (\vec{d})^2 \right) \right\rangle \\ \xi_{rad} &= -\frac{8}{5\sqrt{3}} \left\langle |r|^{-3} \vec{b}(\vec{n} - \vec{d}) \right\rangle / \left\langle |r|^{-3} \left(1 - \frac{2}{9} (\vec{n}\vec{v})^2 + \frac{11}{18} (\vec{d})^2 \right) \right\rangle \end{aligned}$$

where λ_e , r_e , c and γ are the Compton wavelength of an electron, its classical radius, speed of light and gamma factor, respectively. Other parameters stands for: r – radius of curvature of the orbit at the point of emission of the photon, \vec{b} is the unit vector indicating the direction of the magnetic field, \vec{n} the unit vector along the equilibrium spin direction at a given azimuth, and $\vec{d} = \gamma(d\vec{n}/d\gamma)$ the spin-orbit coupling vector, showing the direction of the jump of vector \vec{n} when a photon is emitted, and the magnitude of this jump.

Modulus distribution of vector \vec{d} over the azimuth of the storage ring was calculated by the ASPIRRIN program, created in the 1990s[64, 65]. Figure 22 shows the graph of $|\vec{d}(s)|$ calculated for the rotator optics option with the parameters in Table 12.

It is essential that for a given optimized value of the beam energy $E = 7.15$ GeV the modulus $|\vec{d}(s)|$ almost everywhere does not exceed the factor 2. Thereby the spin relaxation time falls from the initial values of the Sokolov-Ternov polarization time $\tau_{ST} = 32000$ s to a quite acceptable $\tau_{rad} = 10000$ s. This time remains very long in comparison with the time for refreshing the beam with new polarized electrons, which is less than $\tau_{beam} < 1000$ s. The energy dependence of the radiation spin relaxation time is shown in Fig. 23. Resonances with integer values of the spin frequency occurred at the energy $E = 6.61, 7.05, 7.49$ GeV, and the so-called “intrinsic” spin resonances with the betatron vibration frequencies are located at the spin tunes $\{\nu_0\}=0.4$ and 0.6. You have to choose the beam energy and operate somewhere in between these two types of resonances, for example at $E=7.15$ GeV, or in other words at spin tune $\nu_0 = 16.226$.

In principle, resonances with betatron frequencies can be made narrower. For this, it is necessary to fulfill the condition of the spin transparency of both: the rotator itself and the entire experimental



Figure 22: Graph of the modulus of the spin-orbit coupling vector in the HER ring with a modified rotation geometry in the experimental section. Rotator parameters from Table 12 and Fig. 21.



Figure 23: Dependence of the radiation spin relaxation time on energy with the rotator version from Table 12 with rotated extreme doublets of the lenses, see Fig. 21.

straight section as a whole - from the rotator to the rotator [66]. But, as our study has shown, the fulfillment of the conditions for spin transparency requires several times stronger lenses in comparison with the variants of rotator optics considered above. Therefore, we have come to a compromise variant of using relatively weak lenses providing, nevertheless, a sufficiently long spin relaxation time. Note that electrons with the opposite sign of polarization with respect to the equilibrium one dictated by the Sokolov-Ternov self-polarization mechanism will depolarize much faster, tending exponentially to their natural state with a positive degree of polarization shown by the blue curve in Fig. 23. Apparently, bunches of electrons with a negative sign of polarization need to be updated more often so that their degree of polarization averaged over time is as high as for its positive sign.

Unfortunately, all programs of accelerator optics calculations available to us, such as MADx

or RING, as well as the program for calculating the spin response functions ASPIRRIN, do not support the calculation of matrices of optical elements with combined longitudinal and quadrupole fields. Therefore, to calculate the time and degree of self-polarization in the variant of optics with combined longitudinal and quadrupole fields, we replaced the structure of rotators with a continuous longitudinal field (Table 13) with a structure similar to it presented in Table 14. In this structure, longitudinal field discontinuities are made, in which somewhat shortened lenses are located at the same distances from each other between their centers, as in the variant of Table 13, see Fig. 24. The presence of four families of quadrupole lenses and complete freedom in choosing the angles of their rotation around the axis make it possible to obtain any betatron phase advances and periodic beta functions of the rotator, both with the longitudinal field turned on and off. We reproduced the X-box matrix the same as the rotator shown in Fig. 21.

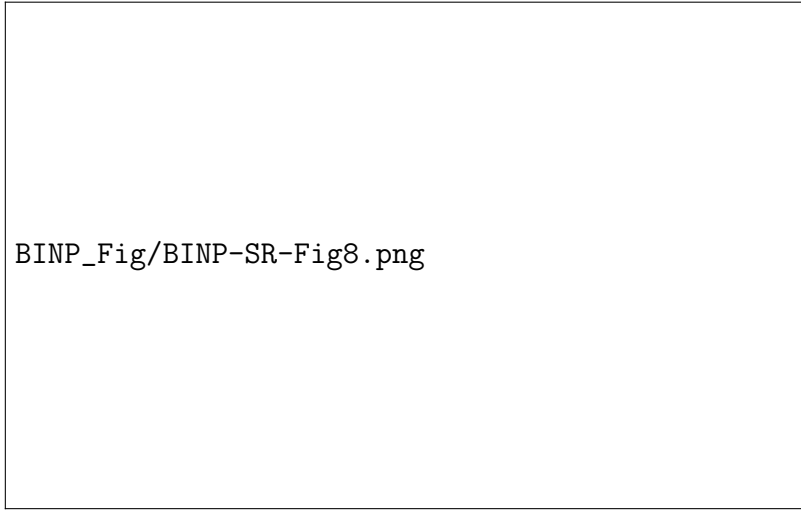


Figure 24: Amplitude functions in a rotator with alternating sections of solenoids and quadrupole lenses rotated around the axis.

Element	Length, m	Field or Gradient: T, T/m
Drift #1, #17	0.34556	$B_s = G = 0$
Solenoid: #2, #16	0.35	$B_s = 5.15983$
Quadrupole: #3, #15	0.3	$-41.5055 (\phi_3 = -\phi_{15} = -20.25818^\circ)$
Solenoid #4, #14	0.8	$B_s = 5.15983$
Quadrupole: #5, #13	0.3	$45.5005 (\phi_5 = -\phi_{13} = -15.19364^\circ)$
Solenoid #6, #12	1.2	$B_s = 5.15983$
Quadrupole: #7, #11	0.3	$-7.56501 (\phi_7 = -\phi_{11} = 7.59682^\circ)$
Solenoid #8, #10	1.2	5.15983
Quadrupole: #9	0.3	$-53.2734 (\phi_9 = 0^\circ)$

Table 14: Parameters of lenses and solenoids of a spin rotator with alternating solenoidal and quadrupole fields for $BR = 23.3495 \text{ T}\cdot\text{m}$ ($E = 7.15 \text{ GeV}$).

The magnitude of the modulus of the spin-orbit coupling vector calculated by the ASPIRRIN program is shown in Fig. 25. Its average value in the main part of the ring is less than one and it can be seen that this version of the rotator optics is the best of all those presented earlier. This was reflected in a significant increase in the spin relaxation time: $\tau_{rad}=18800 \text{ s}$ versus 10000 s for the rotator version from Table 12. Both these tau-values are given for beam energy $E = 7.15 \text{ GeV}$.

The degree of equilibrium polarization also increased from $P = 40\%$ to $P = 60\%$. The graphs of the dependence of the relaxation time and the equilibrium degree of polarization on energy are shown in Fig. 26. We believe that the above estimates of radiative self-polarization refer not only to the version from Table 14, but also to the version of the parameters taken from Table 13 with a continuous longitudinal field.

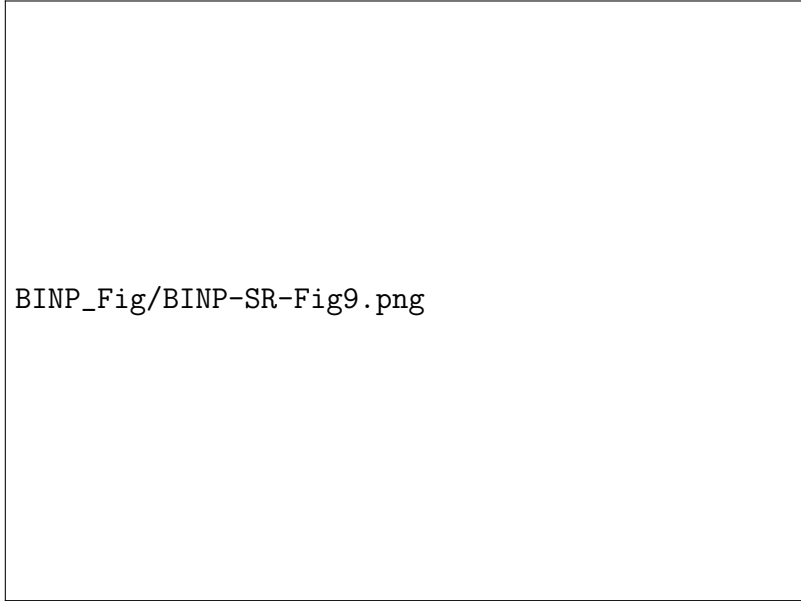


Figure 25: Modulus of the spin-orbit coupling vector in the HER ring with the rotator parameters from Table 14.

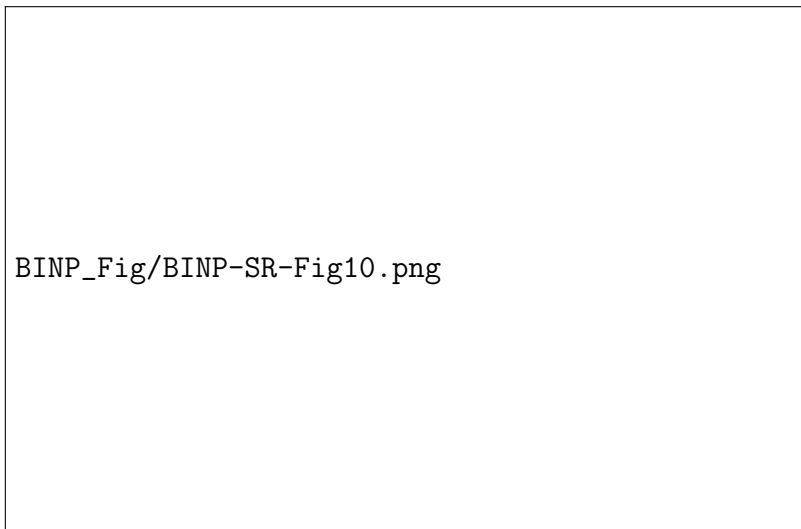


Figure 26: Radiation spin relaxation time and equilibrium degree of polarization versus energy for the rotator optics option from Table 14.

Finally, Figures 27-28 show the optical functions of the left and right halves of the long experimental straight section. They show spin rotators with an optical structure from Table 12. Outside the rotators, the beta functions and the dispersion function are the same for all the versions considered above, since the transport matrices of all these versions are made the same.

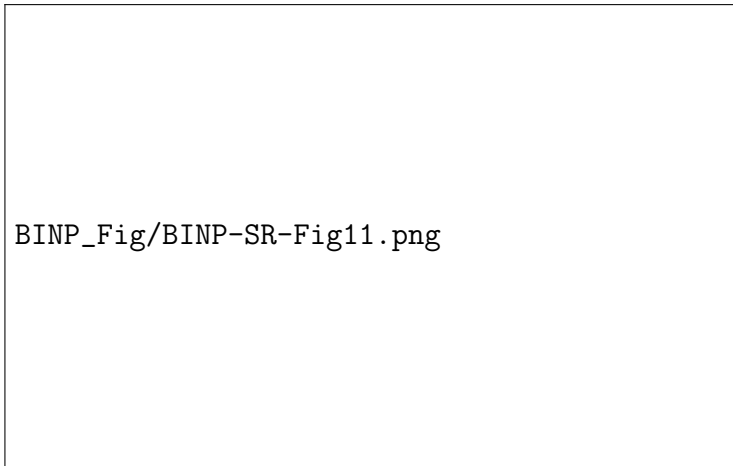


Figure 27: Optical functions of the left half of the long experimental section.

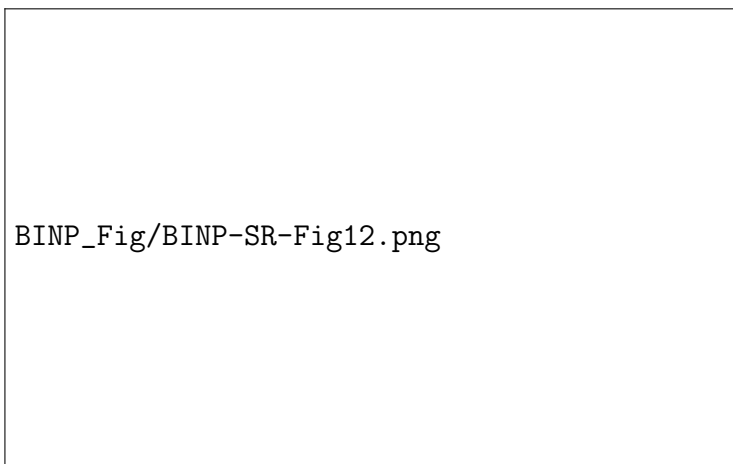


Figure 28: Optical functions of the right half of the long experimental section.

9.1.4 Conclusions

We found, in our opinion, an acceptable variant of converting the geometry of electron beam bends in the experimental section of the HER storage ring, which provides drift gaps with a length of about 10 meters for installing spin rotators in them. Two rotators serve to rotate electron spins by 90° from vertical to horizontal and then, after passing the crossing point, back to vertical. Various lattice options for spin rotators are considered. In the variant with separate longitudinal and quadrupole transverse fields, the optimal transport matrix of the rotator was found, which made it possible to minimize the disturbances in the optics of the storage ring by the changes introduced. The disadvantage of this option is the relatively large value of the longitudinal magnetic field: over 6.54 T. This disadvantage is eliminated in the variant with the superposition of the rotated quadrupole fields on the continuous longitudinal field of the solenoid, which now occupies the entire length of the gap allocated for the rotator. The value of the longitudinal field in this variant dropped to 4.067 T. Calculations of the relaxation time of polarization from the initial $+90\%$ or -90% to its equilibrium value near $+60\%$ showed its sufficiently large value, about 19000 sec, which will make it possible to have a very high level of average polarization during the lifetime of the beam with continuous feeding with new polarized electrons from injector. The urgent task at the next stage is to check the boundaries of the dynamic aperture by tracking the particles in order to get an answer to the question of whether it has worsened in comparison with the initial version of the ring optics.

9.2 Dipole-Solenoid-Quadrupoles Combined Function Magnets Concept

This section describes the conceptual design of the spin rotator with combined function magnets proposed by Uli Wienands (Argonne National Laboratory). The basic idea is to replace a small number of existing HER dipoles on either side of the interaction point (IP) with the rotator magnets in a manner that renders the change transparent to the rest of the lattice and HER operation. This design is intended to introduce the spin rotators with minimal changes to the HER. In this design, the spin rotator magnet consists of dipole-solenoid combined function magnets with six solenoid-quadrupole magnets installed on the top to compensate for the x-y plane coupling caused by the solenoid [67], as shown in Figure 29. The strength of the dipole is maintained as the original to preserve the machine geometry. Also, this design allows the original machine to be recovered by minimizing any disruption to the existing ring, such as by turning off the solenoid-quadrupole field in the rotator magnet. As Figure 30 shows, the spin rotator has two components: the left rotator (L-Rot) located at ~ 210 m upstream of the IP, the right rotator (R-Rot) located at ~ 169 m downstream of the IP. The L-Rot is to rotate the vertical spin of the incoming beam to some direction in the horizontal plane, and dipoles located between L-Rot and the IP continue to rotate spin until it reaches the longitudinal direction. Then, the R-Rot rotates the horizontal spin back to the vertical. The choice of the rotator's installation position has to consider the following constraints: 1) minimizing the impact on the machine dynamics caused by installing the spin rotator; 2) the rotator magnet strength not exceeding the technical limit. The installation position must avoid the region ± 100 m near the IP and keep the area between L-Rot and R-Rot as narrow as possible because the vertical polarization is most stable in the ring due to the vertically induced dipole field. Also, it is beneficial to minimize the number of dipoles that will be replaced. The technical limit is imposed based on considering the possible technology applied to manufacture the combined functions magnets, such as the direct wind technology [68]; the technical limit is 5 T for the solenoid and 30 T/m for the skew-quadrupole. Considering all the constraints listed above, the four B2E dipoles (field: 0.22075 T, length: 5.9 m) in Figure 30 are determined to be the optimal positions to install and the detail is given in the Reference [69].

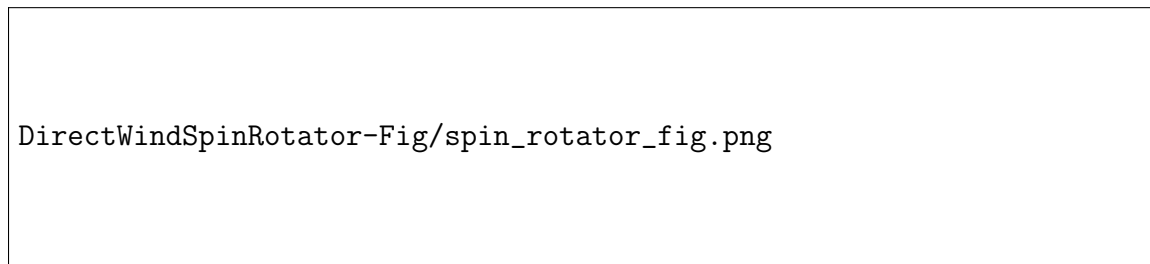


Figure 29: Uli Wienands' (ANL) concept for a compact combined function spin rotator unit with overlaid dipole, solenoid and skew-quadrupole superconducting coil fields.

The installation of the rotator is for the e^- polarization purpose only; the original machine dynamics must be preserved as much as possible, which is called “transparency”. Procedures performed to achieve transparency include the decoupling, optical rematching, and restoring of ring parameters. The x-y plane is decoupled at the exit of the rotator by fitting the skew-quads. The optical functions, such as the beta, alpha, and dispersion, need to be matched to the original at the exit of the rotator region by tuning nearby existing quadrupoles to restore the beam dynamics. Also, the overall ring parameters such as the Tunes and the chromaticities need to be the same as in the original lattice to make the rotator fully transparent to the ring.

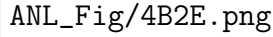
A rectangular box containing the text 'ANL_Fig/4B2E.png'.

Figure 30: Overview of the spin rotator structure: the four B2E dipoles indicated would be replaced by the combine function spin rotator magnets.

9.2.1 Rotator Modelling with BMAD

The lattice simulation tool applied to run optimizations for this project is BMAD [70], an open-source, subroutine library created/maintained by David Sagan at Cornell University. The BMAD lattice file of the current SuperKEKB High Energy Ring (HER) with crab waist and a $\beta_y^* = 1$ mm was translated from SAD [71]. Note that the positive y-direction of the HER lattice points downward in the KEK frame and the e^+ default simulation particle is used. The rotator magnet modelling requires a combination of the dipole-solenoid-quadrupole element. BMAD has the solenoid-quadrupole element (Sol_Quad), but it does not have the attribute of a dipole because Sol_Quad is a straight element, and a dipole (Sbend) is a curved element. Following the advice of David Sagan, we use the ‘hkick’ (horizontal kick) feature to simulate the dipole. The Sol_Quad has an hkick attribute since it is a straight element. To simulate the curved element (dipole) with the straight element(hkick), the hkick is initially sliced into six pieces (stand-alone model) to match the number of skew-quad, and the geometry of the dipole is recovered by applying patch elements to shift the reference orbit at the exit of each piece, as shown in Figure 31.

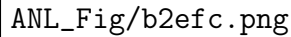
A rectangular box containing the text 'ANL_Fig/b2efc.png'.

Figure 31: Comparison of the geometry of B2E and 6-piece sliced hkick with patches to shift the reference orbit.

Also, the strength of the hkick pieces is adjusted to match the horizontal orbit. To validate the dipole simulation with the hkick, the four B2E dipoles mentioned in the previous section are replaced with the hkicks in the ring and we compare the optical functions, spin, and ring parameters such as the Tunes and chromaticities. The validation result is shown in the Reference [69]. However, using hkick and patches causes non-physical orbit excursion due to the shift of the reference orbit. It might affect the performance of the rotator since the particle would experience the solenoid-quad field if it is not following the ideal orbit. This problem is addressed by applying the “slice model”, which is to further slice each piece of the hkick into smaller pieces. With this method, the non-physical orbit excursion is significantly reduced but makes the optimization more computationally expensive. The optimal slicing number of the “slice model” is determined to be 16, 96 slices in total. Also, the ‘vkick’ (vertical kick) is introduced to match the vertical orbit since solenoids cause the x-y plane coupling.

9.2.2 Open-geometry Optimization

Four B2E dipoles, indicated in Figure 30, are replaced with the rotator elements, and the lattice segments which contain the L-Rot/R-Rot are taken out from the full lattice. The open-geometry optimizations are performed to the lattice segments. The first goal is to fit the value of the solenoid fields to achieve the polarization purpose. The strengths of the two solenoids of the L-Rot are determined to be $k_s = -0.20720 \text{ m}^{-1}$, -0.11027 m^{-1} , or $B_s = -4.8431 \text{ T}$, -2.5774 T . For the R-Rot, solenoids are determined to be $k_s = -0.15438 \text{ m}^{-1}$, -0.16865 m^{-1} , or $B_s = -3.6084 \text{ T}$, -3.9420 T . All solenoids are below the technical limit of 5 T. In the next step, the skew-quads are turned on to perform the decoupling, with the goal of making every element in the \mathbf{C} matrix [72] zero at the exit of each rotator magnet. The skew-quad strength is correlated to the solenoid. The strongest skew-quad in the L-Rot is about 20 T/m and approximately 14 T/m for the R-Rot; all solenoids are below the limit of 30 T/m. The final step of the open-geometry optimization is to recover the original optical functions to achieve transparency. The lattice segments containing the rotators are extended to involve nearby quadrupoles. Existing quadrupoles and skew-quads are adjusted to match the optical functions to the original at exit of the lattice segments. However, it is challenging to match the vertical dispersion because it lacks the horizontal bending effect in the ring. The way to address this problem is to abandon the decoupling at the exit of the first rotator magnet in the L-Rot/R-Rot, giving extra freedom. In addition, the vertical emittance must be kept low to guarantee the high luminosity. The finalized optimization result is shown in Table 20, Table 21 for the L-Rot, and Table 22, Table 23 for the R-Rot. The maximum strength of new quadrupoles is about 14 T/m, which is achievable. The lattice segments are put back into the ring, with Figure 32 and Figure 33 showing the comparison of the L-Rot/R-Rot tuning region with the original. It can be seen that the optical functions are well matched to the original at the exit of the tuning region. Note that the orbit excursions in the L-Rot/R-Rot regions are non-physical; they are artificial effects associated with the use of a series of hkicks to model the dipole component of the spin rotator.



Figure 32: Comparison of the L-Rot tuning region: optical functions are matched to the original at the exit. Note that the orbit excursions in the bottom right plot in the region of the L-Rot are non-physical artifacts of the slice model used to describe the dipole component of the spin rotator, as discussed in the text.



Figure 33: Comparison of the R-Rot tuning region: optical functions are matched to the original at the exit. Note that the orbit excursions in the bottom right plot in the region of the R-Rot are non-physical artifacts of the slice model used to describe the dipole component of the spin rotator, as discussed in the text.

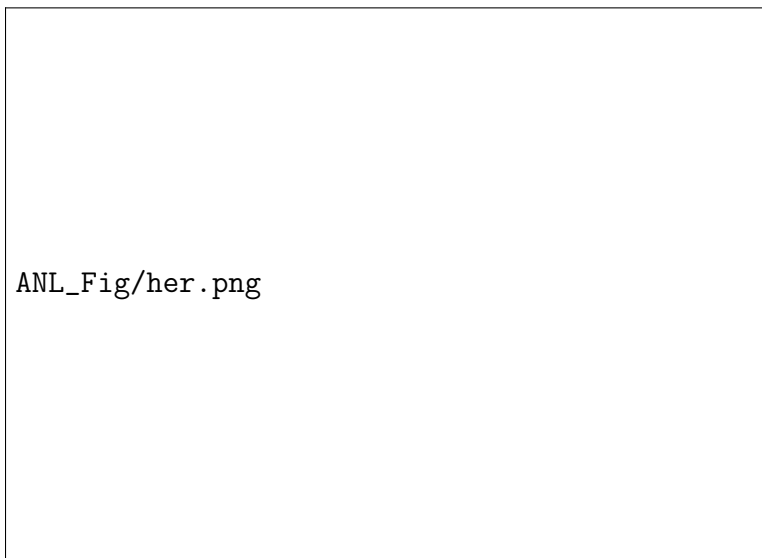


Figure 34: Quadrupoles in the “Nikko” section of the HER are adjusted to match the Tunes; sextupoles in four arc sections between $s = 167$ to 630 m, $s = 880$ to 1385 m, $s = 1635$ to 2140 m, and $s = 2338$ to 2775 m are adjusted to match the chromaticities

9.2.3 Closed-geometry Optimization

The optical functions are matched to the original lattice outside the rotator regions but are not restored inside those regions, which causes Tunes and chromaticities to be shifted from the original lattice. To make the spin rotator fully transparent to the ring, they must be re-matched. The match of the Tunes is achieved by adjusting existing quadrupoles in the straight section region having zero dispersion, allowing local quadrupoles to be adjusted without changing the dispersion. The straight area satisfying the zero-dispersion requirement is the “Nikko” section shown in Figure 34 [73], and the original chromaticities are restored by tuning sextupoles in four arc sections. The adjustment of the sextupoles does not change the beta function. Thus, Tunes must be matched

before chromaticities. Also, Tunes and chromaticities are overall ring parameters that can only be calculated in closed-geometry.

9.2.4 Match the Tune

In the “Nikko” section, the beta function has a symmetric structure because of the symmetric distribution of the quadrupole pairs. The optimization goal is to recover the original Tunes Q_x , Q_y and match the Twiss parameters $(\beta_x, \beta_y, \alpha_x, \alpha_y)$ at the exit of the “Nikko” section. In order to preserve the symmetric structure, quadrupoles with the same name must be kept identical. There are 8 variables available, and 6 parameters to match, which gives 2 degrees of freedom. To address the problem of simultaneously matching the Tune and the optical functions, we start with the following approximation. For a small quadrupole deviation Δk , the Tune shift is given by [74]:

$$dQ = \frac{1}{4\pi} \Delta k \beta ds, \quad (15)$$

where β is the local beta function. Notice that the local beta function remains changed. Similarly, when adjust a series of quadrupoles slightly, the total Tune shift ΔQ can be approximated by:

$$\Delta Q \sim \frac{1}{4\pi} \sum_i \beta_i \Delta k_i L_i, \quad (16)$$

where L_i is the length of the quadrupole. This equation indicates that the Tune can be slightly shifted without significantly changing the local beta function if the variation of quadrupoles is sufficiently small. Thus, the “Ladder method” is created to approach the original Tunes by taking small steps. This method allows the fitter to match the Tune and the beta function simultaneously since the variation of the quadrupole is small. As Table 15 shows, it takes 15 steps to approach the original Tunes. At each step, the Tunes and the beta function at the exit of the “Nikko” section are matched to the original with an extra constraint to add an upper limit to the local beta function. With this method, the original Tunes are successfully restored. Also, the symmetric structure of the beta function in the “Nikko” section is maintained, and the local beta function stays in a reasonable range, as shown in Figure 35. Table 16 shows the optimization result and there is no significant adjustment.

Step	0th	1st	2nd	3rd	...	15th
Q_x	45.777566	45.761128	45.744690	45.728252	...	45.530994
Q_y	44.446774	44.389036	44.331299	44.273561	...	43.580709

Table 15: Ladder Method: taking steps to approach the original Tunes



Figure 35: Comparison of the “Nikko” section after the Tune match

Quadrupole	Length (m)	k_1 (m^{-2}) original	k_1 (m^{-2}) Rot
QFRNE	1.080	0.122	0.099
QDRNE	1.080	-0.118	-0.085
QR7NE	0.826	-0.252	-0.249
QR6NE	1.015	0.196	0.202
QR5NE	1.080	-0.110	-0.091
QR4NE	1.080	0.144	0.127
QR3NE	1.080	-0.145	-0.071
QR2NE	1.080	0.110	0.067

Table 16: Quadrupoles adjusted to match the Tunes for the rotator ring. The quadrupole magnet labels are those used in the SAD lattice file.

9.2.5 Match the Chromaticity

Matching the original first-order chromaticity is achieved by adjusting sextupole strengths of existing HER sextupoles in a manner that introduces the required additional quadrupole strength from the quadrupole field component of those sextupoles. The total effective chromaticity ξ is given by [74]:

$$\xi_{tot} = \frac{1}{4\pi} \oint \left[k(s) + m(s)\eta(s) \right] \beta(s) ds, \quad (17)$$

where m is sextupole strength, η is the dispersion, and k is the quadrupole strength. Based on

this equation, it can be seen that there exists a linear relation between the chromaticity and the sextupole strength since varying the sextupole strength does not change the beta function. The variation of chromaticity can be expressed as a linear combination of the variation of sextupole strength:

$$\begin{cases} \Delta\xi_x = \sum_i p_i \Delta x_i \\ \Delta\xi_y = \sum_j q_j \Delta x_j \end{cases} \quad (18)$$

with

$$\begin{cases} p_i = \frac{1}{4\pi} \beta_{x,i} \eta_{x,i} \\ q_j = -\frac{1}{4\pi} \beta_{y,j} \eta_{x,j} \end{cases}, \quad (19)$$

where $\Delta\xi_x$, $\Delta\xi_y$ is the variation that needs to be achieved in order to match the original horizontal and vertical chromaticity, respectively; Δx is the variation of integrated strength of the sextupole; η_x , η_y is the horizontal and the vertical component of the dispersion, respectively. Notice that $b_2 = \frac{k_2 L}{2}$ represents the integrated strength of sextupole in the HER lattice. With this relation, an algorithm is developed to achieve a better starting point for running the BMAD optimization. Assume N ($N > 2$) sextupoles are used to match the the chromaticity. Let $\vec{P} = (p_1, p_2, \dots, p_N)$, $\vec{Q} = (q_1, q_2, \dots, q_N)$, $\vec{x} = (\Delta x_1, \Delta x_2, \dots, \Delta x_N)$, and define following functions:

$$\begin{cases} f_p(\vec{x}) = \vec{P} \cdot \vec{x} - \Delta\xi_x \\ f_q(\vec{x}) = \vec{Q} \cdot \vec{x} - \Delta\xi_y \end{cases}, \quad (20)$$

Construct following square function:

$$f(\vec{x}) = f_p^2(\vec{x}) + f_q^2(\vec{x}) + \lambda \vec{x}^2. \quad (21)$$

The first two terms represent discrepancies to the original chromaticities. The last term prevents variables from having large values, and the choice of λ must not have significant impact on discrepancies. When $f(\vec{x})$ reaches the global minimum (or close to it), the desired chromaticities are reached. A gradient descent algorithm is applied to approach the global minimum. We give random starting point to initiate the algorithm and at the j th iteration, compute following functions:

$$f_p^j = \vec{P} \cdot \vec{x}^j - \Delta\xi_x, \quad (22)$$

$$f_q^j = \vec{Q} \cdot \vec{x}^j - \Delta\xi_y, \quad (23)$$

$$\nabla f^j = 2f_p^j \vec{P} + 2f_q^j \vec{Q} + 2\lambda \vec{x}^j, \quad (24)$$

and determine variables for the next iteration:

$$\vec{x}^{j+1} = \vec{x}^j - \varepsilon \nabla f^j, \quad (25)$$

where ε is the learning rate. The choice of ε has vital impact on the performance of the algorithm, since large values may not converge to the optima, and small values require longer iteration process.

Sextupoles located at the rotator area and their identical pair are not used for matching the chromaticity. The phase advance between each sextupole pair needs to be fixed at π to cancel out the leading order of their non-linear effect. However, the adjustment of the quadrupoles near the rotator region changes the local beta function thus changing the local phase, as shown in Table 17. Sextupole pairs SF4TLE, SD5TLE, and SD3TRE are turned off due to the large phase shift from π . SF4TRE pair is not adjusted since the phase advance is slightly shifted from π .

sextupole	s-position (m)	Ψ_x	Ψ_y	$\Delta\Psi_x$	$\Delta\Psi_y$
SF4TLE	199.675	22.604	24.978		
SF4TLE	235.237	29.183	30.468	6.579	5.490
SD5TLE	241.458	29.552	30.790		
SD5TLE	269.820	31.817	33.344	2.265	2.554
SF4TRE	2779.934	263.620	262.070		
SF4TRE	2815.495	266.770	265.220	3.150	2.950
SD3TRE	2821.717	265.560	248.930		
SD3TRE	2850.078	268.330	256.290	2.770	7.360

Table 17: Sextupoles located at the rotator tuning area. Ψ_x , Ψ_y are the horizontal and vertical component of the phase, and $\Delta\Psi_x$, $\Delta\Psi_y$ are the horizontal and vertical component of advance between the sextupole pair.

The gradient descent algorithm is implemented in Python. 45 pairs of sextupoles in 4 arc sections are adjusted. It was found that there is no significant adjustment required to match the chromaticities, thus taking $\lambda = 0$. The square function $f(\vec{x})$ drops exponentially and reaches the global minimum at ~ 630 th iteration. All the adjusted sextupoles stay below the technical limit, and their sign does not change. The output from Python is used as the starting point to run BMAD optimization, and the optimization result is shown in Table 24.

9.2.6 HER With Spin Rotators: Rotator Ring

With the rematching completed, we now turn to examining the full HER with the spin rotators - the ‘Rotator Ring’. Figure 36 shows the comparison of the entire lattice of the HER, and the optical functions are well preserved outside the rotator region. For example, the β_y^* values for both the original and rotator ring are the same, 1 mm. The only noticeable change of the ring parameters in Figure 18 is the vertical emittance, which is higher than the original but still smaller than the current design 12.9 pm [75]. These comparisons indicate that transparency is successfully achieved; the impact of installing the spin rotator is minimized to an acceptable level. The single-particle tracking result shows that the longitudinal polarization at the IP reaches a significantly high level, greater than 99.99%, as shown in Table 19, and vertical polarization is achieved at the entrance of the L-Rot and exit of the R-Rot, which satisfies the polarization purpose. Figure 37 shows the spin motion of the electron in the KEK frame with the spin rotator installed in the HER. The IP polarization depends on the injection point as the injected beam is polarized aligned with the dipole

field, leading to right-handed longitudinal polarization at the IP and anti-aligned with the dipole field, leading to left-handed longitudinal polarization.

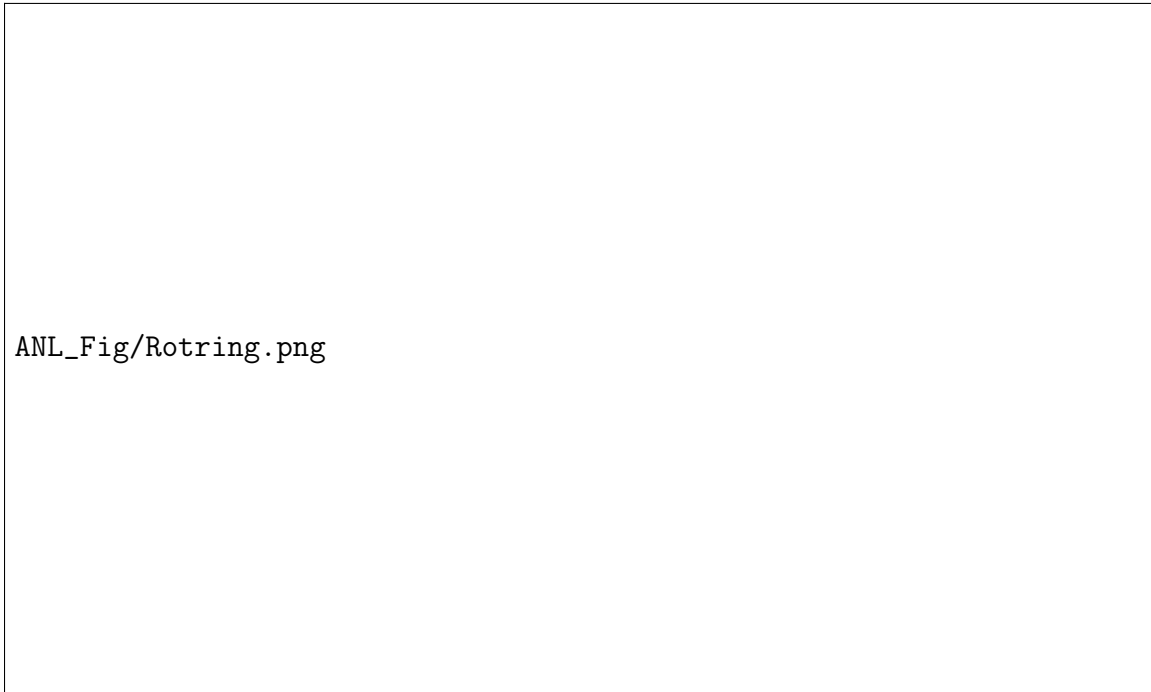


Figure 36: Comparison of the HER with Rotator installed: the squiggle in the orbit plot at $s \sim 2200$ m is the effect of wigglers

Machine Parameter	Original Ring	Rot Installed
Tune Q_x	45.530994	45.530994
Tune Q_y	43.580709	43.580709
Chromaticity ξ_x	1.593508	1.593508
Chromaticity ξ_y	1.622865	1.622865
Damping partition J_x	1.000064	0.984216
Damping partition J_y	1.000002	1.005266
Emittance ε_x (m)	4.44061×10^{-9}	4.89628×10^{-9}
Emittance ε_y (m)	5.65367×10^{-13}	3.96631×10^{-12}

Table 18: Comparison of the ring parameters after matching the Tunes and Chromaticities

Spin Component	Entrance of the L-Rot	IP	Exit of the R-Rot
X	-0.0000450734	0.0000066698	0.0000538792
Y	0.9999999959	0.0000926945	0.9999999959
Z	-0.0000788085	0.9999999957	-0.0000728110

Table 19: Single particle spin tracking result of the electron in the rotator ring

ANL_Fig/KEK.png

Figure 37: The spin motion of the electron (KEK frame) in the HER with the spin rotator installed

9.2.7 Tracking Studies and Next Steps

Having achieved a first-order BMAD spin rotator solution using this approach of replacing four existing dipoles with spin rotators, the next step is to consider the non-linear effects using long-term tracking studies. Two goals of these studies: 1)investigate the dynamic aperture and re-tune sextupoles to achieve the maximum dynamic aperture; 2)determine the beam lifetime and polarization lifetime. The beam tracking will be implemented by the Long Term Tracking [76] program built upon BMAD with the Polymorphic Tracking Code (PTC) interface. The R&D effort on this combined function spin rotator conceptual design has shown it to be promising and will be continue to be pursued with these long-term tracking studies, along with R&D on how to implement the magnet realization using direct wind technologies, such as those available at BNL.

Quads	L(m)	k_1L (Original)	k_1L (L-Rot)	B_1 (Original) T/m	B_1 (L-Rot) T/m
QD3E	0.826	-0.175	-0.177	-4.948	-5.012
QF4E	1.015	0.035	0.071	0.805	1.633
QEAE	0.826	0.183	0.175	5.178	4.961
QD5E	0.826	-0.179	-0.286	-5.074	-8.079
QF6E	0.557	0.163	0.342	6.855	14.366
QF2E	0.557	0.192	0.145	8.050	6.067
QD1E	1.015	-0.255	-0.203	-5.868	-4.682

Table 20: Ring quadrupoles used for matching the optics in the L-Rot tuning region. The quadrupole magnet labels are those used in the SAD lattice file.

Skew-Quad	L(m)	$k_1 L$	B_1 (T/m)	Tilt (rad)
B2EALSQ1	0.9837	0.511	12.133	-0.426
B2EALSQ2	0.9837	0.510	12.130	1.053
B2EALSQ3	0.9837	-0.314	-7.457	-0.988
B2EALSQ4	0.9837	0.855	20.315	0.030
B2EALSQ5	0.9837	0.688	16.350	-0.630
B2EALSQ6	0.9837	0.814	19.340	1.383
B2EBLSQ1	0.9837	0.558	13.266	0.651
B2EBLSQ2	0.9837	-0.482	-11.444	0.992
B2EBLSQ3	0.9837	0.426	10.119	-1.494
B2EBLSQ4	0.9837	0.338	8.024	-0.931
B2EBLSQ5	0.9837	0.562	13.359	0.735
B2EBLSQ6	0.9837	-0.185	-4.404	0.868

Table 21: Skew-quadrupoles in the L-Rot.

Quads	L(m)	$k_1 L$ (Original)	$k_1 L$ (R-Rot)	B_1 (Original) T/m	B_1 (R-Rot) T/m
QD5E	0.826	-0.179	-0.165	-5.074	-4.667
QEAE	0.826	0.183	0.154	5.178	4.362
QF4E	1.015	0.035	0.067	0.805	1.538
QD3E	0.826	-0.175	-0.251	-4.948	-7.088
QF2E	0.557	0.192	0.183	8.050	7.659
QD1E	1.015	-0.255	-0.274	-5.868	-6.311
QLA10RE	0.826	0.202	0.185	5.718	5.234
QLA9RE	0.826	-0.237	-0.226	-6.703	-6.385
QLA8RE	0.557	0.203	0.169	8.527	7.106
QLA7RE	0.826	-0.192	-0.195	-5.438	-5.522
QLA6RE	0.826	0.202	0.205	5.716	5.808

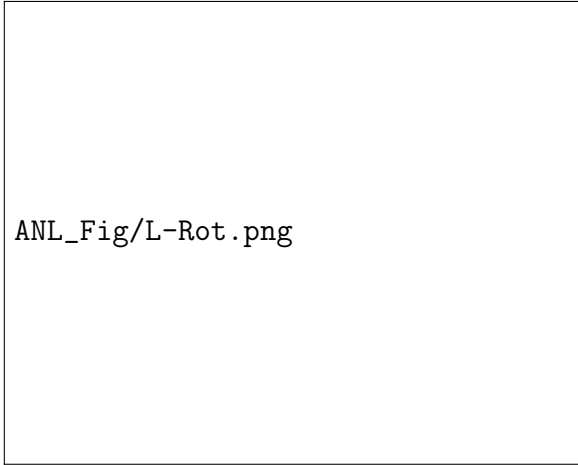
Table 22: Ring quadrupoles used for matching the optics in the R-Rot tuning region. The quadrupole magnet labels are those used in the SAD lattice file.

Skew-Quad	L(m)	k_1L	B_1 (T/m)	Tilt (rad)
B2EARSQ1	0.9837	0.435	10.341	-2.610
B2EARSQ2	0.9837	0.600	14.258	2.290
B2EARSQ3	0.9837	0.043	1.032	2.328
B2EARSQ4	0.9837	-0.566	-13.451	-0.180
B2EARSQ5	0.9837	0.600	14.258	-2.545
B2EARSQ6	0.9837	-0.591	-14.038	0.618
B2EBRSQ1	0.9837	0.495	11.769	-2.480
B2EBRSQ2	0.9837	0.532	12.648	2.238
B2EBRSQ3	0.9837	0.280	6.663	-0.960
B2EBRSQ4	0.9837	-0.565	-13.429	-0.197
B2EBRSQ5	0.9837	0.600	14.258	-2.846
B2EBRSQ6	0.9837	-0.383	-9.098	0.475


Table 23: Skew-quadrupoles of the R-Rot.

Name	L (m)	b2 (original)	b2 (Rot)
SD3TLE	1.030	-3.577	-3.789
SF6TLE	0.334	0.818	0.869
SD7TLE	1.030	-3.607	-3.819
SF8TNE	0.334	1.751	1.554
SD7NRE	1.030	-4.582	-4.788
SF6NRE	0.334	1.467	1.539
SD5NRE	1.030	-1.389	-1.573
SF4NRE	0.334	2.092	2.175
SD3NRE	1.030	-1.443	-1.628
SF2NRE	0.334	0.371	0.403
SF2NLE	0.334	0.077	0.109
SD3NLE	1.030	-3.070	-3.281
SF4NLE	0.334	0.497	0.535
SD5NLE	1.030	-1.527	-1.714
SF6NLE	0.334	0.660	0.705
SD7NLE	1.030	-1.537	-1.724
SD7FRE	0.334	-5.461	-5.652
SF6FRE	0.334	2.296	2.384
SD5FRE	1.030	-6.803	-6.954
SF4FRE	0.334	0.691	0.737
SD3FRE	1.030	-1.903	-2.099
SF2FRE	0.334	1.226	1.289
SF2FLE	0.334	0.856	0.897
SD3FLE	1.030	-1.359	-1.542
SF4FLE	0.334	0.541	0.581
SD5FLE	1.030	-2.926	-3.136
SF6FLE	0.334	2.260	2.353
SD7FLE	1.030	-6.909	-7.055
SF8FOE	0.334	1.871	1.770
SD7ORE	1.030	-7.242	-7.375
SF6ORE	0.334	0.217	0.245
SD5ORE	1.030	-2.833	-3.043
SF4ORE	0.334	1.686	1.761
SD3ORE	1.030	-3.123	-3.335
SF2ORE	0.334	0.362	0.397
SF2OLE	0.334	2.296	2.384
SD3OLE	1.030	-0.706	-0.868
SF4OLE	0.334	0.585	0.628
SD5OLE	1.030	-2.483	-2.689
SF6OLE	0.334	0.415	0.435
SD7OLE	1.030	-3.385	-3.598
SF8OTE	0.334	0.353	0.216
SD7TRE	1.030	-1.730	-1.921
SF6TRE	0.334	0.829	0.876
SD5TRE	1.030	-1.695	-1.885

Table 24: Sextupoles pairs adjusted to match the chromaticity. The sextupole magnet labels are those used in the SAD lattice file.

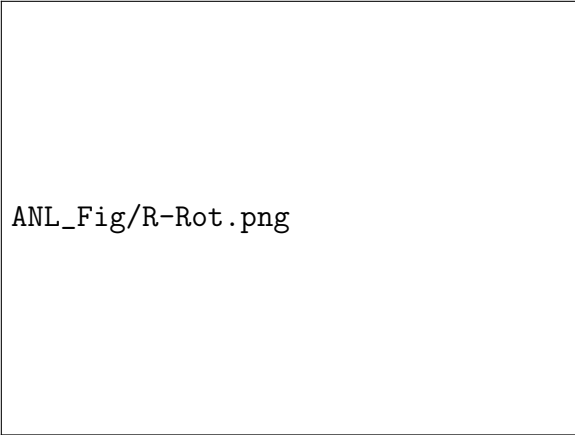


ANL_Fig/L-Rot.png




ANL_Fig/Lrot_spin.png

Figure 38: Left: Spin motion of the electron in the L-Rot (rest frame). Right: Spin motion of the electron in the L-Rot (co-moving frame).



ANL_Fig/R-Rot.png



ANL_Fig/Rrot_spin.png

Figure 39: Left: Spin motion of the electron in the R-Rot (rest frame). Right: Spin motion of the electron in the R-Rot (co-moving frame).

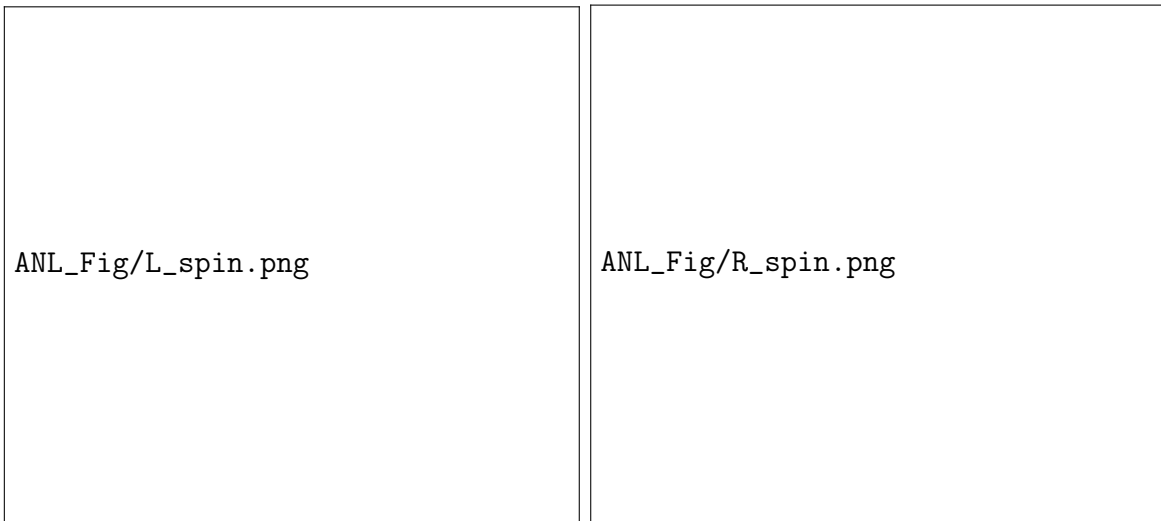


Figure 40: Left: Spin motion of the electron (co-moving frame) in the area between the L-Rot and the IP at $s \sim 3016$ m. Right: Spin motion of the electron in the area between the IP (at $s = 0$ m) and the R-Rot (co-moving frame).

,



Figure 41: Spin motion of the electron in the Rotator Ring (co-moving frame): Ip at $s = 0$ and 3016 m

9.3 Direct Wind Magnet for Spin Rotators

The seminal concept for the compact spin rotator module invented by U. Wienands' is illustrated in Figure 29. The main idea is to start with a superconducting dipole coil having a field profile that matches that of an existing SuperKEKB High Energy Ring (HER) arc dipole. Then by overlaying the field from a 4.5 T solenoid, the electron spin direction starts to rotate away from its stable, dipole field anti-parallel, orientation in the rest of the HER. By using pairs of spin rotator units located immediately upstream and then downstream of the Belle II IP in SuperKEKB, we can bring the spin to longitudinal and subsequently return it back to the anti-parallel direction. The spin rotator unit shown in Figure 29 includes additional skew-quadrupole coils to compensate locally for undesirable coupling effects introduced by the solenoidal field. The gradients of the HER lattice quadrupoles around the spin rotator units are adjusted so as to re-match the present HER lattice optics. In this manner the replacement of HER warm dipoles by the spin rotator units is “invisible” to the rest of the HER optics.

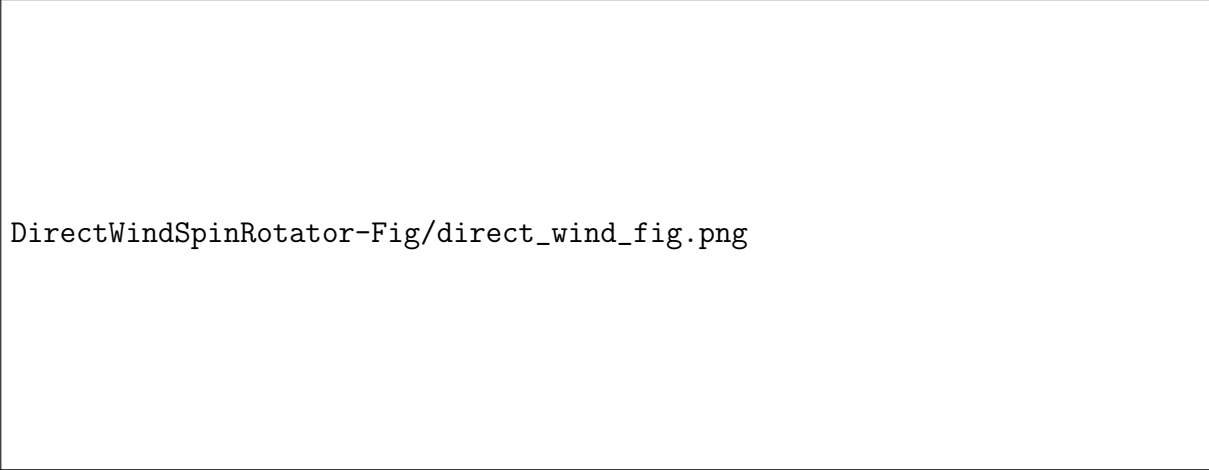
This spin rotator concept is especially attractive for use in an operating accelerator complex such as SuperKEKB because we minimize the change to the existing ring layout in the tunnel and disruption of SuperKEKB accelerator running. A standard spin rotator solution typically uses isolated solenoids separated by dipole bends designed to provide “magic angles” between the solenoids for proper spin rotation. But such a standard solution eats up precious lattice space for the solenoids and at a minimum requires shifting accelerator components in the tunnel over extended sections. Our proposed multi-function spin rotator solution minimizes the number of components that have to be physically changed or moved and maintains the present HER geometry, so it should be possible to make these changes in a standard shutdown and with lowest possible project cost.

In order to accomplish these goals our spin rotator modules must

- satisfy accelerator physics and beam optics requirements,
- have reasonable superconducting coil magnetic designs,
- be housed in an appropriate cryostat with a suitable mechanical structure,
- and have low-enough heat leak that the units can be operated each with a small number of local cryocoolers within the existing SuperKEKB tunnel.

The compact spin rotator modules needed for IP longitudinal polarization will take advantage of BNL Direct Wind production technology to make overlapping dipole, solenoidal and skew-quadrupole coils according to HER optics requirements. Direct Wind coil production involves temporarily bonding superconducting wire or round cable to a support tube as shown in Figure 42 with a picture of one layer of the SuperKEKB b5 external field cancel coil during winding next to a rendition of the skew-quadrupole coil pattern needed for our spin rotator modules. Note for the Direct Wind process, once the desired coil pattern is laid down under computer control any spaces or gaps in the winding pattern are filled in with a combination of fiberglass and epoxy and then the coil structure is wrapped with tensioned fiberglass roving to provide coil prestress against the local electromagnetic Lorentz force when the coils are cooled down and energized.

In this manner we build up the desired multi-function superconductor coil structure shown schematically in Figure 43 (for simplicity intermediate coil support tubes, cold mass containment and cryostat walls are not shown). Note that the four spin rotator modules are operated with different combinations of individual coil magnetic strengths but for the worst case, e.g. solenoid field 4.85 T, skew-quadrupole gradient 24 T/m and 0.2 T dipole field, the combined field at the skew-quadrupole conductor is 6.15 T which corresponds to 69% of the predicted short sample quench



DirectWindSpinRotator-Fig/direct_wind_fig.png

Figure 42: Direct Wind Coil Production Example. Photo on the left shows one layer of the SuperKEKB external field cancel coil during production on the BNL computer controlled winding machine. For comparison a conceptual coil winding pattern for a spin rotator skew-quadrupole is shown on the right.

value at a 729 A operating current for the preliminary configuration shown and the assumed 1.4 mm diameter 7-strand cable (at 4.22 K). While these numbers are subject to later optimization once we have a chance to do a more careful and detailed system conceptual study, this first pass analysis indicates that the proposed magnetic design is reasonable and we do not find any obvious show stoppers.

Note in order to set the coil radial buildup assumed in Figure 43 we needed to know the radius of the inner cryostat wall and this in turn depends upon both the space required to accommodate a warm HER beam pipe with features to handle synchrotron radiation and vacuum as well as the space needed for an intermediate cryostat heat shield. Since the spin rotator locations are far from existing cryogenic supplies, the cryostat units must be self-contained with integrated current leads and cryocoolers similar to what is shown in Figure 44 for the BNL AGS Snake Magnet. The specification of cryocooler capacity depends upon knowledge of the heat leak simulated using the cryostat inner cold mass support structure and the overall system design, as was done for the Oak Ridge APEX magnet system shown in Figure 45. Finally, we must show that the spin rotator module design satisfies KEK/Japanese safety and tunnel installation requirements (e.g. requirements that depend upon the net helium volume).

In summary the main spin rotator challenge that needs to be addressed is to develop a realistic, fully self-consistent conceptual design for our proposed system. To this end we submitted a proposal, “R&D for a New Belle-II Era of Polarization Physics at SuperKEKB”, for the required R&D under the U.S.-Japan Science and Technology Cooperation Program in High Energy Physics. PIs in Japan and at BNL will coordinate setting spin rotator system requirements for the conceptual design to be developed. It is anticipated that the requested US/Japan support will act as seed funding and form an initial basis for requesting future international project funding. Assuming the research and development work demonstrates that a Direct Wind magnet spin rotator can be realized in SuperKEKB while maintaining high luminosity with a polarized source, and the polarization upgrade is approved by KEK, our Canadian collaborators, led by Michael Roney, intend to submit a request to the Canadian Foundation for Innovation (CFI) towards the construction of the spin rotator magnets at BNL.

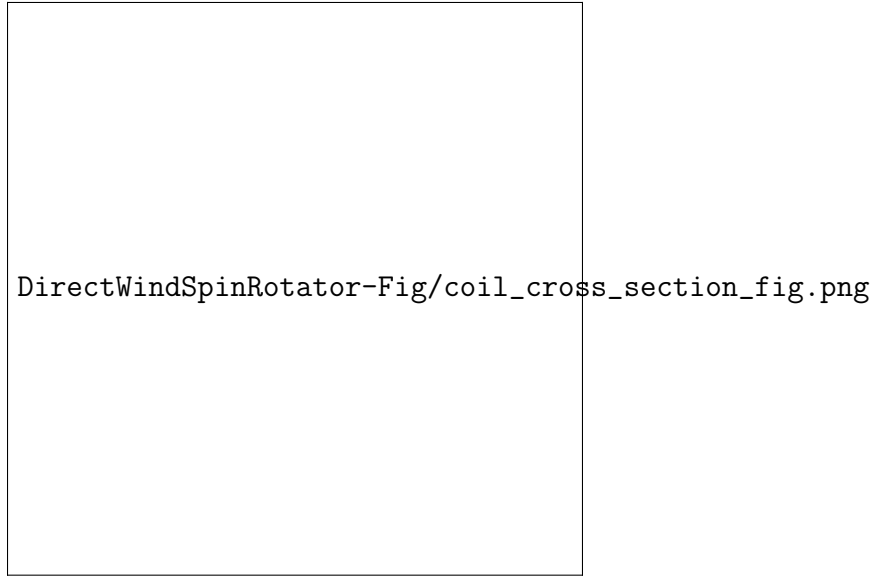


Figure 43: Conceptual Cross Section for the Proposed Multi-function Spin Rotator Coil Structure Utilizing BNL Direct Wind Technology. In this design the skew-quadrupole coil radius was minimized in order to reduce the coil magnetic peak field at the superconductor.

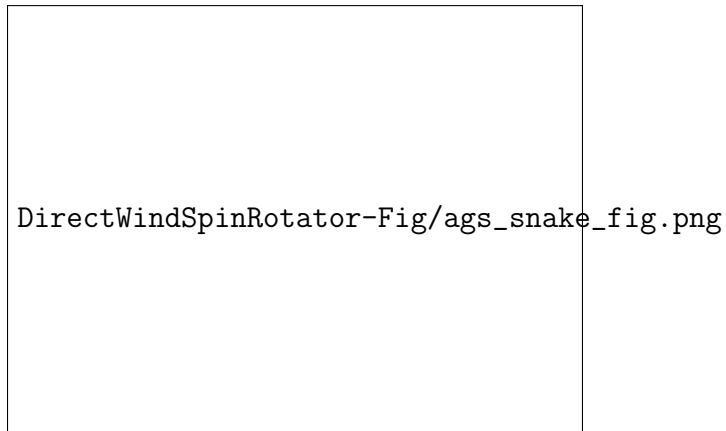


Figure 44: View of the BNL Manufactured Superconducting Snake Module Installed in the AGS Tunnel. The AGS Snake superconducting coil structure is housed in a standalone cryostat that is sandwiched in an otherwise normal conducting magnet accelerator lattice. This system uses local cryocooler based cooling along with a low heat leak support structure.



Figure 45: Cryostat Mechanical and Thermal Modeling Example. The SuperKEKB spin rotator modules will require optimization of the cryostat design with features similar to those shown here for the Oak Ridge APEX magnets. The required cryocooler capacity depends upon the thermal load from the current leads and the low heat leak support structure with intermediate temperature heat shields. The spin rotator cryostat needs a warm bore to accommodate inserting the HER beam pipe with features for synchrotron radiation heat load water cooling and beam vacuum pumping.

10 Compton Polarimetry

10.1 Introduction

Compton backscattering is a process allowing to measure accurately [77] the electron beam polarization at electron beam energies above 1 GeV. Indeed, the cross-section of this process exhibits a polarization dependent behavior [78]. This technique has been successfully employed in the past at SLC [79], at HERA [80, 81], JLAB [82] and was considered for SuperB [2]. In particular, it has enabled the demonstration and optimization of a high degree of polarization in the HERA ring [83]. It is also considered in other projects as ILC [84], LHeC [85] and EIC [86]. It is also foreseen for FCC-ee [87] in the context of energy calibration with resonant depolarization, as it was done at LEP2 [88]. For the EIC project, in the design phase, similar requirements hold.

The experimental setup consists of a circularly polarized laser beam which scatters off the electron beam. The photons are scattered within a narrow ($<1\text{mrad}$) cone around the tangent of the electron's trajectory at the interaction plane. A calorimeter can be implemented to measure the scattered gamma ray spectrum and/or a segmented electron counter placed after a dispersive element to measure the transverse electron distribution directly linked to their energy once the magnetic field is known. Both these distributions show sensitivity to the longitudinal electron beam polarization but with different sources of systematic uncertainties. It must be noted that vertical electron beam polarization may also be extracted, but would require a vertically segmented detector since the sensitivity comes from spatial asymmetries in the measured energy spectra [83, 89].

The specificities of the SuperKEKB upgrade, and similarly of EIC, lie in the fact that no permanent regime is reached, and that continuous top-up is realized to maintain a very high luminosity. It will be necessary to measure the beam polarization for every bunch independently on a timescale similar to that of the top-up period in the SuperKEKB ring. It must be noted that this measurement cannot be made at the Belle II interaction point itself, nor in the corresponding straight section due to too high backgrounds and an already very busy space. This measurement of the polarization could be extrapolated to the Belle II interaction point, provided that the lattice and alignments are well known [90]. Two possibilities could be considered. The simpler one is to place the Compton interaction point relatively close to the interaction point but far enough from the polarization rotators such that the longitudinal projection electron beam polarization vector is sufficiently large. Alternatively, the polarimeter could be placed in a region of the ring where the polarization is nearly vertical. However, in this case, the experience of HERA [80], shows that alignments must be controlled within few tens of microns, in regions of the lattice where the vertical beam size, angular spread and dispersion are negligibly small. The longitudinal polarimeter is considered as a baseline solution at this stage of the project. Three different solutions have been considered for the spin rotators. Two of them imply the spin rotators to be located at 80 m from Belle II IP, which does not allow inserting a longitudinal Compton polarimeter in the ring. A transverse Compton polarimeter would need to be studied. Implementation of combined function magnets at about 210 m upstream Belle II IP however allows inserting a longitudinal Compton polarimeter around BLA2LE where there is enough space. The polarization vector is also nearly longitudinal there, see Fig. 41. This option is further discussed below. It must be noted that the study described below is mostly a summary of a conceptual design reported elsewhere [91].

10.2 Integration

The Compton cross-section reads [78, 92]

$$\frac{d\sigma}{dy_c} = \frac{r_e^2}{x_c} (F_0(r, y_c) + P_C P_z F_{C,z}(r, y_c)), \quad (26)$$

where the F_i are functions of $y_c = \frac{E_\gamma}{E_e}$, the ratio of the energy of the scattered photon and the energy of the incoming electron, and $r = \frac{y_c}{x_c(1-y_c)}$. The parameter $x_c = \frac{2E_e h\nu_0(1+\beta \cos \theta_{in})}{m_e^2 c^4}$ is also introduced. The integration over the azimuthal direction has been performed, since only longitudinal polarization is of interest here. When designing a Compton polarimeter, there are a few things to keep in mind. The laser beam polarization needs to be circular. The longitudinal electron beam polarization can be obtained by measuring the energy distribution of the scattered particles, using calorimetric detection for photons, or a spectrometer for electrons.

10.2.1 Laser-electron beam interaction point

We will implement the laser directly in the accelerator bay close to the Compton interaction point to avoid major modifications. A 1 Gy integrated dose over 6 months of uninterrupted operations is extrapolated from measurements made at the floor level in a representative area of the accelerator. It is considered small enough [93–95]. Electronics will be further shielded with Borated Polyethylene walls surrounding electronics boards. A modified design of the beam pipe has been drawn to allow the interaction of the laser beam with the electron beam. Polar crossing angle of 8.9 degrees and azimuthal angle of 28 degrees were obtained to ease integration and avoid large radiation in the bending plane of the electron beam. Contribution to the electron beam impedance from this modification is found negligible.

An Ytterbium laser oscillator at 250 MHz locked on the accelerator RF will be used to generate laser pulses [96, 97]. The infrared light will be converted to green thanks to a second harmonic generator [82]. Beam size can be adjusted thanks to spherical or cylindrical lenses, if an elliptical laser beam is need at the interaction point. Beam position will be controlled to $100\mu\text{m}$ and $100\mu\text{rad}$, or better, thanks to commercial stabilization systems to ensure a good stability of the luminosity. The laser beam will be monitored for its intensity and polarization by means of holographic beam samplers, which will be adjusted using high-quality wave plates. Optical reversibility [82, 98] will be used to calibrate the degree of circular polarization of the laser. To this end and to minimize maintenance, we plan to implement a highly reflective mirror on a motorized mount right after the exit window of the vacuum tube, see Fig. 47.

10.2.2 Photon detector

The detector needs to cope with the 4 ns bunch separation. The dose induced by the Compton photons is expected to reach few 100 kGy. It suggests employing a radiation tolerant scintillation crystal with a fast fluorescence as BaF_2 and provided that the slow component is filtered out [99]. A prototype detector needs to be produced and tested to show the feasibility of the measurements. A length of 25 cm (about 12 X_0) seem appropriate to keep the mean energy leakage below 10% for 1.5 GeV photons [100]. The final choice of the transverse size and shape of the crystal will be performed based on detailed GEANT4 simulations and prototyping. A photomultiplier tube (PMT) will be used for the readout. We will pay attention to its choice and the design of the analog readout electronics. This remains to be done and validated with a prototype. The signal will then be digitized and treated by means of an FPGA (Field Programmable Gate Array) to fill histograms in for every bunch at 250 MHz. The possibility to reduce the interaction rate to



Figure 46: Drawing of the interaction chamber. Reproduced from [91].



Figure 47: Drawing of the insertable mirror after the exit mirror that can be used for calibration of the laser polarization. Reproduced from [91].

125 MHz or 62.5 MHz is accounted for in the design of the laser system. Final choice will rely on the detector prototyping results. In order to let the photon beam impinge the detector, the pumping ports in the sides of the beam pipe of BLA2LE must be modified and placed on the other side. The detector is placed right after the next quadrupole and vertical beam position monitor. The vacuum pipe is then modified according to Figure 48 where the detector is shown in green. A violet tube of diameter 6mm representing the photon beam is shown. It roughly corresponds to an emission cone of $\pm 3/\gamma$. The involved modification is not affecting the electron beam impedance. A 4 mm thickness of the beam pipe, where the photon beam goes through, allows shielding synchrotron radiation efficiently. Mean energy loss for photons of more than 100 MeV is estimated to be below 1% in this case. A detailed study of this effect by means of GEANT4 simulations is planned, when progress will be made on detector prototyping.

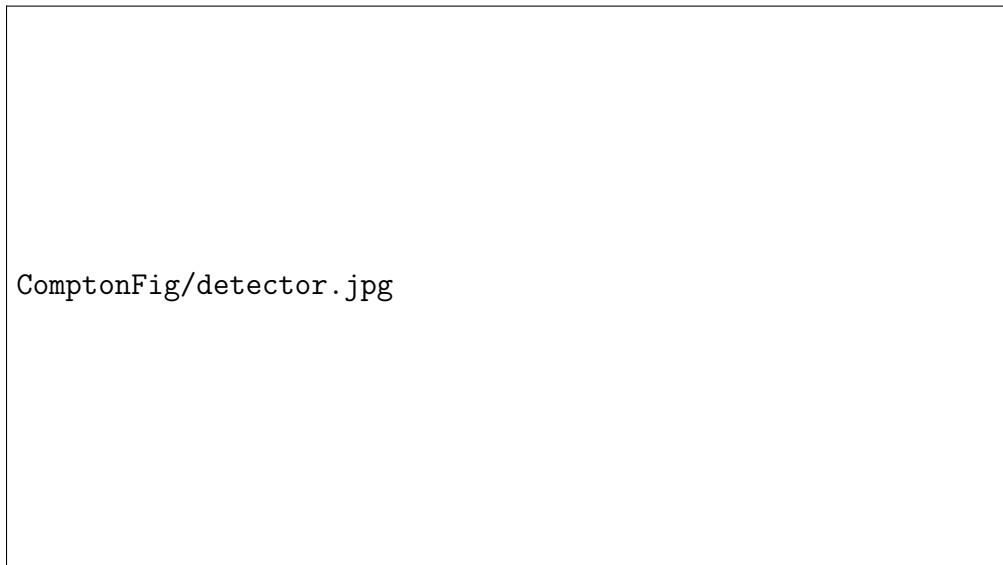


Figure 48: Drawing of the modified beam pipe for the insertion of the photon calorimeter in the SuperKEKB ring. Reproduced from [91].

10.2.3 Electron detector

An electron spectrometer employing an electron counter horizontally segmented and the dispersive magnetic element, ideally one already existing in the SuperKEKB lattice, will provide complementary information. The spectrum of the scattered electrons will be measured by a HVMAPs array. Despite this detector is slow compared to the 4 ns bunch separation, the occupancy will be much smaller compared to that of the photon calorimeter. Alternatively, diamond strips could be used, which will be naturally radiation hard and fast. However, there is at present no commercial solution for that technology.

10.3 Sensitivity studies

We describe in this section the rapid simulation that is used to assess the performance of the photon detector.

10.3.1 Event generation

The event generation is composed of few ingredients. First electrons are sampled according to the electron beam phase space at the expected Compton IP obtained from up-to-date detailed simulations of the accelerator. Second, the Compton cross-section is implemented. Thirdly backgrounds are modeled and implemented in the simulation. Finally, interaction in the detector is modeled.

Simulated electrons are generated following Refs. [101, 102], where it is assumed that beam parameters are constant in the Compton interaction region. The Twiss parameters of the beam are denoted by $\alpha_{x,y}$ and $\beta_{x,y}$, the RMS emittance by $\epsilon_{x,y}$ and the dispersion parameters $\eta_{x,y}$ and $\eta'_{x,y}$. The parameter $\sigma_\delta = \frac{\sigma_E}{\mu_E}$ is related to the energy spread of the electron beam σ_E and its mean energy μ_E . The electron beam parameters used in the simulation are summarized in Table 25.

Table 25: Table of nominal electron beam parameters used for the simulation. Reproduced from [91].

Parameter	Value	
μ_E	7 GeV	
σ_δ	6.3×10^{-4}	
Q_e	10 nC	
T_{rev}	10 μs	
P_\perp	0	
P_z	0.7	
ϕ_e	$\pi/2$	
	horizontal plane (x)	horizontal plane (y)
$\epsilon_{x,y}$	4.49×10^{-9} m.rad	4.5×10^{-11} m.rad
$\beta_{x,y}$	96.46 m	127.09 m
$\alpha_{x,y}$	-8.72	9.45
$\eta_{x,y}$	-0.083 m	-1.1×10^{-9} m
$\eta'_{x,y}$	-0.0035	6.8×10^{-11}

Compton scattering is then simulated using Eq. ?? by means of a Monte-Carlo accept-reject method. The mean number of expected photons reads $n_{\text{exp.}} = \sigma_C \mathcal{L} \approx 0.06$ where σ_C is the integrated cross-section for Compton scattering [78]. and the luminosity of the interaction is given by

$$\mathcal{L} = \frac{\lambda U Q_e}{2\pi h c q_e \sqrt{\sigma_{y,l}^2 + \sigma_{y,e}^2} \sqrt{\sigma_{x,l}^2 + \sigma_{x,e}^2 + \tan^2 \frac{\theta_{\text{in}}}{2} (\sigma_{z,l}^2 + \sigma_{z,e}^2)}}, \quad (27)$$

where λ denotes the laser wavelength, U the laser pulse energy, h the Planck constant, c the speed of light in vacuum, q_e the elementary charge. Parameters related to the laser are summarized in Table 26.

Main identified backgrounds for the measurement of photon's energy are synchrotron radiation, bremsstrahlung on the residual gas of the vacuum chamber and Compton radiation of electrons of the beam on the photons from the black-body radiation in the vacuum chamber [81]. Synchrotron radiation spectrum is estimated assuming that a 4 mm copper window is used in front of the photon detector (same material as the beam-pipe of SuperKEKB). The number of photons from synchrotron radiation passing through the window without interaction is estimated using known spectrum [103] and experimental data for absorption length in copper $\lambda_{a,\text{Cu}}(E)$ for X-rays [104, 105]. The corresponding spectrum of the non-interacting photons is found to be roughly bell-shaped at about 60 keV with a RMS width of 10 keV approximately. The total energy deposited per bunch

Table 26: Table of nominal laser beam parameters used for the simulation. Reproduced from [91].

Parameter	Value
P_C	-1
P_L	0
ϕ_l	0
$\sigma_x/\sigma_y/\sigma_z$	500 $\mu\text{m}/500 \mu\text{m}/500 \mu\text{m}$
λ	515 nm
$f_{\text{rep.}}$	250 MHz
U	20 nJ
θ_{in}	8.9 degrees
ϕ_{in}	28 degrees

crossing from synchrotron radiation is thus estimated to be about 3 keV for a 10 nC electron bunch. The related background will thus consist of a fluctuating energy pedestal that will negligibly contribute to the finite energy resolution of the measurements. We decide to further neglect this contribution in the simulation, at the current stage of the design.

The bremsstrahlung of electrons on the residual gas in the beam pipe is approximated with the differential cross-section formula [106]

$$\frac{d\sigma_{\text{BG}}}{dy_c} = \frac{4\alpha r_e^2}{y_c} \left(\left(\frac{4(1-y_c)}{3} + y_c^2 \right) \left(Z^2 \log \left(\frac{184.15}{Z^{1/3}} \right) + Z \log \left(\frac{1194}{Z^{2/3}} \right) \right) + (1-y_c) \frac{Z+Z^2}{9} \right), \quad (28)$$

where $Z \approx 2.5$ is the average atomic charge number of atoms contained in the residual gas. It is an empirical quantity that has been estimated for SuperKEKB by dedicated studies [107]. A low energy cut-off of 1 MeV is employed in the simulation. Change this figure essentially affects the yield of photons at very low energy, where there is no sensitivity of Compton spectrum to polarization.

Electrons also experience Compton scattering on the thermal photons that are in the vacuum pipe of the accelerator [108]. The number of such photons is estimated to be about 0.04 in average per bunch crossing. The average deposited energy is of 700 keV. These may seem small, but the corresponding spectrum extends towards relatively large energies, around up to 100 MeV, still in a region where there is no sensitivity to beam polarization from the Compton spectrum.

The photons' energy for Compton and bremsstrahlung processes is summed up for each simulated bunch crossing. Full containment of the electromagnetic shower is assumed. The effect of the transverse and longitudinal extensions of the electromagnetic shower is not simulated at this stage. These crude assumptions will be removed at a later stage of the design of the detector, using a detailed GEANT4 simulation. We further smear the total deposited energy with a Gaussian distribution centered on the expected total incident energy E_{in} and with a width

$$\sigma_{E_{\text{in}}} = E_{\text{in}} \sqrt{\frac{A_{\text{det.}}^2}{E_{\text{in}}} + B_{\text{det.}}^2}. \quad (29)$$

Parameters related to the detector are summarized in Table 27. For a 1 GeV incident energy, preliminary estimates suggest that the energy resolution shall be of few percents. Given the lack of a prototype at this stage of the study we will rather assume for the simulations a 10 % resolution for the stochastic term. A constant term of 1 % is also added. Attention will be paid to this contribution during the development of the detector, since one main source is related to pedestal fluctuations that may be large due to a possibly significant pile-up related to the small time-separation of the incoming photons of about 4 ns. The obtained smeared energy is then stored in a histogram that

will be further analyzed to extract the polarization parameters. Since bunches are refreshed on few minutes timescales, the measurement of the polarization is expected on a similar timescale. Over $T_{\text{meas.}} = 5 \text{ min}$ it corresponds to 30×10^6 crossings of a given electron bunch at the Compton interaction point.

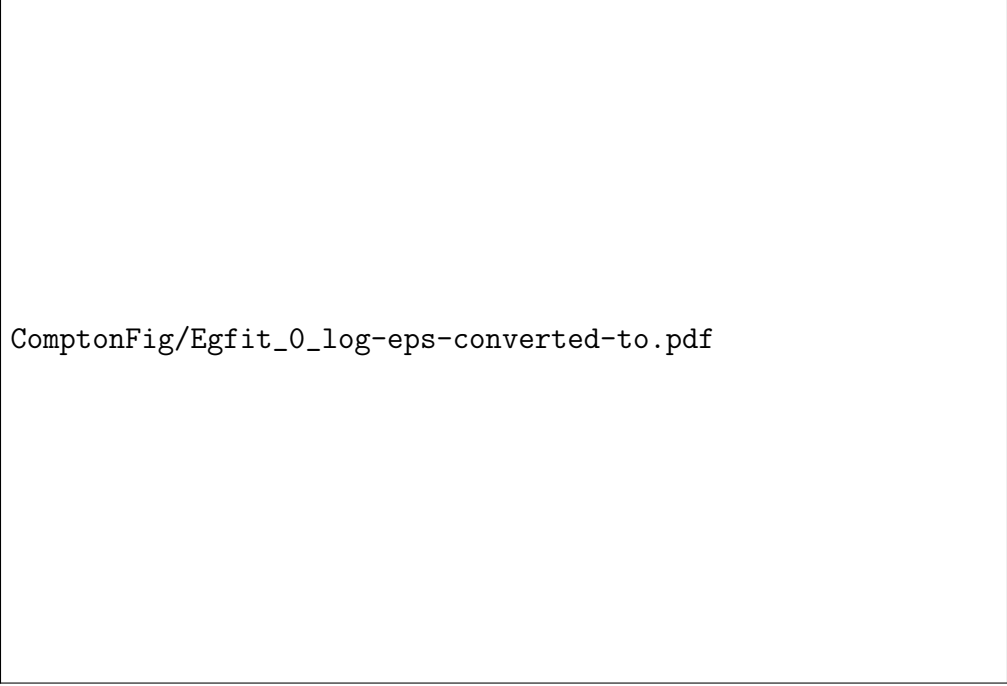
Table 27: Table of nominal parameters used to simulate the Compton interaction and the detector. Reproduced from [91].

Parameter	Value
L	13 m
$T_{\text{meas.}}$	5 min
$d_{\text{det.}}$	5 cm
$A_{\text{det.}}$	0.1 GeV ^{1/2}
$B_{\text{det.}}$	0.01


10.3.2 Fitting procedure

Fit of the generated data with the known theoretical expressions of the differential cross-sections provides sensitivity to the electron beam polarization. The model used for the bremsstrahlung background contribution is only an approximation, and the experimental results may differ to some extent. Thus, regular dedicated background measurement runs may be considered by switching off the laser and measuring the background only, dominated by the bremsstrahlung [81]. Periodicity of such background measurements will be determined by a study of the reproducibility and drifts in this distribution with time. It could also be beneficial to organize a dedicated measurement campaign of background with a prototype detector to ensure the level of background prior the polarization upgrade takes actually place. Signal and bremsstrahlung, along with their convolutions for few photons events are accounted for in the fit. Even though the calibration scale it has been found that the calibration scale can be extracted from the fit itself (assuming that the beam energy is approximately known), we assume that it is a nearly constant quantity on sufficiently short period of time such that it can be considered as a fixed parameter in the fit. Doing this, allows minimizing the fit parameters to several scale parameters and the electron beam longitudinal polarization. As implemented, the fit is extremely fast and allows extracting 2500 polarization parameters in less than a minute, i.e. could provide online polarization information. A typical fit result is shown on Fig. 49, where the generated Monte Carlo events are shown along with the fit result, explicitly showing each contribution. We note that the fit is excellent spanning over five orders of magnitude, thanks to the different characteristic energy end points of Compton and Bremsstrahlung photons.

A toy Monte Carlo procedure is applied to validate the fitting procedure and assess preliminary systematic uncertainties. The statistical precision for a single bunch is estimated by generating events corresponding to several data-taking duration t_{dt} ranging from one to 25 minutes and shown on Figure 50. The dominant source of systematic uncertainty is related to the absolute knowledge on the degree of circular laser polarization, to which 0.3% uncertainty is assigned [81], even though it may be possible to improve on this figure [82]. Systematics related to knowledge of bremsstrahlung parameter $Z = 2.50$ is assigned by performing a fit of the pure background contribution for 25 min. The obtained fit value is found unbiased with a width of 0.07, that is used to randomize this parameter at the generator level and fit with the nominal value. A bias of 0.16% is obtained and assigned as a systematic uncertainty. A small bias of 0.08% was also obtained while performing a signal only study, and is assigned as systematic uncertainty related to the underlying approximations of the fit model, that is based on look up table instead of analytical formulae to fasten the fit



ComptonFig/Egfit_0_log-eps-converted-to.pdf



ComptonFig/Egfit_0_err-eps-converted-to.pdf

Figure 49: (Top) a typical example of a Monte Carlo experiment, representing 25 min of data taking in the polarimeter. Black dots with error bars represent the Monte-Carlo data, the blue line is the fit result that is the sum of the contributions related to Compton scattering in light blue (one-photon in plain line, two-photons in dashed line, three-photons in dash-dotted line) and those related to Bremsstrahlung in magenta (one Bremsstrahlung photon in plain line, one Bremsstrahlung photon and one Compton photon in dashed line, one Bremsstrahlung photon and two Compton photons in dash-dotted line). (Bottom) residuals of the fit normalized by the statistical uncertainty in the simulated data. Reproduced from [91].

procedure. The beam energy is varied by $10\sigma_E$, and the fit procedure applied again to show that it induces a systematic uncertainty of 0.05%. Other sources of systematic uncertainties as spatial and angular misalignment and possible ignored transverse electron beam polarization are not found to bias the fit and thus assigned with an uncertainty corresponding to the statistical accuracy of this statement. These results are summarized in Table 28.



Figure 50: Statistical precision of the Compton polarimeter as a function of the duration of the data taking t_{dt} for a single bunch. For 25 minutes of data taking, a 0.5% statistical precision is obtained. Monte Carlo uncertainties on the points are negligible and smaller than the size of the points. The orange curve is a $1/\sqrt{t_{dt}}$ fit of the points, showing that the statistical behaves as expected. Reproduced from [91].

It must be noted that a detailed detector simulation and performance validation on a prototype detector is planned in order to confirm the systematic uncertainties assigned at this conceptual stage of the design of the polarimeter. It will also allow understanding the actual energy resolution and non-linearities in the energy scale. Furthermore, beam-based experiments are also needed to validate the background model with SuperKEKB data at the expected location of the polarimeter to understand its actual influence on the detector performance, since it is one of the dominant systematic uncertainties. Finally, the measurement of the longitudinal polarization of the electron at the location of the polarimeter remains to be converted to a figure at the Belle II interaction point. Fortunately, the expected polarization at the Belle II interaction point is identical to that at the Compton polarimeter, and thus the Compton polarimeter provides a meaningful measurement. However, systematic uncertainties in the spin transport remain to be evaluated in order to compare Compton polarimeter measurement with direct measurements of the electron beam polarization by use of $e^+e^- \rightarrow \tau^+\tau^-$ data.

10.4 Summary and outlook

The studies performed at this stage give confidence that commercial laser systems can be used to provide the photons that will interact with the electron beam of SuperKEKB to realize a measurement of electron beam polarization with Compton backscattering. Expected statistical precision

Table 28: Systematic uncertainties on the extraction of P_z , see text for details. Background modeling and absolute knowledge of the laser polarization dominates. Reproduced from [91].

Source	Uncertainty on P_z (%)
Laser beam polarization	0.30
Backgrounds	0.16
Fit procedure	0.080
Beam energy	0.050
Spatial misalignment	0.015
Angular misalignment	0.015
Longitudinal misalignment	0.015
Transverse electron beam polarization	0.015
Total	0.35

of this device is better than 1% per minute for each bunch. Residual systematic uncertainties are expected to lie well below 1%. One of the key aspects related to the laser beam is the control and survey of its polarization components that enter into the systematic uncertainties for the extraction of the polarization of the electron beam. Some limited R&D work needs to be performed on this topic to ensure a precise and accurate estimation in the SuperKEKB environment with the laser system under consideration. It is planned to use the existing/upgraded SuperKEKB lattice with minor modifications related to the insertion of the laser interaction chamber and the photon and electron detectors. Existing technology based on HVMAPS can be implemented for the counting of electrons, with no specific need for a dedicated R&D program. A measurement of the scattered photon spectrum using a BaF2 crystal coupled to a PMT could complementarily be implemented. It is expected to be compliant with the short time-separation of bunches at SuperKEKB. This may be confirmed with some limited R&D to ensure the performance of this system.

11 Touschek Polarimetry

11.1 Introduction

The first step of the upgrade consists in demonstrating that the required current of polarized electron beam can be produced, transported in the linac to the main SuperKEKB ring and stored for a long enough time without loss of vertical polarization. The next stage would consist in actually implementing modifications to the main SuperKEKB ring by inserting spin rotators and a Compton polarimeter to ensure and optimize a longitudinal polarization at the Belle II interaction point. In order to avoid modifications to the main ring prior a demonstration that significantly polarized electron bunches can be stored in SuperKEKB, it is of interest to find a simple, possibly non-invasive technique to diagnose the beam polarization in SuperKEKB. We investigate here the possibility to do so by means of Touschek lifetime measurements.

This part is organized as follows. First we introduce the dependence of the Touschek lifetime as a function of beam polarization. We investigate its impact for the SuperKEKB ring. In a second section, we investigate the present status of Touschek lifetime measurements in the SuperKEKB ring that are presently made in the context of beam background diagnostics for the Belle II experiment. We finally list the needs for a meaningful polarization measurement at SuperKEKB.

11.2 Touschek lifetime and polarization

Touschek described the lifetime of electrons in AdA (accumulation ring) in 1963 [109], as a result of Moeller scattering in between electrons of a beam in a ring. Right after, Baier and Khoze pointed out that the Touschek lifetime is sensitive to polarization [110]. It was then used in the VEPP-2M ring to measure depolarization, and in turn the beam energy, by measuring the counting rate of scattered electrons [111]. It allowed to realize a first precision mass measurement of the J/Psi, that was continuously improved until it reached a few parts per million accuracy on the beam energy measurement at VEPP-4M [112]. Since then it has been continuously used by the accelerator physics community to measure beam polarization, also at the most modern synchrotron light sources, see for instance [113–115] and is planned to be used at FCC-ee too [87].

In order to quantitatively investigate the effect of beam polarization on the Touschek lifetime at SuperKEKB we follow the formalism developed in Ref. [87, 116, 117], where a flat beam approximation is being used. It is obtained after calculations that the ratio of Touschek lifetimes with and without polarization reads

$$\frac{\tau_T(P=0)}{\tau_T(P)} = 1 + \frac{\langle \tilde{F}(\xi) \rangle_s}{\langle \tilde{C}(\xi) \rangle_s} P^2, \quad (30)$$

where P denotes the beam polarization, τ_T the Touschek lifetime, $\langle . \rangle_s$ the average over the ring circumference, the coordinate of which is written s ; and

$$\tilde{F}(\xi) = a(s)F(\xi) \quad (31)$$

$$\tilde{C}(\xi) = a(s)C(\xi) \quad (32)$$

$$F = -\frac{\xi}{2} \int_{\xi}^{\infty} \frac{1}{u^2} \log\left(\frac{u}{\xi}\right) e^{-u} du \quad (33)$$

$$C(\xi) = \xi \int_{\xi}^{\infty} \frac{1}{u^2} \left[\frac{u}{\xi} - \frac{1}{2} \log\left(\frac{u}{\xi}\right) - 1 \right] e^{-u} du \text{ and} \quad (34)$$

$$\xi(s) = \left(\frac{\delta\beta_x(s)}{\gamma\sigma_x(s)} \right)^2 \quad (35)$$

$$a(s) = \frac{N_e c r_e^2 \sqrt{\xi}}{8\pi\gamma^2 \sigma_x(s) \sigma_y(s) \sigma_s(s) \delta^3} \quad (36)$$

where $\log(\cdot)$ denotes the natural logarithm, δ the relative momentum acceptance that we assume to be 6.3×10^{-3} [118] despite it is expected to be s -dependent, β_x the horizontal betatron function, σ_x the transverse beam size, $\gamma \approx 13700$ is the Lorentz boost of the electrons in the SuperKEKB ring, r_e the classical radius of the electron, c the speed of light in vacuum and N_e the number of electrons in a bunch. The need to average over the ring circumference is related to the fact that ξ is related to the horizontal betatron function. This ratio is estimated for SuperKEKB with the SAD lattice file `her_2021-06-09_231636.388_MeasOpt` that provides betatron function and beam size. It must be noted that ξ is actually subject to possibly large systematic uncertainties related to the fact that the actual momentum acceptance, and lattice parameters are difficult to estimate. Note that the bunch population cancels in the ratio.

We observe that the ratio $\frac{\tilde{F}(\xi)}{\tilde{C}(\xi)}$ varies by approximately 20% in most of the ring except in the four long straight sections (Tsukuba, Oho, Fuji, Nikko) where it varies by up to a factor three. The importance of the s -dependence on the ratio of lifetimes, is tested by also computing the average value of $\langle \xi \rangle_s$ in the SuperKEKB ring, and computing

$$\frac{\tau_T(P=0)}{\tau_T(P)} = 1 + \frac{\tilde{F}(\langle \xi \rangle_s)}{\tilde{C}(\langle \xi \rangle_s)} P^2, \quad (37)$$

instead. In that case the effect of the misknowledge of the beam volume cancels in the ratio of lifetimes, which is not exactly the case since it weighs the integrands of the calculation. It corresponds to a relative change in the ratio of lifetimes of five percents. Misknowledge of $\xi(s)$ also affects this prediction. If in the present calculation δ is overestimated by a factor 10, the ratio of the lifetime drops to a two percent increase for a nominally polarized beam. The variation of the ratio of Touschek lifetime for $P = 0.7$ as a function of ξ is shown in Fig. 52.

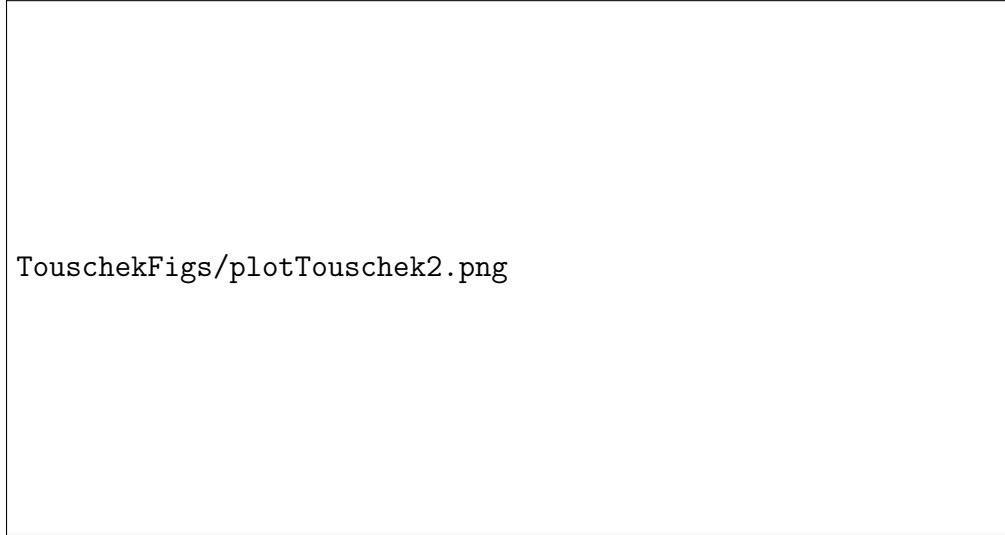


Figure 51: Ratio of the Touschek lifetimes with and without a polarized beam versus the polarization of the beam. A nominally polarized beam at 70% induces a change of beam lifetime of approximately 5%.

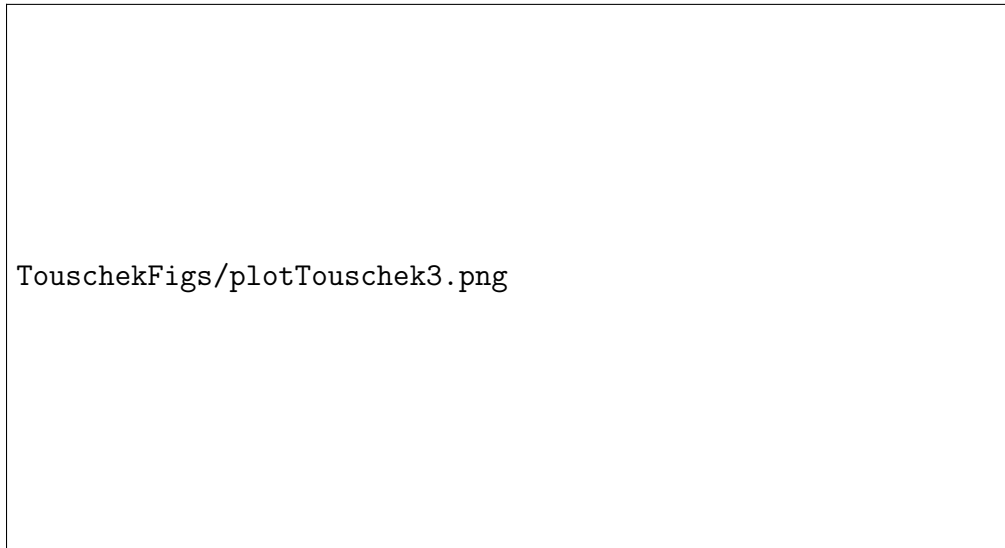


Figure 52: Ratio of the Touschek lifetimes with and without a polarized beam ($P = 0.7$) versus the value of $\langle \xi \rangle_s$.

11.3 s-dependance of Touschek lifetime

Within approximations described in the text, it is also possible to compute the contribution to the Touschek lifetime as function of s . It is shown in Fig. 53. The contribution to the lifetime from

the tightly focused region of Belle II IP is marginally contributing to the average, with the lattice parameters used. The obtained lifetime is of 83 min for a 5 nC bunch charge. The s -dependence of the ratio of polarized/unpolarized beam Touschek lifetime is also given in Fig. 54.



Figure 53: Contribution to the Touschek lifetime as a function of the coordinate s . The black line shows the value averaged over the whole circumference.

11.4 Touschek lifetime measurement at SuperKEKB

We now turn to the question of the precision with which this ratio of lifetime can be measured at SuperKEKB. The following study is based on previous works made for Belle II beam induced background studies [107, 119, 120] with some refinements. Beam induced background measurements are realized a couple of times per year. These are typically made over a day by varying the number of bunches and currents separately in both positron (LER) and electron (HER) rings, and then by analyzing data during collisions. For the present discussion we are mostly interested in the lifetime measurement in the HER. Beam is filled in with bunch numbers varying from 400 to 1600 with a given measured current in the accelerator. The beam is then left evolving without top-up injection. The decay of the beam charge thus allows to measure the beam lifetime, which is a combination of (i) elastic and inelastic scattering of electrons off the residual gas of the imperfect vacuum; (ii) inelastic scattering of particles within a bunch, i.e. the Touschek contribution. During collisions, additional losses must be accounted for. These are related to physics processes, as radiative Bhabha and

TouschekFigs/plotTouschek-sdepRatio.png

Figure 54: Contribution to the ratio of Touschek lifetimes with polarized/unpolarized beams as a function of the coordinate s .

$e^+e^- \rightarrow e^+e^-e^+e^-$ process. Since the dependence of Touschek and beam-gas losses as a function of the number of bunches and bunch charge is different, their magnitude can be extracted from data. The lifetime is measured directly from data by computing

$$\tau_{\text{meas.}} = I / \left(\frac{\Delta I}{\Delta t} \right), \quad (38)$$

where $\frac{\Delta I}{\Delta t}$ is extracted every 10 s, and I denotes the measured beam current. This is a measured quantity and can be fit using the heuristic formula as discussed in Ref. [120]:

$$\frac{\Delta I}{\Delta t} = B \times I \bar{P}_{\text{eff.}} + T \times \frac{I^2}{n_{\text{b}} \sigma_x \sigma_y \sigma_z} \quad (39)$$

where B and T are beam-gas and Touschek loss sensitivities, respectively; $\bar{P}_{\text{eff.}}$ is the effective average gas pressure seen by the beam and estimated using measurements of Cold Cathode Gauges (CCGs) installed around each ring [120], and it is linearly proportional to the beam current; n_{b} is the number of bunches; σ_x and σ_y are transverse beam sizes, and $\sigma_z = 6.0211 + 1.3711 \times I/n_{\text{b}}$ is the bunch length, which depends on the beam current and number of bunches due to the bunch lengthening. It must be noted that recent dedicated beam studies suggest that another scaling law may be more appropriate $\sigma_z = 5.140 + 0.832 \times I/n_{\text{b}}$ [121]. Using these two different expressions is expected to have a small effect on the ratio of Touschek lifetimes.

Figure 55 shows an example of beam loss studies conducted on May 9, 2020 in the HER. As shown in Fig. 55 (bottom), the LER beam was dumped, and we started with only HER beam at $n_{\text{b}} = 783$. After about 5 min of top-up injection at $I = 500$ mA, the injection stopped and the beam was let to decay due to beam losses around the ring. Having collected enough data we dumped the beam, changed the number of bunches, and repeated the measurements. One can see that during non-injection, beam decay periods (blue hatched area) the measured by the SuperKEKB group

TouschekFigs/HER_BeamLossRateFit_20200509.pdf

Figure 55: Example of beam loss rate measurements on May 9, 2020. Top: calculated HER beam loss rate; bottom: SuperKEKB machine parameters. See text for detailed discussion.

total beam lifetime (green markers) follows the beam current and beam loss change according to Eq. 38. The calculated beam loss rate $\Delta I/\Delta t$ every 10 s is shown in Fig. 55 (top). As expected the quantity follows the beam current changes according to Eq. 39.

By fitting the data with Eq. 39 using the TMinuit Class [122] from the CERN ROOT framework [123], we extract beam loss sensitivities B and T for beam-gas and Touschek components, respectively. Figure 55 (top) illustrates the result of the non-injection data fit (red hatched area). Table 29 lists heuristic fit parameters for four dedicated beam loss studies conducted in 2020-2021 with different beam optics as indicated by β_y^* the vertical betatron function at the interaction point. Each study corresponds to different beam and machine settings, including collimators (see Fig. 56), residual gas pressure, and beam currents.

Table 29: HER beam loss sensitivities for four dedicated measurements at SuperKEKB in 2020-2021.

Date	β_y^*	Beam-gas (B) $\times 10^{-6}$	Touschek (T)	χ^2/ndf
May 9, 2020	1.0 mm	225.01 ± 1.24	1189.97 ± 1.78	0.70
June 27, 2020	0.8 mm	487.18 ± 2.24	1341.05 ± 2.57	0.71
June 16, 2021	1.0 mm	142.67 ± 4.45	1616.06 ± 5.81	0.14
December 20, 2021	1.0 mm	83.04 ± 3.80	1872.26 ± 6.11	0.12

The uncertainty for each beam parameter used in the heuristic fit can be summarized as follows:

- I (BMHDCCT:CURRENT): the systematic uncertainty for the HER beam current is $10 \mu\text{A}$ [124];
- $\sigma_{x/y}$ (BMHXRM:BEAM:SIGMA[X/Y]): the systematic uncertainties for transverse beam sizes are $10/1 \mu\text{m}$;
- \bar{P}_{eff} . (VAHCCG:D[i]_HER:PRES:AVG): since the relative uncertainty for the individual CCG is 10%, we assume the relative uncertainty for HER sections of $10\%/\sqrt{N}$, where N is the number of CCGs in the given section D[i], see Fig. 56.

All mentioned beam parameters are stored as 1 Hz time series of process variables (PVs) provided by the EPICS-based slow-control system of Belle II. The name of the corresponding PV is indicated in parentheses. The measured transverse beam sizes should be corrected before using them in the fit due to a specific X-ray monitor technique described in Ref. [124]:

$$\sigma_{\text{corr.}} = \sqrt{\sigma_{\text{meas.}}^2 - \sigma_{\text{off.}}^2}, \quad (40)$$

where $\sigma_{\text{corr.}}$ stands for the corrected transverse beam size, $\sigma_{\text{meas.}}$ is the measured quantity, and the offset $\sigma_{\text{off.}}$ is $10 \mu\text{m}$ and $7 \mu\text{m}$ for σ_x and σ_y , respectively. Moreover, the potentially overestimated uncertainties for the measured transverse beam sizes presumably explain a noticeable *over-fitting* (i.e. $\chi^2/ndf < 1$).

Using the heuristic fit parameters listed in Table 29 and the measured beam parameters, we can estimate beam lifetime for each background source during the operation. Figure 57 shows the estimated beam lifetime using heuristic fit results for May 2020 studies. It is seen that the Touschek lifetime (τ_T) is at least two times lower than the beam-gas (τ_B), and it strongly depends on the bunch current (I/n_b), as expected. Therefore, the total single-beam lifetime (τ) is mainly defined by intrabeam scatterings due to the Touschek effect since:

$$\frac{1}{\tau} = \frac{1}{\tau_T} + \frac{1}{\tau_B}. \quad (41)$$

TouschekFigs/CollimatorMap.pdf

Figure 56: Map of the SuperKEKB collimators used in 2021 and 2022. The letters V and H in the collimator names indicate vertical and horizontal movable jaws, respectively. There are twelve sections in each ring named D01 through D12.

TouschekFigs/HER_BeamLifeTime_20200509.pdf

Figure 57: Estimated (Est.) beam lifetime during dedicated beam loss studies in May 2020 using fit results listed in Table 29.

The accuracy with which the ratio of lifetime will be measured for a given lattice configuration of the accelerator will thus depend on i) the relative magnitude of the beam-gas contribution to the lifetime and its uncertainty related to the knowledge of the pressure, ii) the accuracy of the beam current and bunch volume measurements. Fit results show that the parameter T is extracted with a relative precision of less than 1%. As shown in Fig. 51, this relative uncertainty would translate in a 5-10% uncertainty on the beam polarization.

This statement implicitly assumes that optical functions and bunch lengths are very constant when performing these measurements with and without polarization. In order to minimize such a possible change, it is assumed that we would inject bunches with and without polarization in the same beam. The number of bunches and the relative proportions of polarized and unpolarized bunches could be varied in similar manner as that done currently for beam losses studies. It would also be necessary to measure independently the beam volume for all bunches separately to minimize the systematic uncertainty related to a non constant transverse bunch size over the beam. Thus a relative correction could be applied provided relative bunch charges are known. This procedure will require an upgrade of bunch-by-bunch beam size monitors, to store the full information without decimation, as it is currently.

In order to translate the measurement of the ratio of Touschek lifetimes into a measurement of the polarization, it is needed to know the factor $\langle \xi \rangle$. This implies to know the beam size, the horizontal emittance and the momentum acceptance.

Finally, beam-beam interactions at the Belle II may also contribute in depolarizing the beam. Thus it would be interesting to realize these measurements while beam-beam effects take place. However it sounds a difficult task since beam-beam effects effectively correspond to a modification of the betatron function of the accelerator. Moreover, Beamstrahlung will modify the bunch length and thus the bunch volume. These modifications may be different for polarized and unpolarized bunches and bunch-by-bunch. Instead we thus consider to perform a first measurement of the ratio of Touschek lifetimes, put beams into collision for some time, dump the positron beam, and perform again a measurement of the ratio of Touschek lifetime.

11.5 Conclusion

We have investigated the possibility to use relative measurement of Touschek lifetimes with polarized and unpolarized beams to demonstrate that polarized beams are actually well produced, transported to and stored into the SuperKEKB HER ring. This will allow to avoid implementing modifications to the SuperKEKB and has the ability to provide a low-cost approach in the first stage of the project.

12 Tau Polarimetry

As mentioned in the Physics Case, a precise determination of the average beam polarization is required to maximize the sensitivity of the planned measurements. Due to the left handed nature of the weak nuclear force the τ particle is uniquely suited for gaining access to beam polarization. This is due in part to the τ decaying while inside the detector and secondly the kinematics of the decay products are sensitive to the τ spin state. The spin state of the tau produced in an $e^+e^- \rightarrow \tau^+\tau^-$ directly couples to the helicity of the electron beam as shown in Equation 42.

$$P_\tau = P_e \frac{\cos\theta}{1 + \cos^2\theta} - \frac{8G_{FS}}{4\sqrt{2}\pi\alpha} g_V^\tau \left(g_A^\tau \frac{|\vec{p}|}{p^0} + 2g_A^e \frac{\cos\theta}{1 + \cos^2\theta} \right) \quad (42)$$

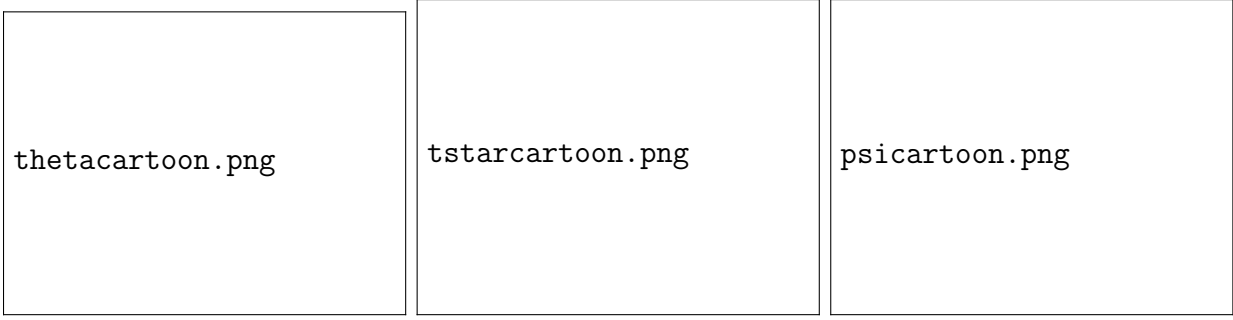


Figure 58: Cartoons illustrating $\cos \theta$ (left, f represents a final state particle), $\cos \theta^*$ (center), and $\cos \psi$ (right).

Where P_ℓ is the polarization of the tau or electron, $\cos \theta$ is the opening angle between the tau and the electron beam, G_F and α are the Fermi constant and fine structure constant respectively, and $g_{V,A}^\ell$ are the vector and axial neutral current couplings for their respective leptons. The work we present in this section is focused on determining the polarization sensitivity in the $\tau^\pm \rightarrow (\rho^\pm \rightarrow \pi^\pm \pi^0) \nu_\tau$ decay mode and determining the associated statistical and systematic uncertainties. This decay mode was chosen for the large branching fraction of the tau decay, 25.93%, as well as the high tau pair purity achievable with a lepton tag on the other tau decay. For this ρ decay three angular variables are required to extract the beam polarization. The polarization sensitive variables are defined in equations in 43 and 44 [125].

$$\cos \theta^* = \frac{2z - 1 - m_\rho^2/m_\tau^2}{1 - m_\rho^2/m_\tau^2} \quad z \equiv \frac{E_\rho}{E_{\text{beam}}} \quad (43)$$

$$\cos \psi = \frac{2x - 1}{\sqrt{1 - m_\pi^2/m_\rho^2}} \quad x \equiv \frac{E_\pi}{E_\rho} \quad (44)$$

For the mass of the pion and the tau we use the PDG values, while for the mass of the rho we used the event-by-event reconstructed $\pi\pi^0$ mass. $\cos \theta^*$ is defined as the opening angle between the between the tau flight path in the center-of-mass frame and rho direction in the tau rest frame. Similarly $\cos \psi$ is the opening angle between the rho flight direction in the center-of-mass frame and the pion direction in the rho rest frame. Forward and backward regions are defined from the direction of the final state momentum with respect to the beam axis, $\cos \theta$, and the prior angular variables reverse their polarization behaviour switching between these regions. Figure 58 illustrates the angular definitions. The distributions of these variables are depicted in Figures 59, 60, and 61 for different values of the electron beam polarization.

12.1 Event Selection

A preliminary study of this technique has been implemented at *BABAR* in order to identify dominant uncertainties. At *BABAR* the event selection is designed to select tau pair events where each of the tau particles decay into a single charged particle. One tau lepton, labelled the as the tag, is required to decay leptonically into an electron while the other tau, the signal, decays into a charged and a neutral pion. Figure 62 shows this event topology. This requirement for a single charged hadron and a single charged lepton excludes nearly all Bhabha, $\mu\mu$, and $q\bar{q}$ events. The requirement of the neutral pion on the signal side of the event significantly reduces any remaining Bhabha events which contain one electron misidentified as a pion. The remaining Bhabha events are further reduced by

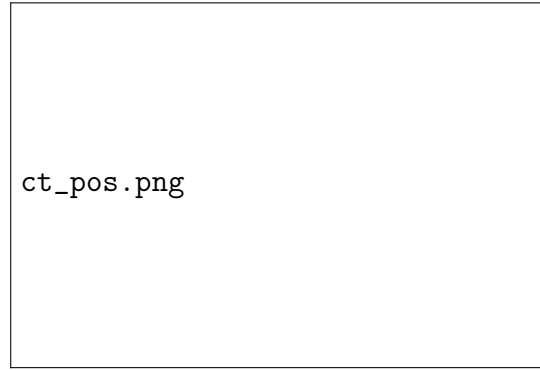


Figure 59: $\cos \theta$ distribution in MC for positively charged rho decay.

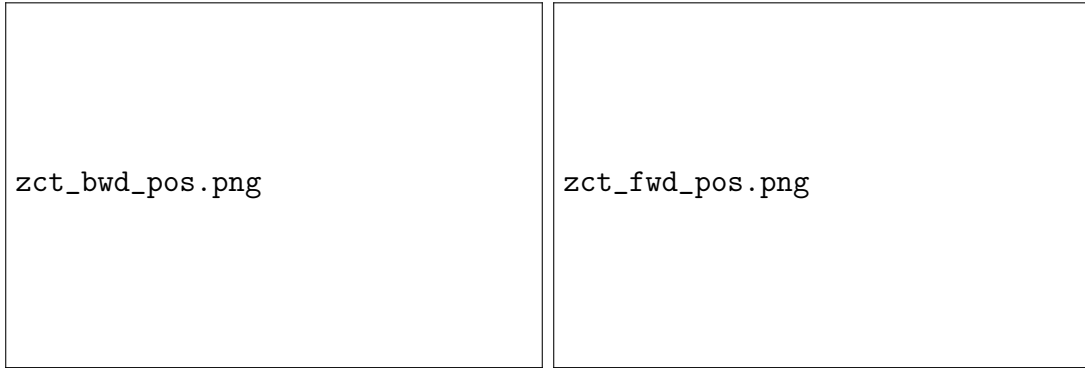


Figure 60: $\cos \theta^*$ distribution in MC for positively charged rho decay. For $\cos \theta < 0$ (left) and $\cos \theta > 0$ (right).

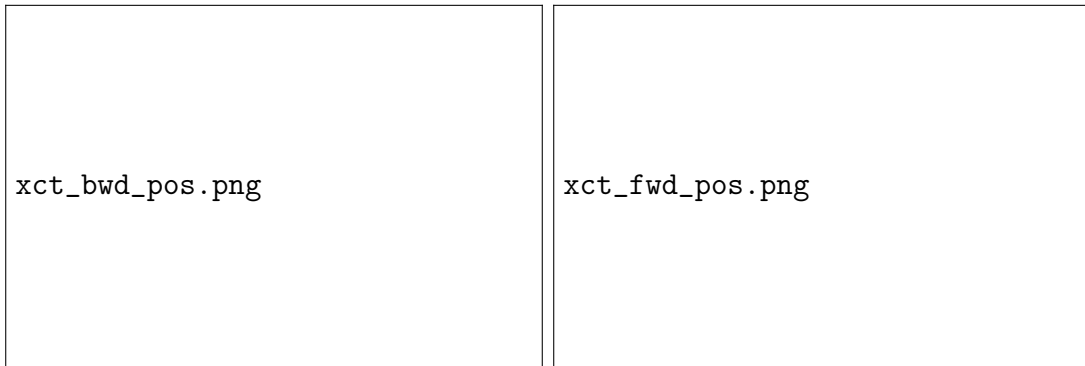


Figure 61: $\cos \psi$ distribution in MC for positively charged rho decay. For $\cos \theta < 0$ (left) and $\cos \theta > 0$ (right).

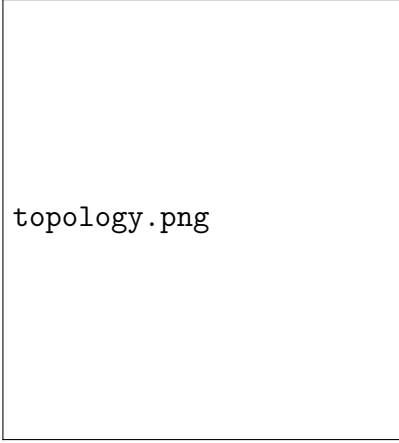


Figure 62: Example tau-pair decay. Signal $\tau^\pm \rightarrow (\rho^\pm \rightarrow \pi^\pm \pi^0) \nu_\tau$ decay tagged with a $\tau^\pm \rightarrow e^\pm \bar{\nu}_e \nu_\tau$ decay

MC source	Fraction	Tau Signal	Fraction
Bhabha	0.289%	$\tau^\pm \rightarrow e^\pm \bar{\nu}_e \nu_\tau$	0.012%
$\mu^+ \mu^-$	0.000%	$\tau^\pm \rightarrow \mu^\pm \bar{\nu}_\mu \nu_\tau$	0.018%
$u\bar{u}, d\bar{d}, s\bar{s}$	0.005%	$\tau^\pm \rightarrow \pi^\pm \nu_\tau$	0.033%
$c\bar{c}$	0.002%	$\tau^\pm \rightarrow (\rho^\pm \rightarrow \pi^\pm \pi^0) \nu_\tau$	89.994%
$b\bar{b}$	0.000%	$\tau^\pm \rightarrow (a_1^\pm \rightarrow \pi^\pm \pi^0 \pi^0) \nu_\tau$	8.028%
$\tau^+ \tau^-$	99.704%	$\tau \rightarrow \text{else}$	1.915%

Table 30: Fraction of event types in MC in the final event selection. The tau pair events are further broken down to show the $\tau^\pm \rightarrow (\rho^\pm \rightarrow \pi^\pm \pi^0) \nu_\tau$ selection.

a factor of three by slightly trimming $\cos \theta^*$, $-1 < \cos \theta^* < 0.9$, and $\cos \psi$, $-0.9 < \cos \psi < 1$. These requirements achieve a final tau selection which is 99.7% pure and with a 0.70% efficiency. The branching fraction for the tagging tau is 17.82% and 25.49% for the signal tau. Including these in our efficiency calculation, brings our efficiency to 15.40% for selecting $\tau^\pm \tau^\mp \rightarrow \rho^\pm \nu_\tau + e^\mp \nu_e \bar{\nu}_\tau$ events. Our largest non-tau background is Bhabha events which make up 0.3% of the final sample. The final event selection break-down as predicted by MC is shown in Table 30.

12.2 Fitting

To extract the average beam polarization we perform a binned likelihood fit as described by Barlow and Beeston [126]. We fill three dimensional histograms of $\cos \theta^*$, $\cos \psi$, and $\cos \theta$, for each of the data and MC modes. The 3D histogram for data is then fit as a combination of the MC histograms, where the weights of the non-tau MC is fixed based on the MC efficiency studies. This leaves only the left and right polarized contribution to vary in the fit, and with a restraint that the contributions sum to 1 leaves only one parameter in the fit. We define this fitted parameter as $\langle P \rangle = L - R$, where L and R are the fitted fractions reported by the fit for the left and right polarized tau MC. As the polarization sign flips with electric charge we perform the fit separately for positively and negatively charged signal candidates, and extract the fit result, statistical uncertainty, the chi squared as defined by TFractionFitter, and the number of degrees of freedom (bins in fit with an event minus one fit parameter). A final fit result is then reported as the combined average of the two independent fits. In addition to the data fit we use unpolarized tau MC mixed with non-tau MC to produce three “data-like” samples for approximating the level of statistical uncertainty present in

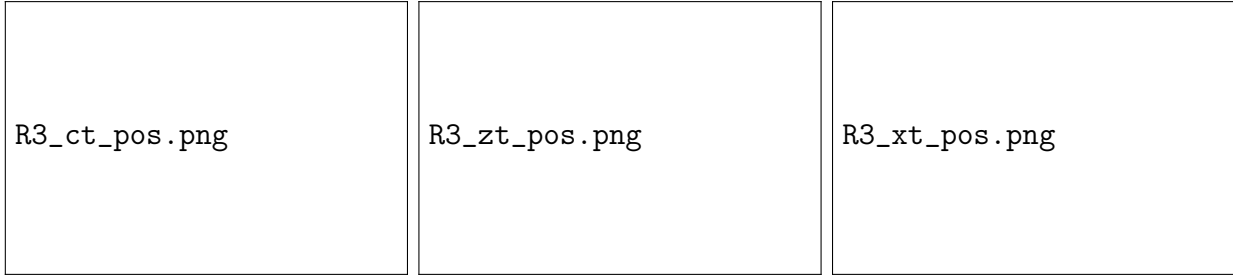


Figure 63: One dimensional projection of the fit result for $\cos \theta$ (left), $\cos \theta^*$ (middle), and $\cos \psi$ (right) in positively charged candidates in Run 3.

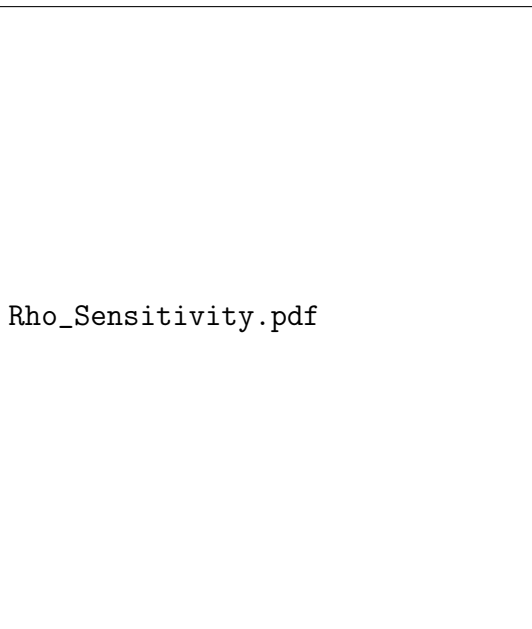
small perturbations to the fit. Figure 63 shows the 1D projections of the run 3 fit, where the data points represent the data and the MC is stacked with relative proportions equal to the fit results. As the *BABAR* data sets are split into multiple data collection periods, run numbers 1 to 6, and each set has its own unique beam conditions we treat each sample independently. As such we obtain 6 measurements of the beam polarization and corresponding statistical and systematic uncertainties. A final measurement of the beam polarization is then obtained from combining these measurements and accounting for correlations in the systematic uncertainties.

12.3 Extracted vs Input Beam Polarization Study

In order to ensure the polarimetry measurement is valid at beam polarization states other than 0, as expected for PEP-II runs, we used polarized tau MC to study the extracted polarization from this analysis of the rho channel at multiple input beam polarization states. This was done by splitting each of the left and right polarized tau MC into two distinct samples, one reserved for fitting the beam polarization in MC “measurements” and the other for mixing beam polarization states. With the samples reserved for mixing beam polarization states specific beam polarization states can be created, ie. 70% polarized is made with 85% left polarized MC and 15% right polarized MC. Using this technique we tested polarization states from -1 to 1 in steps of 0.1, the results of which can be seen in Figure 64. The fit results to the MC are within good agreement of the input MC beam polarization states, which demonstrates the measurement technique will yield the correct polarization for any beam polarization.

12.4 Systematic Uncertainties

Systematic uncertainties are evaluated by studying the response in the MC and data polarization fits as we systematically vary parameters in the fit templates. To evaluate the systematic uncertainty corresponding to a particular source, the fit is performed in a “default” mode then repeated with some variation in the systematic source. The shift in data, as well as the average shift in MC is found, and the relative shift in the agreement between data and MC is taken as the systematic uncertainty. In order to approximate the level of statistical uncertainty present in the measurement we split the MC into 3 independent samples, each roughly equal in size to the data set being studied, and take the RMS of the shifts in the MC as a statistical uncertainty on the systematic uncertainty. This provides both a central value for the systematic shift and a statistical uncertainty on the systematic uncertainty. As a conservative measure, in the case the statistical component is larger than the central value of the systematic uncertainty we list the statistical part as the systematic uncertainty. As systematic uncertainties are expected to be run dependent we treat each run independently and started with *BABAR* Run 3 as a study sample as the data set, which



Rho_Sensitivity.pdf

Figure 64: Measured beam polarization for a given input polarization mixed from polarized tau MC. The red points correspond to the measurements for positively charged signal candidates while the blue points correspond to the negatively charged candidates.

represents 32.3 fb^{-1} , is relatively small. The following systematic uncertainties discussed in this section are the result of the Run 3 studies. In order to determine the level of variation required to accurately evaluate a potential systematic source, the mean of the distributions for the variable are compared between data and MC. The level of disagreement between data and MC is taken as the uncertainty in the variable and used in the systematic uncertainty tests. For the cuts applied to $\cos \psi$, the cut was varied from $\cos \psi > -0.9$ up and down to $\cos \psi > -0.91$ and $\cos \psi > -0.89$. This resulted in an overall shift in the level of agreement between data and MC in the polarization fit of -0.0007 ± 0.0013 . As the statistical component dominates, we list 0.0013 as the uncertainty seen in Table 31. A similar approach for $\cos \theta^*$ results in a systematic uncertainty of -0.0002 ± 0.0001 , or 0.0002 in our final table. To evaluate the uncertainties arising from our treatment of neutral clusters we vary the thresholds for the related cutoffs. In the case of the hadronic split-off modelling the relevant variable is the distance within we associate neutral clusters with charged particles, 40 cm by default. The MC suggests the resolution for the distance between a charged particle and a neutral cluster is better than 1cm. By varying the acceptance cut by 1 cm a systematic uncertainty of 0.27% was estimated. For the minimum neutral energy, 50 MeV, as well as the photon energy cutoff for π^0 reconstruction, 100 MeV, we vary the acceptance by ± 1 MeV, as dictated by the level of agreement between MC and data. Both of these variables resulted in small systematic uncertainties of 0.13% and 0.11% respectively. The systematic uncertainty for momentum resolution is evaluated by scaling the momentum up or down based on its resolution and results in a 0.02% systematic uncertainty in the polarization fit. Similarly for $\cos \theta$ the angle is varied by its resolution and results in a 0.10% systematic uncertainty. The π^0 identification systematic uncertainty was evaluated by varying the mass window for the reconstructed π^0 's by 1 MeV or by tweaking the π^0 likelihood acceptance by 5, depending which selection criteria selected a particular π^0 . The combined systematic uncertainty for the π^0 identification is 0.19%. In addition to already mentioned variables, similar studies were performed on the τ trigger decision, the boost calculation, the charged track definition, the total event transverse momentum, uncertainties within the τ branching fraction, the weights of non- τ backgrounds, the luminosity weighting of the MC, the effects of re-binning in the fit, the electron

PID requirements, and the cuts on $\cos\psi$ and $\cos\theta^*$. None of these exhibited any notable effects. After carrying out the full measurement on the remaining *BABAR* data-sets the run-by-run systematic uncertainties were combined in a process that accounts for correlations between the runs. Table 31 shows the systematic uncertainties for each run as well as the final uncertainty for each systematic source once correlations are accounted for. The individual uncertainties are summed in quadrature to arrive at the total uncertainty shown in the final row.

Source	Final
π^0 Likelihood	0.0015
Hadronic Split-off Modelling	0.0011
$\cos\psi$	0.0010
Angular Resolution	0.0009
Minimum Neutral Energy	0.0009
π^0 Mass	0.0009
$\cos\theta^*$	0.0008
Electron PID	0.0007
Tau Branching Fraction	0.0006
Event Transverse Momentum	0.0005
Momentum Resolution	0.0005
π^0 Minimum Photon Energy	0.0004
Rho Mass	0.0003
Background Modelling	0.0003
Boost	0.0002
Total	0.0030

Table 31: Summary of systematic uncertainties associated with polarization measurement.

12.5 Preliminary results from *BABAR* Beam Polarization Fit

The fit results for all of the *BABAR* data sets are shown in Table 32. Taking the weighted mean of these fit results gives the average beam polarization of PEP-II runs to be $\langle P \rangle = 0.0001 \pm 0.0035_{\text{stat}} \pm 0.0030_{\text{sys}}$ with a sample of 0.4 ab^{-1} . We can estimate that 56 fb^{-1} of data is needed to achieve a total uncertainty of 1%, where the statistical uncertainty scales with $1/\sqrt{N_{\text{Events}}}$. The absolute systematic uncertainty of ± 0.003 demonstrates that a 0.4% relative systematic uncertainty on a beam polarization of 70% can be achieved in e^+e^- colliders, and with sufficient statistics represents the achievable total uncertainty. Such a precise beam polarization measurement in SuperKEKB enables the high precision electroweak measurements. These preliminary results have been presented at the Lake Louise Winter Institute Conference[127].

13 Summary and Next Steps

Unique and powerful sensitivities to new physics via precision neutral current measurements at 10 GeV are enabled by an upgrade of SuperKEKB to have polarized electron beams. With a measurement of $\sin^2\theta_W$ having a precision comparable to the current world-average Z^0 -pole value, but at 10 GeV, Chiral Belle will be uniquely sensitive to the presence of dark sector parity violating bosons with masses below the Z^0 . Moreover, it would be the only facility able to probe neutral current universality relations between charm and beauty quarks and all three charged leptons at

Data Set	Luminosity (fb ⁻¹)	Positive Charge	χ^2/NDF	Negative Charge	χ^2/NDF	Average Polarization
Run 1	20.37	-0.0018±0.0222	934/881	0.0143±0.0224	1022/882	0.0062±0.0157
Run 2	61.32	-0.0064±0.0127	785/884	0.0056±0.0128	819/877	-0.0004±0.0090
Run 4	99.58	0.0054±0.0101	890/888	-0.0280±0.0100	832/883	-0.0114±0.0071
Run 5	132.33	0.0053±0.0092	914/886	-0.0124±0.0087	993/886	-0.0040±0.0063
Run 6	78.31	0.0256±0.0117	939/881	0.0060±0.0116	1022/882	0.0157±0.0082
Total	424.18	0.0070±0.0052		-0.0087±0.0051		-0.0010±0.0036

Table 32: Average beam polarization measured in each data set. The average for each run is found from the weighted mean of the positive and negative fit results.

energies below the Z^0 pole and would measure ratios of neutral current couplings with unprecedentedly high precision. The τ -pairs produced with polarized beams will also provide the only means to measure the third-generation $g-2$ at a precision that can begin to approach the $\mathcal{O}(10^{-6})$ level, the equivalent of the muon $g-2$ anomaly scaled by $(m_\tau/m_\mu)^2$ as expected in Minimal Flavor Violation scenarios. With 40 ab⁻¹, a measurement at the 10^{-5} is possible and to reach $\mathcal{O}(10^{-6})$ will require more statistics as well as improved measurements of m_τ and $M_{\Upsilon(1S)}$. Other physics will also benefit from the polarization, including lepton flavor violation searches in τ decays, τ Michel parameter measurements, τ EDM measurements and QCD hadronization studies.

It has been demonstrated that the challenging problem of providing a spin rotator that is transparent to the rest of the SuperKEKB lattice can be solved, with some options being presented in this paper. Developments of a polarized source are underway, as are solutions for implementing Compton polarimeters. Unique to the Chiral Belle program is the additional means of measuring the beam polarization at the IP using τ pair events with a relative systematic uncertainty of 0.4%, as described in this paper.

The next steps involve developing a Technical Design with cost estimates. The capital costs for such an upgrade are expected to be substantially less than half of the annual power costs of operating the SuperKEKB accelerator. It can also be expected that a significant fraction of those capital costs will be provided by non-Japanese groups on Belle II. It is possible to plan for the upgrade to commence during a long shutdown at the end of this decade and completed over a number of summer shutdowns following such a long shutdown. In such a scenario, the polarization program could begin while SuperKEKB completes its program of delivering 50 ab⁻¹ of data to Belle II and continued beyond that program.

References

- [1] S. Schael *et al.* (ALEPH, DELPHI, L3, OPAL, SLD, LEP Electroweak Working Group, SLD Electroweak Group, SLD Heavy Flavour Group), *Phys. Rept.* **427**, 257 (2006), [arXiv:hep-ex/0509008](#).
- [2] M. Baszczyk *et al.* (SuperB), (2013), [arXiv:1306.5655 \[physics.ins-det\]](#).
- [3] J. Erler and A. Freitas (Particle Data Group), *Phys. Rev. D* **98**, 030001 (2018).
- [4] D. Becker *et al.*, *Eur. Phys. J. A* **54**, 208 (2018), [arXiv:1802.04759 \[nucl-ex\]](#).

- [5] J. Benesch *et al.* (MOLLER), (2014), [arXiv:1411.4088 \[nucl-ex\]](#).
- [6] H. Davoudiasl, H.-S. Lee, and W. J. Marciano, *Phys. Rev. D* **92**, 055005 (2015), [arXiv:1507.00352 \[hep-ph\]](#).
- [7] M. Pospelov and A. Ritz, *Phys. Lett. B* **671**, 391 (2009), [arXiv:0810.1502 \[hep-ph\]](#).
- [8] N. Arkani-Hamed, D. P. Finkbeiner, T. R. Slatyer, and N. Weiner, *Phys. Rev. D* **79**, 015014 (2009), [arXiv:0810.0713 \[hep-ph\]](#).
- [9] B. Batell, D. McKeen, and M. Pospelov, *Phys. Rev. Lett.* **107**, 011803 (2011), [arXiv:1103.0721 \[hep-ph\]](#).
- [10] R. Pohl *et al.*, *Nature* **466**, 213 (2010).
- [11] C. Hearty, “Measurement of A_{LR} with muon pairs and a polarized electron beam at SuperKEKB,” (2021), BELLE2-NOTE-PH-2021-012 L.
- [12] A. Aleksejevs, S. Barkanova, C. Miller, J. M. Roney, and V. Zykunov, *Phys. Rev. D* **101**, 053003 (2020), [arXiv:1801.08510 \[hep-ph\]](#).
- [13] B. Aubert *et al.* (BaBar), *Phys. Rev. D* **69**, 011103 (2004), [arXiv:hep-ex/0310027](#).
- [14] J. P. Lees *et al.* (BaBar), *Phys. Rev. Lett.* **125**, 241801 (2020), [arXiv:2005.01230 \[hep-ex\]](#).
- [15] W. Altmannshofer *et al.* (Belle-II), *PTEP* **2019**, 123C01 (2019), [Erratum: *PTEP* **2020**, 029201 (2020)], [arXiv:1808.10567 \[hep-ex\]](#).
- [16] F. Abudinén *et al.* (Belle-II), *Phys. Rev. Lett.* **127**, 211801 (2021), [arXiv:2108.03216 \[hep-ex\]](#).
- [17] X. C. Tian *et al.* (Belle), *Phys. Rev. Lett.* **95**, 231801 (2005), [arXiv:hep-ex/0507071](#).
- [18] A. G. Aleksejevs, S. G. Barkanova, Y. M. Bystritskiy, and V. A. Zykunov, *Physics of Atomic Nuclei* **83**, 463 (2020).
- [19] F. Abudinén *et al.* (Belle-II), *Chin. Phys. C* **44**, 021001 (2020), [arXiv:1910.05365 \[hep-ex\]](#).
- [20] R. Sadykov and V. Yermolchyk, *Comput. Phys. Commun.* **256**, 107445 (2020), [arXiv:2001.10755 \[hep-ph\]](#).
- [21] J. Abdallah *et al.* (DELPHI), *Eur. Phys. J. C* **35**, 159 (2004), [arXiv:hep-ex/0406010](#).
- [22] G. A. González-Sprinberg, A. Santamaria, and J. Vidal, *Nucl. Phys. B* **582**, 3 (2000), [arXiv:hep-ph/0002203](#).
- [23] B. Abi *et al.* (Muon $g - 2$), *Phys. Rev. Lett.* **126**, 141801 (2021), [arXiv:2104.03281 \[hep-ex\]](#).
- [24] T. Aoyama *et al.*, *Phys. Rept.* **887**, 1 (2020), [arXiv:2006.04822 \[hep-ph\]](#).
- [25] S. Eidelman and M. Passera, *Mod. Phys. Lett. A* **22**, 159 (2007), [arXiv:hep-ph/0701260](#).
- [26] A. Crivellin, M. Hoferichter, and J. M. Roney, (2021), [arXiv:2111.10378 \[hep-ph\]](#).
- [27] J. H. Kühn, *Phys. Lett. B* **313**, 458 (1993), [arXiv:hep-ph/9307269](#).

- [28] J. Bernabéu, G. A. González-Sprinberg, J. Papavassiliou, and J. Vidal, *Nucl. Phys. B* **790**, 160 (2008), [arXiv:0707.2496 \[hep-ph\]](#).
- [29] J. Bernabéu, G. A. González-Sprinberg, and J. Vidal, *JHEP* **01**, 062 (2009), [arXiv:0807.2366 \[hep-ph\]](#).
- [30] J. Bernabéu, G. A. González-Sprinberg, and J. Vidal, *Phys. Lett. B* **326**, 168 (1994).
- [31] J. Bernabéu, G. A. González-Sprinberg, and J. Vidal, *Nucl. Phys. B* **763**, 283 (2007), [arXiv:hep-ph/0610135](#).
- [32] P. Zyla *et al.* (Particle Data Group), *PTEP* **2020**, 083C01 (2020), and 2021 update.
- [33] M. J. Booth, (1993), [arXiv:hep-ph/9301293](#).
- [34] U. Mahanta, *Phys. Rev. D* **54**, 3377 (1996), [arXiv:hep-ph/9604380](#).
- [35] W. Bernreuther, A. Brandenburg, and P. Overmann, *Phys. Lett. B* **391**, 413 (1997), [Erratum: *Phys.Lett.B* 412, 425–425 (1997)], [arXiv:hep-ph/9608364](#).
- [36] T. Huang, W. Lu, and Z.-j. Tao, *Phys. Rev. D* **55**, 1643 (1997), [arXiv:hep-ph/9609220](#).
- [37] K. Inami *et al.* (Belle), (2021), [arXiv:2108.11543 \[hep-ex\]](#).
- [38] G. A. Gonzalez-Sprinberg, J. Bernabeu, and J. Vidal, in *23rd International Symposium on Lepton-Photon Interactions at High Energy (LP07)* (2007) [arXiv:0707.1658 \[hep-ph\]](#).
- [39] B. Ananthanarayan and S. D. Rindani, *Phys. Rev. D* **51**, 5996 (1995), [arXiv:hep-ph/9411399](#).
- [40] W. Bernreuther, L. Chen, and O. Nachtmann, *Phys. Rev. D* **103**, 096011 (2021), [arXiv:2101.08071 \[hep-ph\]](#).
- [41] D. G. Hitlin *et al.*, (2008), [arXiv:0810.1312 \[hep-ph\]](#).
- [42] B. Aubert *et al.* (BaBar), *Phys. Rev. Lett.* **104**, 021802 (2010), [arXiv:0908.2381 \[hep-ex\]](#).
- [43] A. Matsuzaki and A. I. Sanda, *Phys. Rev. D* **77**, 073003 (2008), [arXiv:0711.0792 \[hep-ph\]](#).
- [44] B. M. Dassinger, T. Feldmann, T. Mannel, and S. Turczyk, *JHEP* **10**, 039 (2007), [arXiv:0707.0988 \[hep-ph\]](#).
- [45] A. Accardi and A. Signori, *Phys. Lett. B* **798**, 134993 (2019), [arXiv:1903.04458 \[hep-ph\]](#).
- [46] A. Accardi and A. Signori, *Eur. Phys. J. C* **80**, 825 (2020), [arXiv:2005.11310 \[hep-ph\]](#).
- [47] A. Accardi and J.-W. Qiu, *JHEP* **07**, 090 (2008), [arXiv:0805.1496 \[hep-ph\]](#).
- [48] A. Accardi and A. Bacchetta, *Phys. Lett. B* **773**, 632 (2017), [arXiv:1706.02000 \[hep-ph\]](#).
- [49] D. Boer, R. Jakob, and P. Mulders, *Nucl.Phys.* **B504**, 345 (1997), [arXiv:hep-ph/9702281 \[hep-ph\]](#).
- [50] D. Boer, *Nucl. Phys. B* **806**, 23 (2009), [arXiv:0804.2408 \[hep-ph\]](#).
- [51] P. J. Mulders and R. D. Tangerman, *Nucl. Phys. B* **461**, 197 (1996), [Erratum: *Nucl. Phys. B* **484**, 538 (1997)], [arXiv:hep-ph/9510301](#).

- [52] A. Accardi *et al.*, (2022), [arXiv:2204.02280](https://arxiv.org/abs/2204.02280) [hep-ex].
- [53] D. Pierce, F. Meier, and P. Zürcher, [Appl. Phys. Lett.](#) **26**, 670 (1975).
- [54] X. Jin, B. Ozdol, M. Yamamoto, A. Mano, N. Yamamoto, and Y. Takeda, [Applied Physics Letters](#) **105**, 203509 (2014).
- [55] M. Kuriki and K. Masaki, [IPAC2019](#) , [TUPTS026](#) (2019).
- [56] M. Boge and T. Limberg, [Conf. Proc. C](#) **950501**, 2901 (1996).
- [57] M. Bieler *et al.*, in *Workshop on Beam-Beam Effects in Large Hadron Colliders* (1999) pp. 12–19.
- [58] J. Shi, L. Jin, and G. Hoffstaetter (2003).
- [59] Y. Ohnishi, H. Koiso, A. Morita, H. Sugimoto, and K. Oide, [Conf. Proc. C](#) **110904**, 3694 (2011).
- [60] Y. Onishi (SuperKEKB accelerator group), [PoS ICHEP2016](#), 006 (2016).
- [61] A. Zholents and V. Litvinenko, <https://inspirehep.net/files/feeab64bfc358327614578468cfff5bb>, preprint YAF 81-80 (1981), also in DESY-L-TRANS-289.
- [62] G. Luijckx *et al.*, [Conf. Proc. C](#) **970512**, 1063 (1997).
- [63] Y. S. Derbenev and A. M. Kondratenko, [Sov. Phys. JETP](#) **37**, 968 (1973).
- [64] V. I. Ptitsyn, Ph.D. thesis, Novosibirsk (1997), in Russian.
- [65] V. I. Ptitsyn, Y. M. Shatunov, and S. R. Mane, [Nucl. Instrum. Meth. A](#) **608**, 225 (2009).
- [66] I. A. Koop, A. V. Otboev, P. Y. Shatunov, and Y. M. Shatunov, [AIP Conf. Proc.](#) **915**, 948 (2007).
- [67] V. N. Litvinenko and A. A. Zholents, (2018), [arXiv:1809.11138](https://arxiv.org/abs/1809.11138) [physics.acc-ph].
- [68] B. Parker, M. Anerella, J. Escallier, A. Ghosh, A. Jain, A. Marone, J. Muratore, and P. Wanderer, [IEEE Trans. Appl. Supercond.](#) **22**, 4101604 (2012).
- [69] Y. Peng, *Conceptual Design of the Spin Rotator for the SuperKEKB High Energy Ring*, Master’s thesis, University of Victoria (2022).
- [70] D. Sagan, “The bmad reference manual,” <https://www.classe.cornell.edu/bmad/manual.html> (2021).
- [71] D. Zhou, M. Biagini, N. Carmignani, H. Koiso, S. Liuzzo, A. Morita, Y. Ohnishi, K. Oide, D. Sagan, and H. Sugimoto, in *7th International Particle Accelerator Conference* (2016) p. WEPOY040.
- [72] D. Sagan and D. Rubin, [Phys. Rev. ST Accel. Beams](#) **2**, 074001 (1999).
- [73] Y. Suetsugu *et al.*, [Phys. Rev. Accel. Beams](#) **22**, 023201 (2019).

- [74] K. Wille, *The physics of particle accelerators: an introduction* (Oxford University Press, 2000).
- [75] K. Akai, K. Furukawa, and H. Koiso (SuperKEKB), *Nucl. Instrum. Meth. A* **907**, 188 (2018), [arXiv:1809.01958 \[physics.acc-ph\]](#).
- [76] D. Sagan, “Long term tracking program,” https://www.classe.cornell.edu/bmad/other_manuals.html (2021).
- [77] A. Denner and S. Dittmaier, *Nucl. Phys. B* **540**, 58 (1999), [arXiv:hep-ph/9805443](#).
- [78] I. F. Ginzburg, G. L. Kotkin, S. L. Panfil, V. G. Serbo, and V. I. Telnov, *Nucl. Instrum. Meth. A* **219**, 5 (1984).
- [79] R. C. King (SLD), *Nucl. Phys. B Proc. Suppl.* **37**, 23 (1994).
- [80] D. P. Barber *et al.*, *Nucl. Instrum. Meth. A* **329**, 79 (1993).
- [81] S. Baudrand *et al.*, *JINST* **5**, P06005 (2010), [arXiv:1005.2741 \[physics.ins-det\]](#).
- [82] A. Narayan *et al.*, *Phys. Rev. X* **6**, 011013 (2016), [arXiv:1509.06642 \[nucl-ex\]](#).
- [83] D. P. Barber *et al.*, *Nucl. Instrum. Meth. A* **338**, 166 (1994).
- [84] S. Boogert *et al.*, *JINST* **4**, P10015 (2009), [arXiv:0904.0122 \[physics.ins-det\]](#).
- [85] J. L. Abelleira Fernandez *et al.* (LHeC Study Group), *J. Phys. G* **39**, 075001 (2012), [arXiv:1206.2913 \[physics.acc-ph\]](#).
- [86] W. Deconinck, “Polarization Upgrade and Polarimetry at the SuperKEKB Belle II Facility,” (2020).
- [87] A. Blondel *et al.*, “Polarization and centre-of-mass energy calibration at fcc-ee,” (2019), [arXiv:1909.12245 \[physics.acc-ph\]](#).
- [88] R. Assmann *et al.* (LEP Energy Working Group), *Eur. Phys. J. C* **39**, 253 (2005), [arXiv:hep-ex/0410026](#).
- [89] N. Muchnoi, *Journal of Instrumentation* **17**, P10014 (2022).
- [90] M. Beckmann, J. List, A. Vauth, and B. Vormwald, *JINST* **9**, P07003 (2014), [arXiv:1405.2156 \[physics.acc-ph\]](#).
- [91] D. Charlet, T. Ishibashi, A. Martens, M. Masuzawa, F. Mawas, Y. Peinaud, D. Zhou, and F. Zomer, *Journal of Instrumentation* **18**, P10014 (2023).
- [92] O. Klein and Y. Nishina, *Zeitschrift für Physik* **52**, 853 (1929).
- [93] G. Buchs, S. Kundermann, E. Portuondo-Campa, and S. Lecomte, *Opt. Express* **23**, 9890 (2015).
- [94] Y.-S. Jang, J. Lee, S. Kim, K. Lee, S. Han, Y.-J. Kim, and S.-W. Kim, *Opt. Lett.* **39**, 2831 (2014).
- [95] S. Girard, A. Laurent, E. Pinsard, T. Robin, B. Cadier, M. Boutillier, C. Marcandella, A. Boukenter, and Y. Ouerdane, *Opt. Lett.* **39**, 2541 (2014).

- [96] U. Keller, *Applied Physics B* **100**, 15 (2010).
- [97] M. N. Zervas, *International Journal of Modern Physics B* **28**, 1442009 (2014), <https://doi.org/10.1142/S0217979214420090>.
- [98] N. Vansteenkiste, P. Vignolo, and A. Aspect, *J. Opt. Soc. Am. A* **10**, 2240 (1993).
- [99] R.-Y. Zhu, *Journal of Physics: Conference Series* **1162**, 012022 (2019).
- [100] R. L. Workman *et al.* (Particle Data Group), *PTEP* **2022**, 083C01 (2022).
- [101] P. Chen, G. Horton-Smith, T. Ohgaki, A. Weidemann, and K. Yokoya, *Nuclear Instruments and Methods in Physics Research Section A: Accelerators, Spectrometers, Detectors and Associated Equipment* **355**, 107 (1995), gamma-Gamma Colliders.
- [102] K. Yokoya, “CAIN:user manual,” .
- [103] J. D. Jackson, *Classical electrodynamics*, 3rd ed. (Wiley, New York, NY, 1999).
- [104] S. M. Seltzer, *Radiation Research* **136**, 147 (1993).
- [105] NIST, “X-ray mass attenuation coefficients,” .
- [106] Y.-S. Tsai, *Rev. Mod. Phys.* **46**, 815 (1974).
- [107] Z. Liptak, A. Paladino, L. Santelj, J. Schueler, S. Stefkova, H. Tanigawa, N. Tsuzuki, A. Aloisio, P. Ahlburg, P. Bambade, G. Bassi, M. Barrett, J. Baudot, T. Browder, G. Casarosa, G. Cautero, D. Cinabro, G. Claus, D. Cuesta, F. Di Capua, S. Di Carlo, J. Flanagan, A. Frey, B. Fulsom, Y. Funakoshi, M. Gabriel, R. Giordano, D. Giuressi, M. Goffe, K. Hara, O. Hartbrich, M. Hedges, D. Heuchel, N. Iida, T. Ishibashi, K. Jaaskelainen, D. Jehanno, S. de Jong, T. Kraetzschmar, C. La Licata, L. Lanceri, P. Leitl, P. Lewis, C. Marinias, C. Miller, H. Moser, K. Nakamura, H. Nakayama, C. Niebuhr, Y. Onuki, C. Pang, B. Paschen, I. Ripp-Baudot, G. Rizzo, J. Roney, H. Schreeck, B. Schwenker, F. Simon, M. Specht, B. Spruck, Y. Soloviev, M. Szelezniak, S. Tanaka, S. Terui, G. Tortone, T. Tsuboyama, Y. Uematsu, S. Vahsen, L. Vitale, and H. Windel, *Nuclear Instruments and Methods in Physics Research Section A: Accelerators, Spectrometers, Detectors and Associated Equipment* **1040**, 167168 (2022).
- [108] V. Telnov, *Nuclear Instruments and Methods in Physics Research Section A: Accelerators, Spectrometers, Detectors and Associated Equipment* **260**, 304 (1987).
- [109] C. Bernardini, G. F. Corazza, G. Di Giugno, G. Ghigo, J. Haissinski, P. Marin, R. Querzoli, and B. Touschek, *Phys. Rev. Lett.* **10**, 407 (1963).
- [110] V. N. Baier and V. A. Khoze, *Soviet Atomic Energy* **25**, 1256 (1968).
- [111] Y. Derbenev, A. Kondratenko, and E. Saldin, *Nuclear Instruments and Methods* **165**, 15 (1979).
- [112] V. Blinov *et al.*, *Nuclear Instruments and Methods in Physics Research Section A: Accelerators, Spectrometers, Detectors and Associated Equipment* **494**, 81 (2002), proceedings of the 8th International Conference on Instrumentation for Colliding Beam Physics.

- [113] C. Sun, J. Zhang, J. Li, W. Wu, S. Mikhailov, V. Popov, H. Xu, A. Chao, and Y. Wu, *Nuclear Instruments and Methods in Physics Research Section A: Accelerators, Spectrometers, Detectors and Associated Equipment* **614**, 339 (2010).
- [114] J. Zhang, L. Cassinari, M. Labat, A. Nadji, L. Nadolski, and D. Pédeau, *Nuclear Instruments and Methods in Physics Research Section A: Accelerators, Spectrometers, Detectors and Associated Equipment* **697**, 1 (2013).
- [115] N. Vitoratou, P. Karataev, and G. Rehm, *Phys. Rev. Accel. Beams* **22**, 122801 (2019).
- [116] T.-Y. Lee, J. Choi, and H. Kang, *Nuclear Instruments and Methods in Physics Research Section A: Accelerators, Spectrometers, Detectors and Associated Equipment* **554**, 85 (2005).
- [117] *CAS - CERN Accelerator School : 5th General Accelerator Physics Course: Jyväskylä, Finland 7 - 18 Sep 1992. CAS - CERN Accelerator School : 5th General Accelerator Physics Course*, CERN (CERN, Geneva, 1994) 2 volumes, consecutive pagination.
- [118] “Superkekb design report,” .
- [119] P. Lewis *et al.*, *Nuclear Instruments and Methods in Physics Research Section A: Accelerators, Spectrometers, Detectors and Associated Equipment* **914**, 69 (2019).
- [120] A. Natochii *et al.*, *Nuclear Instruments and Methods in Physics Research Section A: Accelerators, Spectrometers, Detectors and Associated Equipment* **1055**, 168550 (2023).
- [121] T. I. et al., “Impedance modelling and single-bunch collective 2 instability simulation in superkekb main ring,” .
- [122] CERN ROOT, “TMinuit Class Reference,” <https://root.cern.ch/doc/master/classTMinuit.html>.
- [123] R. Brun and F. Rademakers, *Nuclear Instruments and Methods in Physics Research Section A: Accelerators, Spectrometers, Detectors and Associated Equipment* **389**, 81 (1997), new Computing Techniques in Physics Research V.
- [124] M. Arinaga *et al.*, *Nuclear Instruments and Methods in Physics Research Section A: Accelerators, Spectrometers, Detectors and Associated Equipment* **499**, 100 (2003), KEK-B: The KEK B-factory.
- [125] K. Hagiwara, A. D. Martin, and D. Zeppenfeld, *Phys. Lett. B* **235**, 198 (1990).
- [126] R. J. Barlow and C. Beeston, *Comput. Phys. Commun.* **77**, 219 (1993).
- [127] C. Miller, “Measurement of Beam Polarization at an e^+e^- B-Factory with New Tau Polarimetry Technique,” (2022), Lake Louise Winter Institute.